ESTIMATING EVAPOTRANSPIRATION BY METRIC MODEL OVER
ÇAKIT BASIN

A THESIS SUBMITTED TO
THE GRADUATE SCHOOL OF NATURAL AND APPLIED SCIENCES
OF
MIDDLE EAST TECHNICAL UNIVERSITY

BY

DENİS DENİZHAN YANMAZ

IN PARTIAL FULFILLMENT OF THE REQUIREMENTS
FOR
THE DEGREE OF MASTER OF SCIENCE
IN
CIVIL ENGINEERING

DECEMBER 2019

Approval of the thesis:

ESTIMATING EVAPOTRANSPIRATION BY METRIC MODEL OVER ÇAKIT BASIN

submitted by **DENİS DENİZHAN YANMAZ** in partial fulfillment of the requirements for the degree of **Master of Science in Civil Engineering Department, Middle East Technical University** by,

Prof. Dr. Halil Kalıpçılar
Dean, Graduate School of **Natural and Applied Sciences**   _____

Prof. Dr. Ahmet Türer
Head of Department, **Civil Engineering**   _____

Prof. Dr. Zuhal Akyürek
Supervisor, **Civil Engineering, METU**   _____

Examining Committee Members:

Prof. Dr. İsmail Yücel
Civil Engineering, METU   _____

Prof. Dr. Zuhal Akyürek
Civil Engineering, METU   _____

Assoc. Prof. Dr. Uğur Murat Leloğlu
Geodetic and Geographic Information Technologies, METU   _____

Prof. Dr. Eyüp Selim Köksal
Agricultural Structures and Irrigation, Ondokuz Mayıs University_____

Assist. Prof. Dr. Hakan Aksu
Meteorological Engineering, Samsun University   _____

Date: 09.12.2019

I hereby declare that all information in this document has been obtained and presented in accordance with academic rules and ethical conduct. I also declare that, as required by these rules and conduct, I have fully cited and referenced all material and results that are not original to this work.

Name, Surname: Denis Denizhan Yanmaz

Signature:

ABSTRACT

ESTIMATING EVAPOTRANSPIRATION BY METRIC MODEL OVER ÇAKIT BASIN

Yanmaz, Denis Denizhan
Master of Science, Civil Engineering
Supervisor: Prof. Dr. Zuhal Akyürek

December 2019, 113 pages

Water availability is a topic of interest for many engineering fields. Hydrological cycle is the key to acknowledge the available water in a specific region. Evapotranspiration together with precipitation are the most impactful parameters of the hydrological cycle. A system gains water via precipitation and loses water due to evapotranspiration. Evapotranspiration is the process of water transfer from land to atmosphere by evaporation from soil and other surfaces and by transpiration from vegetation which can be defined as reference and actual evapotranspiration. In this study the main focus is the prediction of the water loss by actual evapotranspiration in a mountainous region. In addition, the reference evapotranspiration will be utilized for comparison with the results. The study region is the Çakıt basin located in south of Niğde province at the foot of Taurus mountains. In this study, actual evapotranspiration is mapped using Mapping EvapoTranspiRation with Internalized Calibration (METRIC) and R-METRIC models. Then, the estimations of the models are verified with the data obtained from an Eddy-Covariance flux tower that has been established. Both METRIC and R-METRIC models estimate seasonal trends adequately. However, the R-METRIC model yields closer results to the results of Eddy-Covariance flux tower than the METRIC model. Furthermore, the comparison with Eddy-Covariance method results is in good agreement with the models' results,

the Root Mean Square Error (RMSE) and the coefficient of determination (R^2) between R-METRIC model results and Eddy-Covariance flux tower measurements are calculated as 1.33 mm/day and 0.79 respectively. Although, some fluctuations in data is present due to the inadequacy of Eddy-Covariance method in mountainous regions.

Keywords: Actual Evapotranspiration, Energy Balance, METRIC Model, Remote Sensing

ÖZ

METRIC MODELİ KULLANILARAK ÇAKIT HAVZASI ÜZERİNDE BUHARLAŞMA/TERLEME HESAPLANMASI

Yanmaz, Denis Denizhan
Yüksek Lisans, İnşaat Mühendisliği
Tez Danışmanı: Prof. Dr. Zuhal Akyürek

Aralık 2019, 113 sayfa

Bir bölgedeki mevcut su miktarı birçok mühendislik alanı için ilgi konusudur. Hidrolojik döngü belirli bir bölgedeki mevcut suyu hesaplamanın anahtarıdır. Yağış ve buharlaşma-terleme hidrolojik döngünün en etkili parametreleridir. Hidrolojik bir sistem yağış yoluyla su kazanırken, buharlaşma-terleme sebebiyle su kaybeder. Buharlaşma-terleme yüzeyden atmosphere, toprak ve diğer yüzeylerden buharlaşma ile bitki örtüsünden terleme yoluyla su transferidir. Potansiyel ve gerçek buharlaşma-terleme olarak ikiye ayrılır. Bu çalışmada asıl odak noktası, dağlık bir bölgedeki gerçek buharlaşma-terleme ile gerçekleşen su kaybının hesaplanmasıdır. Ek olarak, potansiyel buharlaşma-terleme değerleri elde edilen sonuçlarla karşılaştırma için kullanılmıştır. Çalışma bölgesi, Niğde ilinin güneyinde Toros dağlarının eteğinde bulunan Çakıt havzasıdır. Bu çalışmada gerçek buharlaşma-terleme, Mapping EvapoTranspiRation with Internalized Calibration (METRIC) ve R-METRIC modelleri kullanılarak haritalanmıştır. Daha sonra, çalışma havzasında kurulmuş olan Eddy-Kovaryans akı kulesinden elde edilen verilerle modellerin tahminleri doğrulanmıştır. Hem METRIC hem de R-METRIC modelleri mevsimsel eğilimleri yeterince iyi tahmin etmektedir. R-METRIC modeli ile METRIC modeline kıyasla Eddy-kovaryans akı kulesi sonuçlarına daha yakın sonuçlar elde edilmiştir. Ayrıca, Eddy-Kovaryans yönteminin dağlık bölgelerde yetersizliğinden dolayı verilerde bazı

dalgalanmalar olmasına rağmen, yapılan karşılaştırma, modellerle iyi bir uyum içinde olduğunu göstermiştir. R-METRIC modeli sonuçları ile Eddy-Kovaryans akı kulesi verileri arasındaki korelasyon dikkate alındığında RMSE değeri 1.33 mm/gün iken R^2 değeri 0.79 olarak hesaplanmıştır.

Anahtar Kelimeler: Gerçek Buharlaşma-Terleme, Enerji Dengesi, METRIC Modeli, Uzaktan Algılama

To my love and to my family,

ACKNOWLEDGEMENTS

TABLE OF CONTENTS

LIST OF TABLES

LIST OF FIGURES

FIGURES

CHAPTER 1

INTRODUCTION

Water availability has always been a hot topic throughout centuries. Knowledge of the hydrological cycle which is the water movement between surface and atmosphere is the key to provide sustainable water resources. Water budget is a way to quantify the hydrological cycle by estimating the water storage change via inputs and outputs in a system. Water budget estimation is a complicated task which requires hydrological modeling. The main parameters of a hydrological model can be stated as precipitation, evapotranspiration (ET), infiltration, surface runoff and groundwater discharge. ET is the transfer of water from land to atmosphere by evaporation from soil and other surfaces and by transpiration from vegetation which can be defined as reference and actual ET. Reference ET is defined as the amount of ET that would occur if water amount is not a constraint, while actual ET is the quantity of water that is actually removed from a surface with limited water, due to the process of evapotranspiration. Around 60 percent of the land precipitation is lost due to ET (Carr, 1990). Thus, it is crucial to estimate the ET value adequately for the success of hydrological model.

In this study the main focus is the prediction of the water loss from the study basin due to actual ET. In addition, reference ET will be included in comparison of the results as a guideline. The actual ET can be calculated with direct and indirect methods. Water budget measurements and water vapor transfer methods are two commonly used types of direct ET calculation methods (Shuttleworth, 2008). In soil water budget measurements, the ET is determined according to the lost portion of a specific liquid water after accounting all other water budget components in terms of millimeters. The water vapor transfer methods utilize near surface meteorological sensors to calculate the movement of water vapor towards the atmosphere in terms of latent heat flux. The actual ET can be calculated using the latent heat flux which is the

flux of heat from the surface to the atmosphere that is associated with ET. The Eddy-Covariance observations are implemented in this study to provide the actual ET information at the point of interest. An Eddy-Covariance flux tower has been established in the Çakıt basin within the scope of TUBITAK115Y041 project. The Eddy-Covariance flux tower provides 30-minute time average flux data from which latent heat flux is further converted to actual ET at the tower location.

The most common indirect ET calculation methods are remote sensing-based ET methods which are based on surface energy balance and often provide precise ET estimates (Allen et al., 2005). The advantage of remote sensing-based ET methods compared to the direct methods is the capability to map actual ET with spatial and temporal variation. In the hydrological studies planned within the scope of TUBITAK 115Y041 project, it is aimed to determine and monitor the actual ET at the basin scale. Due to the requirement of actual ET estimation for large-scale application, the satellite-based energy balance for Mapping EvapoTranspiRation with Internalized Calibration (METRIC) model (Allen et al., 2007) which is an accepted method with a lot of applications in literature has been selected as the main method for this study. The METRIC model is an image processing model based on satellite imagery consisting of multiple sub-models to calculate ET as the residue of surface energy balance. The METRIC model was developed in The University of Idaho (Allen et al., 2007). A surface energy balance model named SEBAL model (Bastiaanssen et al., 1998) was the baseline to develop the METRIC model. The innovative feature of the SEBAL model is that it employs the temperature gradient close to the earth surface, dT, which is an indicator for satellite-based surface temperature. The novelty of the METRIC model is the selection of two boundary conditions (hot and cold pixels) that are taken into account for the calibration within the surface energy balance. The boundary condition selection is a complicated process which requires expert judgement for best calibration. The R-METRIC model which is based on the METRIC model has automatized hot-cold pixel selection that decreases the possibility of human error (Olmedo et al., 2016). In this study, R-METRIC model is utilized together with

the METRIC model. It is aimed to obtain the actual ET maps using R-METRIC and METRIC models and to compare model results with the Eddy-Covariance flux tower data.

This thesis is composed of seven chapters. After the introduction in Chapter 1, in Chapter 2 the review of similar studies in the literature is presented. In Chapter 3, the study basin and the materials utilized in this study are explained in detail. In Chapter 4, the working principles and governing equations deriving the Eddy-Covariance method, METRIC and R-METRIC models are interpreted. In Chapter 5, the progression of parameters along the model computations are illustrated and evaluated. In Chapter 6, comparisons and discussions of the results are provided and finally in Chapter 7, conclusions derived from the study and recommendations for future work are presented.

CHAPTER 2

LITERATURE REVIEW

There is a wide variety of evapotranspiration (ET) calculation methods (Rana, 2000). The remote sensing-based methods and the Eddy-Covariance method are utilized in this study.

In addition to those methods, the methods heavily presented in the literature are soil water balance, weighing lysimeters, Bowen ratio and Penman-Monteith model. ET is calculated indirectly as a residual of the water balance equation in the soil water balance method. Soil water balance is an indirect process where ET is calculated as a residual of the water balance equation which is related on the principle of mass conservation applied to the soil in one dimension. The soil water balance method is compared with variety of methods in the literature (Mastrorilli et al., 1998; Wilson et al., 2001). Weighing lysimeters were designed to calculate the ET directly via the movement of water crossing a boundary. They are reliable to calculate ET correctly (Tanner, 1967; Aboukhaled et al., 1982). The Bowen ratio is an indirect method using the surface energy balance. The reliability of the Bowen ratio method has been investigated in many studies (e.g. Fuchs and Tanner, 1970; Sinclair et al., 1975; Revfeim and Jordan, 1976). The Bowen ratio method is considered as a very accurate method in semi-arid regions after being broadly studied for different field conditions (e.g. Dugas et al., 1991; Frangi et al., 1996; Zhao et al., 1996). The Penman-Monteith model is impactful in actual ET calculations depending on both meteorological conditions and canopy properties (Szeicz and Long, 1969; Black et al., 1970; Szeicz et al., 1973).

The advantage of remote sensing-based methods and the reason this method is chosen for this study is that this method can estimate ET at basin scale, while the methods

explained above can only estimate ET at a point. A surface energy balance model named SEBAL model by Bastiaanssen (1998), was the baseline to develop the METRIC model (Allen et al., 2007). The innovative feature of the SEBAL model is that it employs the temperature gradient close to the earth surface, dT, which is an indicator for satellite-based surface temperature. The novelty of the METRIC model over the SEBAL model is the selection of two boundary conditions (hot and cold pixels) that are taken into account for the calibration within the surface energy balance.

The METRIC model was used in Idaho to investigate water right consistence and ground water usage as a tool for water asset arranging. In addition, the METRIC model was utilized in Rio Grande Valley, New Mexico, to evaluate water system sufficiency and to administer salinity (Trezza et al., 2013). In another study, MODIS was used in METRIC model to generate actual ET maps of Büyük Menderes basin by using satellite imagery (Aksu and Arikan, 2017). In addition, METRIC model has been utilized to figure out spectral vegetative indexes as a hint about plant coefficient and plant water consumption under full and limited irrigation conditions (Köksal, 2008).

In the study presented by He (2017), the METRIC model is utilized to obtain ET over an almond orchard in California. A 50 meters fetch around a flux tower is used to calculate the METRIC model results. The results of the model are compared with the flux tower data. The latent heat flux of the tower is calculated as a residue of the surface energy balance ($LE = R_n - G - H$). As inputs to the METRIC model, 46 Landsat 5 and 7 satellite images are employed and 30-minute flux tower data are utilized. There is a good agreement between METRIC model results and flux tower calculations. However, for cloudy and rainy weathers the uncertainty of the flux tower data increases.

In the study presented by Oliveira (2018), the METRIC model is utilized to obtain ET over agricultural and natural areas in Brazil. The results of the model are compared with the Eddy-Covariance flux tower data. As inputs to the METRIC model, MODIS/TERRA satellite images are employed and 30-minute flux tower data are

utilized. There is a good match between METRIC model results and Eddy-Covariance method results. The METRIC model overestimates ET by 14 % for natural vegetation which is the highest error encountered in this study.

In the study presented by Madugundu et al. (2017), the METRIC model is utilized to obtain ET over irrigated field in Saudi Arabia. The results of the model are compared with the Eddy-Covariance flux tower data. As inputs to the METRIC model, Landsat 8 satellite images are utilized. The agreement between the METRIC model results and the Eddy-Covariance method results is good. The author concludes that the METRIC model estimations are better at full canopy compared to the partial canopy. In addition, the METRIC model underestimates the Eddy-Covariance method by 4.2 % on daily ET which is unusual regarding current studies in literature.

In the study presented by Lian and Huang (2015), the METRIC model is utilized to obtain ET for an oasis area in the Heihe River Basin in China. The results of the model are compared with the Eddy-Covariance flux tower data. As inputs to the METRIC model, 14 Landsat 8 satellite images are utilized. The METRIC model overestimates daily ET compared to Eddy-Covariance method. The authors state some problems regarding flux readings due to sensor failures and bad weather conditions. According to Wang and Dickinson (2012), 70 % of the direct latent heat flux measurements from an Eddy-Covariance system remain after considering bad weather conditions and failures.

In the study presented by Tasumi (2019), the METRIC model is utilized to obtain ET over irrigated agriculture in the western Urmia Lake Basin in Iran. The results of the model are compared with the Penman-Monteith reference ET from FAO-56. As inputs to the METRIC model, 34 Landsat 8 satellite images are utilized. There is a good correlation between the METRIC model results and the Penman-Monteith reference ET. However, ET is overestimated on bare soil which is problematic for mountainous regions.

In the study presented by Büyükcangaz et al. (2017), the METRIC model is utilized to obtain ET to assess performance of irrigation in flood mitigation of Devils lake basin in North Dakota. The results of the model are compared with the Eddy-Covariance flux tower data. However, the Eddy-Covariance tower is situated near the edge of the satellite image causing lack of hot-cold pixels. As inputs to the METRIC model, Landsat 5 satellite images are utilized. The authors suggest to utilize Landsat 7 satellite images especially for years with few suitable Landsat 5 satellite images and conclude 23 % increase of crop ET helps the disposal of excess water occurring in flood events.

CHAPTER 3

STUDY AREA AND MATERIALS

3.1. Study Area

The study basin spreads a 529 km^2 territory between 37.38°-37.59° N latitudes and 34.39°-34.77° E longitudes in the south of Turkey (Figure 3.1). The study basin is famous for cherry production which is the main source of income and the irrigation is provided by streamlets and the Çakıt river. The area is mountainous which increases the heterogeneity in the basin. Bolkar Mountains are situated at the south of the area coming to up to 3450 m altitude inside the basin boundary. The principal stream of the site is Çakıt river which begins from western side of the study area at around 1500 m altitude, and the river leaves the study basin, around 1000 m altitude.
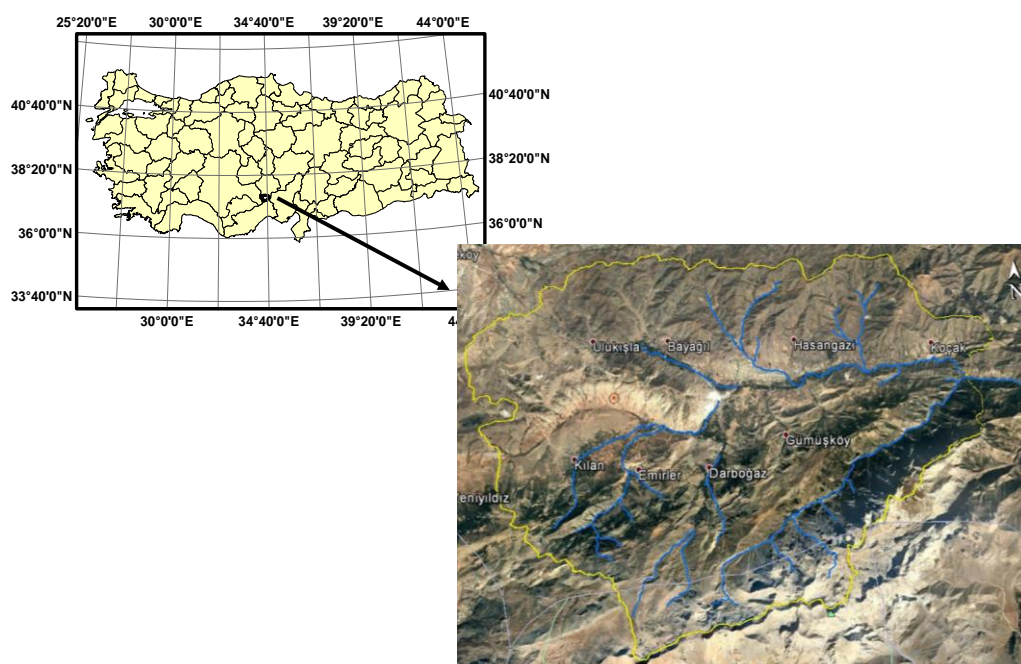
Figure 3.1. The location and the Google Earth image of the Çakıt Basin

The study basin was selected for the project TUBITAK115Y041. The focus of the project is to develop a hydrological model using a smaller number of parameters to calibrate and understand the hydrological processes in detail. For this purpose, three meteorological stations (total of four with already operated by Turkish State Meteorological Service (MGM) at Ulukışla), three stream gauging stations, one Eddy Covariance flux tower and one cosmic ray sensor have been established in the study basin (Figure 3.2).

On the north-west of the study basin the Ulukışla meteorological station is situated at an altitude of 1453 meters and this station is measuring meteorological data since 1937 (Figure 3.2). Using the Ulukışla meteorological long-term data shared by MGM some more information can be given about the study basin.
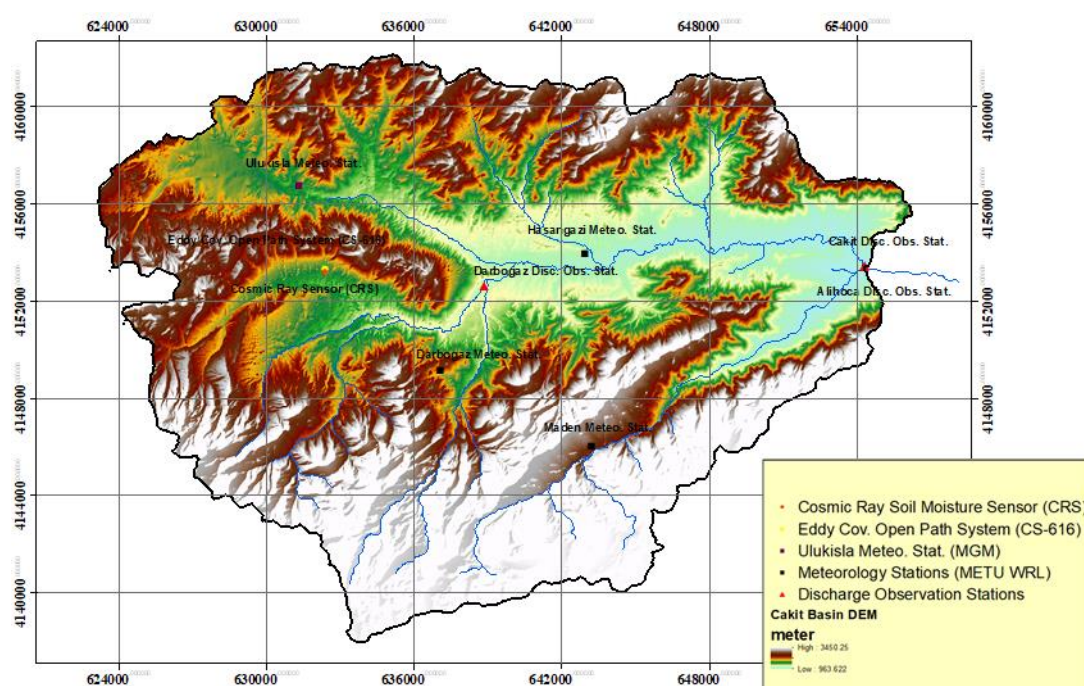
Figure 3.2. Study basin and locations of hydrometeorological stations

(Projection UTM36)

3.1.1. Temperature

The average annual temperature for long-term from the values measured at Ulukışla meteorological station is presented in Figure 3.3. For the observation period the month with the highest temperature is July with a mean of 21.6 °C and the lowest temperature is January with a mean of -1.8 °C given in Table 3.1. Monthly min. and max. temperature values are also presented in Table 3.1. In this table, the max. temperature measured at the Ulukışla meteorological station is 37.5 °C in July, while the minimum temperature is -21.5 °C in February.
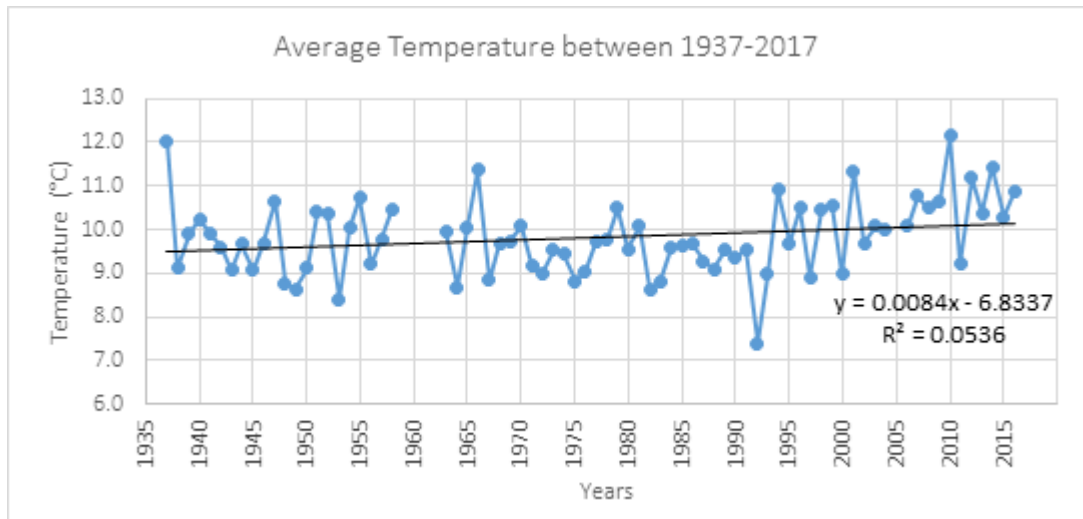
Figure 3.3. Ulukışla meteorological station average annual temperatures (°C) for long-term data

Table 3.1. Ulukışla meteorological station monthly average, maximum and
minimum temperatures between 1937-2017 (°C)

	Average temp.	Maximum temp.	Minimum temp.
October	10.90	32.00	-6.50
November	5.00	22.70	-15.50
December	0.30	17.50	-21.00
January	-1.80	18.00	-20.10
February	-0.30	19.60	-21.50
March	3.50	25.00	-20.50
April	8.90	29.00	-12.00
May	13.50	30.20	-7.00
June	18.10	33.00	2.50
July	21.60	37.50	4.80
August	21.30	36.10	5.40
September	16.70	33.00	0.00
Annual	9.80	37.50	-21.50

Monthly average temperature values observed at Ulukışla meteorological station and
Eddy-Covariance flux tower are compared in Table 3.2 for 2017-2018 water year
starting from October 2017 and ending in September 2018, where both stations have
complete data. The comparison shows that, being at similar altitudes (Ulukışla station
is located at 1453 m and Eddy-Covariance tower is located at 1478 m), both stations
have well matching monthly average temperatures.

Table 3.2. Ulukışla meteorological station and Eddy-Covariance tower monthly average temperatures for 2017-2018 water year (°C)

	Ulukışla average temp. (°C)	Eddy-cov. average temp. (°C)
October	11.18	11.36
November	5.02	5.46
December	3.92	4.15
January	-0.28	0.22
February	4.11	4.28
March	8.14	8.33
April	11.71	11.71
May	14.92	14.65
June	18.30	18.09
July	22.28	22.11
August	21.89	21.86
September	18.47	18.40

3.1.2. Lapse Rate

The lapse rate provides information about the height-dependent temperature variation of the basin and can be used to spatially distribute the temperature. Lapse rate is not a fixed value. It varies according to climatic and meteorological characteristics according to time and region characteristics. To find a reliable lapse rate in mountainous areas, a large number of stations scattered over each altitude and long-term temperature data are required. According to NOAA (1976), -6.5 °C/km is the global lapse-rate value. Lapse rate equations are commonly utilized with regard to air lifted "vertically" upwards under various humidity conditions. Examination of lapse rate in mountains is an interesting topic related to many studies (Thyer, 1985; Rolland, 2003; Harlow et al., 2004). However, the challenges still exist.

The lapse rate study of Rolland (2003) in the Alps has 4 different regions and data sets. Those regions are Northern Italy, Tyrol, Trentin VB and Trentin SL and they contain 269 (30 years of data), 205 (31 years of data), 105 (55 years of data) and 61 (55 years of data) stations, respectively. Monthly and yearly average maximum, minimum and mean temperature values including a linear model T = A*height+B was

used. "A" being the lapse rate and "B" being the sea level temperature. The results of the regression equation were evaluated with the coefficient of fit (R^2). According to the study, it was observed that the most compatible data was maximum temperature and the adaptation decreased in winter months. When the minimum temperature data are considered, the compatibility is very low and in some months the temperature increases as the height increases (temperature inversion). As a result, while the annual lapse rate varies between -5.4 °C/km and -5.8 °C /km for the 4 regions of the study, the average lapse rate in the summer season varies between -6.3°C/km and -6.6 °C/km. In the study of Rolland (2003), it was observed that lapse rate converged to the environmental lapse-rate value from mid-spring to mid-autumn when ET is an important parameter. Therefore, due to the insufficient number of meteorological stations in the Çakıt basin and lack of long-term data, the environmental lapse-rate value of -6.5 °C/km is used. In addition, it is considered appropriate to use a constant lapse-rate of -6.5 °C/km since the study basin is considerably small.

3.1.3. Precipitation (Rainfall)

Total annual rainfall from the data observed at Ulukışla meteorological station is presented in Figure 3.4 between years 1929-2017. The total annual rainfall of the region tends to decrease noticeably over the years. There is a lack of monthly rainfall data in July and August. Since those months are generally rainless, the lack of data is not crucial in calculations of yearly rainfall.
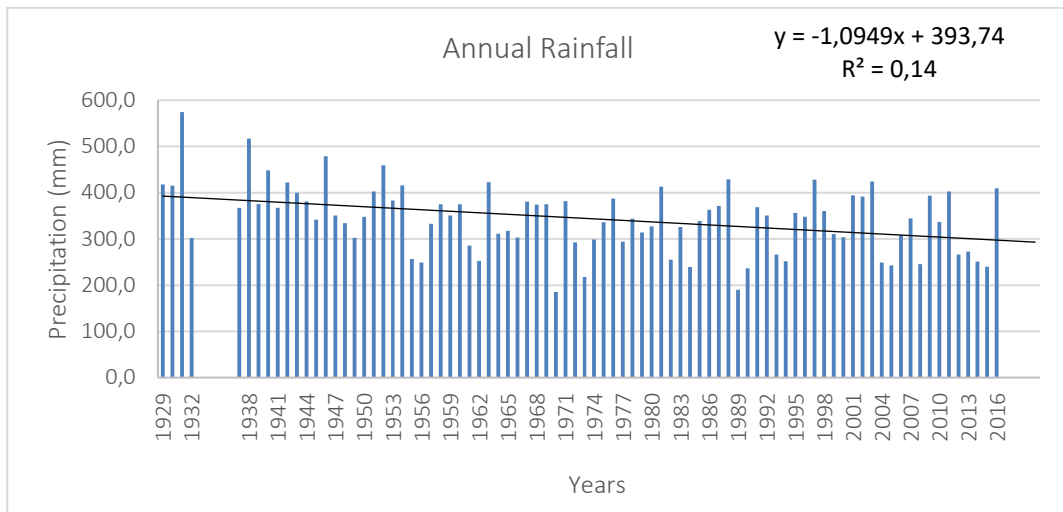
Figure 3.4. Total annual rainfall values obtained from Ulukışla meteorological station

The Ulukışla meteorological station and the Eddy-Covariance flux tower monthly and annual rainfall data for 2017-2018 water year are given in Table 3.3. Comparing the rainfall data, Ulukışla meteorological station values are much higher than the Eddy-Covariance flux tower data. For the Ulukışla station snow looks melted for winter months. However, for the Eddy-Covariance tower snow melt is not measured reliably.

Table 3.3. Ulukışla meteorological station and Eddy-Covariance tower monthly rainfall for 2017-2018 water year (mm)

	Ulukışla rainfall (mm)	Eddy-cov. rainfall (mm)
October	4.60	1.00
November	31.00	12.90
December	21.00	8.40
January	67.00	18.70
February	15.00	5.40
March	39.20	16.40
April	55.20	22.00
May	29.40	18.40
June	63.40	25.60
July	1.80	0.50
August	0.00	0.00
September	0.00	3.10
Annual	327.60	132.40

3.1.4. Relative Humidity and Wind

The monthly average relative humidity values are shown in Table 3.4, according to the data gathered from Ulukışla meteorological station between 1975-2017. The monthly maximum average relative humidity is 92 % (February 1980) and the monthly minimum average relative humidity is 29 % (September 2015), while the annual average relative humidity is 62 %.

According to the monthly wind speed data obtained from Ulukışla meteorological station in the study area, the monthly maximum average wind speed between 1975 and 2017 is 6.1 m/s (January 1981) and the monthly minimum average wind speed is 1.7 m/s (November 2011). Monthly mean wind speeds are given in Table 3.4 and the yearly mean wind speed is 3.1 m/s.

Table 3.4. Long-term average relative humidity and average wind speed data at Ulukışla Meteorological station

	Average relative humidity (%)	Average wind speed (m/s)
October	63.00	2.60
November	69.00	3.10
December	76.00	3.40
January	77.00	3.50
February	74.00	3.50
March	68.00	3.50
April	63.00	3.60
May	61.00	3.10
June	54.00	2.90
July	47.00	3.00
August	47.00	3.00
September	52.00	2.70
Annual	62.00	3.10

3.2. Data Used

3.2.1. Satellite Data

The earth explorer website is used to download the Landsat 8 in this study (url1). two frames of the Landsat 8 satellite (row: 34, path: 175 and 176) are covering the study basin. For this reason, the temporal resolution is enhanced from 16 days to approximately 8 days. In METRIC model, the satellite imagery is preferred to be cloudless. No operations can be performed on the corresponding pixels in the clouds and also it is very difficult to exclude these pixels. Images from March 2017 to October 2018 are reviewed and 13 cloudless images and 30 partly cloudy images are selected to be used for this study. Among them 17 images shown with * are used for METRIC model while all 43 images are used for R-METRIC model (Table 3.5). The reason of selecting partly cloudy images is to increase the temporal resolution of the study. Since the altitude of the study basin is high, cloud cover is a serious problem.

Table 3.5. Date of the Landsat 8 images selected for the study and the total of snow/ice, cloud and cloud shadow (S/I, C, CS) percentages

#	Date	S/I, C, CS (%)	#	Date	S/I, C, CS (%)
1*	24.04.2017	35.7	23	15.02.2018	64.1
2	10.05.2017	33.8	24	22.02.2018	62.1
3	04.06.2017	55.0	25*	26.03.2018	28.8
4*	27.06.2017	11.0	26*	04.04.2018	28.5
5	06.07.2017	25.4	27*	06.05.2018	31.0
6*	13.07.2017	6.1	28*	07.06.2018	31.2
7	22.07.2017	11.7	29*	14.06.2018	35.9
8	29.07.2017	14.3	30*	30.06.2018	31.4
9*	07.08.2017	4.1	31*	09.07.2018	6.8
10	14.08.2017	24.5	32	16.07.2018	13.9
11	23.08.2017	14.7	33	25.07.2018	35.9
12	30.08.2017	41.4	34	01.08.2018	19.2
13*	08.09.2017	1.7	35*	10.08.2018	7.1
14*	24.09.2017	1.7	36*	17.08.2018	0.5
15	01.10.2017	37.0	37*	26.08.2018	2.4
16*	17.10.2017	0.6	38	02.09.2018	1.1
17	02.11.2017	17.1	39	18.09.2018	8.6
18	11.11.2017	31.8	40	27.09.2018	1.8
19	27.11.2017	43.1	41	04.10.2018	1.2
20	13.12.2017	44.6	42	20.10.2018	41.8
21	29.12.2017	29.3	43	29.10.2018	33.8
22	06.02.2018	84.3			

The Landsat 8 spectral bands and their characteristics are shown in Table 3.6. The thermal bands of a Landsat 8 satellite image are band 10 and band 11, those bands are used for mapping the surface temperature. Band 1, band 8 and band 9 are not used in the METRIC applications.

Table 3.6. The spectral bands of Landsat 8 imagery

Band #	Bands	Wave length (µm)	Spatial resolution (m)
1	Visible	0.43 – 0.45	30
2	Visible (Blue)	0.45 – 0.51	30
3	Visible (Green)	0.53 – 0.59	30
4	Red	0.64 – 0.67	30
5	Near-infrared	0.85 – 0.88	30
6	SWIR 1	1.57 – 1.65	30
7	SWIR 2	2.11 – 2.29	30
8	Panchromatic	0.50 – 0.68	15
9	Cirrus	1.36 – 1.38	30
10	TIRS 1	10.60 – 11.19	100
11	TIRS 2	11.50 – 12.51	100

3.2.2. Eddy Covariance Flux Tower and Meteorological Data

The METRIC model requires meteorological data at the daily and hourly scale. Meteorological information utilized for the two models incorporate hourly meteorological factors comprising of mean temperature (°C), mean relative humidity (%), short-wave incoming radiation (W m^{-2}) and wind speed (m s^{-1}) for the period of the study derived from the Eddy Covariance flux tower located at 1478 meters. The energy balance on the surface can be calculated by the Eddy-Covariance method. Net radiation (R_n) and solar radiation (R_s) values are measured directly as components of the energy balance. The radiation value measured on the surface is used in different physical processes. The most significant processes of the surface energy balance are the energy required for evapotranspiration of water (Evaporation latent heat, LE), the energy used to heat air above the surface (sensible heat flux, H), and the energy used for heating the ground under the surface by conductivity (soil heat flux, G). However, the amount of energy coming and going via surface transport, the amount of energy used for photosynthesis and the energy processes accumulated in the environment when there is forest or dense vegetation are generally neglected. Another parameter that is neglected is S, the heat storage change ratio (air and biomass) between the Eddy-Covariance level and the soil surface. It would be a problem to add this parameter to the surface energy balance since the S value is not obtained directly. But

according to Wilson et al., (2002) if the height of the vegetation is less than 8 meters, using half-hour data without S value is not a problem. These error values can be minimized by considering other components in the energy balance or by taking calibration errors into account. The sum of energy consumed by these processes should be equal to the amount of R_n measured on the surface. Therefore, the measured R_n is shared by the physical processes mentioned above. As the surface type (dry, moist soil, plant type, snow cover) changes, which of the physical processes will be more dominant and the amount of radiation sharing can be determined.

It is estimated that the R_n will be shared more between the three main fluxes explained earlier, sensible heat, soil heat and latent heat fluxes. According to a study that tries to equalize the surface energy balance and solve the daily error payments by means of spatial average flow measurements, the most direct method to examine the environment around the Earth and the change of trace gases in turbulence is the Eddy-Covariance method (Twine, et al., 2000). However, this method is based on flat homogeneity and zero mean upright wind speed conditions. Also, upright and horizontal flux separation cannot be followed. This, among other things, leads to a closure problem of balancing the surface energy. Twine et al., (2000) estimated that the distant flux estimate has a bias value of between 10% and 30% of the available energy on the surface. This error margin even exists on flat vegetative surfaces which are best suited for the Eddy-Covariance method.

3.2.3. Digital Elevation Model (DEM) and Land Cover Data

The Digital Elevation Model data is obtained from topography data gathered from the General Directorate of Mapping. The DEM has 30-meter spatial resolution (Figure 3.2) and is further utilized to generate slope and aspect maps.

The slope map is created using the Digital Elevation Model with Arcmap "Slope" tool. The slope of the location of Eddy station is 0.165 radians which is around 9.5° (Figure 3.5).
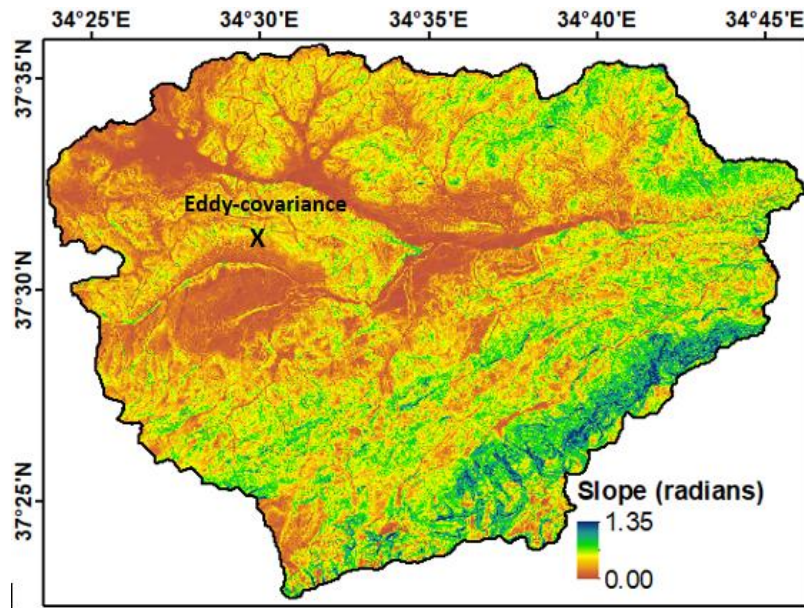
Figure 3.5. METRIC model slope map generated from DEM

The aspect map is created using the Digital Elevation Model with Arcmap "Aspect" tool. The aspect of the location of Eddy station is -1.25 radians where the south is 0, the north is π and $-\pi$, east is $-\pi/2$ and finally west is $\pi/2$ (Figure 3.6). Therefore, the Eddy station is facing the south-east direction.
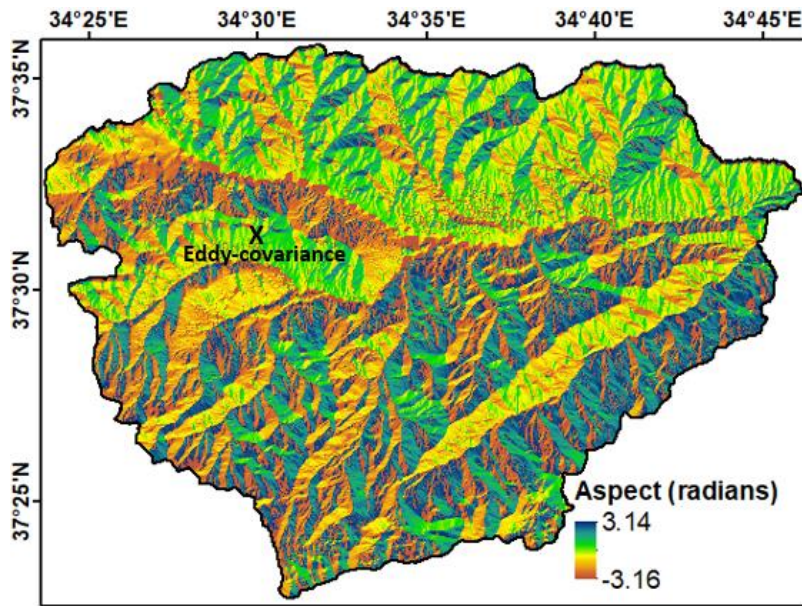
Figure 3.6. METRIC model aspect map generated from DEM

The momentum roughness length (z_{om}) needed for the calibration of sensible heat flux (H) is retrieved using Corine Land Cover Classes (Silva et al., 2007). Due to the assumption of short crop and the heterogeneity of land cover, it is preferred to use CORINE Land Cover Class map dated 2018 in this study. Examining the 1 km radius region around the Eddy-Covariance flux tower, the region is composed of a mixture of arable lands, sparsely vegetated areas and bare rock (Figure 3.7).
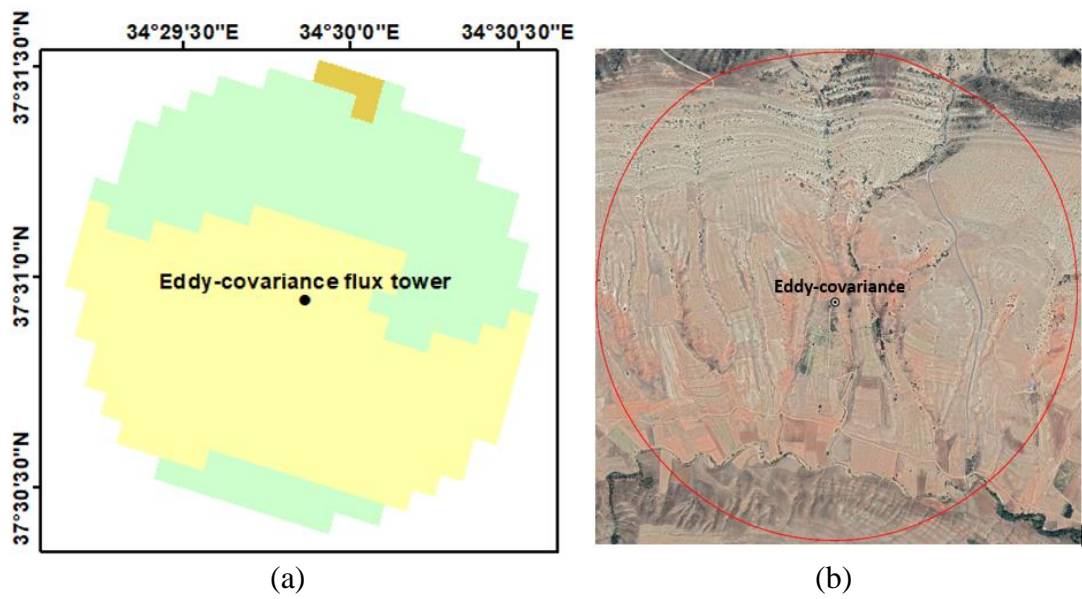
Corine Land Cover 2018
☐ Non-irrigated arable land; Permanently irrigated land
☐ Agro-forestry areas
☐ Bare rock; Sparsely vegetated areas

Figure 3.7. (a) CORINE Land Cover Class map within 1km radius from Eddy-Covariance flux tower and (b) Google Earth image (26.07.2019)

CHAPTER 4

METHODS

A schematic outline of the model is displayed in Figure 4.1. Equations to calculate the parameters of the METRIC model are described in sub-sections.
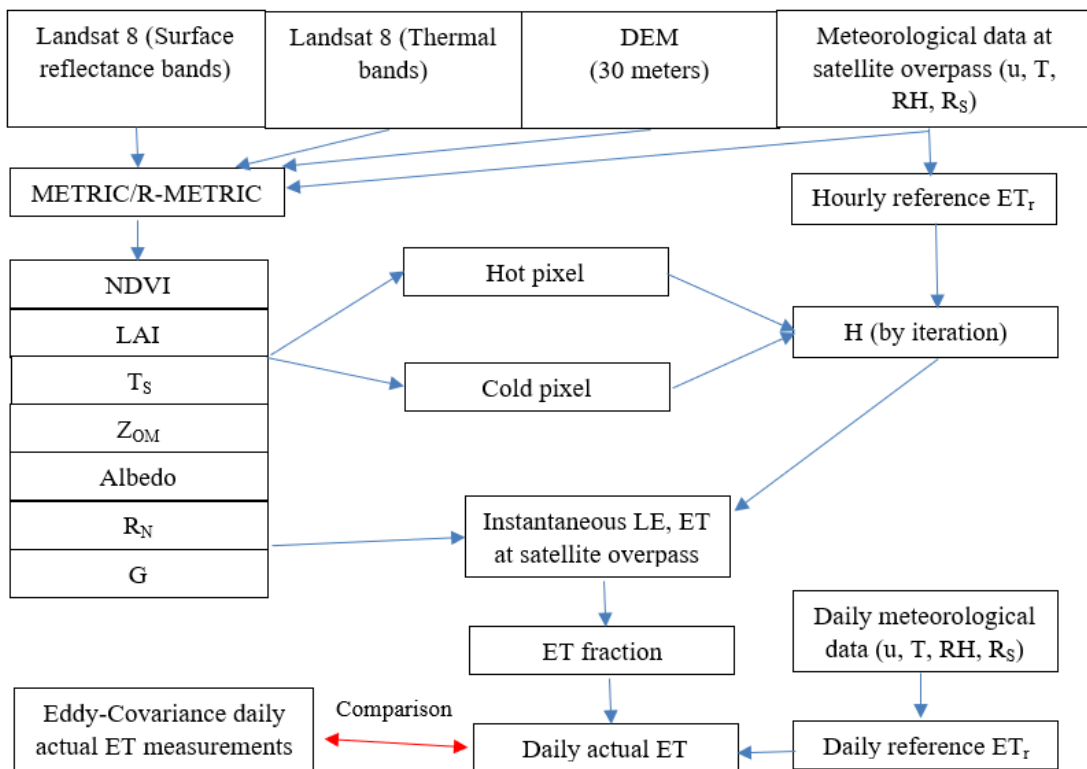
Figure 4.1. Schematic overview of the methodology used in this study

4.1. Penman-Monteith Reference Evapotranspiration

The formulation of the Penman-Monteith Reference ET will be presented in this section.

Alfalfa is the suggested vegetation for the METRIC model and the alfalfa reference ET values are calculated by ASCE-EWRI's standardized Penman-Monteith equation, given in Equation [4.1] as

$$ET_{sz} = \frac{0.408\Delta(R_n - G) + \gamma \dfrac{C_n}{T + 273} u_2(e_s - e_a)}{\Delta + \gamma(1 + C_d u_2)} \qquad [4.1]$$

where;

ET_{sz} = standardized reference crop evapotranspiration (ET_r) (mm d^{-1} for daily time steps or mm h^{-1} for hourly time steps),

R_n = calculated net radiation at the crop surface (MJ m^{-2} d^{-1} for daily time steps or MJ m^{-2} h^{-1} for hourly time steps),

G = soil heat flux density at the soil surface (MJ m^{-2} d^{-1} for daily time steps or MJ m^{-2} h^{-1} for hourly time steps),

T = mean daily or hourly air temperature at 2-meter height (°C),

u_2 = mean daily or hourly wind speed at 2-meter height (m s^{-1}),

e_s = saturation vapor pressure at 2-meter height (kPa), calculated for daily time steps as the average of saturation vapor pressure at maximum and minimum air temperature,

e_a = mean actual vapor pressure at 2-meter height (kPa),

Δ = slope of the saturation vapor pressure-temperature curve (kPa °C^{-1}),

γ = psychrometric constant (kPa °C^{-1}),

C_n = numerator constant that changes with reference type and calculation time step (K mm s^3 Mg^{-1} d^{-1} or K mm s^3 Mg^{-1} h^{-1}) and

C_d = denominator constant that changes with reference type and calculation time step (s m^{-1}).

26

Units for the 0.408 coefficient are m^2 mm MJ^{-1} (ASCE-EWRI, 2005).

4.1.1. Penman-Monteith Equations

The atmospheric pressure, which depends on the altitude of the station above sea level, is calculated by using the equation [4.2].

$$P = 101.3 \left(\frac{293 - 0.0065z}{293}\right)^{5.26} \qquad [4.2]$$

In the FAO-56 Penman-Monteith equation, the latent heat of vaporization (λ) is taken as 2.45 MJ kg^{-1} for ease of processing (Allen et al., 1998). In Equation [4.3], the psychrometric constant (γ) formula is given and it depends only on atmospheric pressure;

$$\gamma = \frac{c_p * P}{\varepsilon * \lambda} = 0.665x10^{-3} \, P \qquad [4.3]$$

where $c_p = 1.013*10^{-3}$ is the specific heat at constant pressure, $\varepsilon = 0.622$ is the water vapor/dry air molecular weight ratio.

Saturation vapor pressure only varies with temperature and its formula is given in Equation [4.4].

$$e^{\circ}(T) = 0.6108 \exp\left[\frac{17.27 \, T}{T + 237.3}\right] \qquad [4.4]$$

Slope of the saturation vapor pressure-temperature curve (Δ) is calculated based on the average temperature as in Equation [4.5].

$$\Delta = \frac{4098\left[0.6108 \exp\left(\frac{17.27 \, T}{T + 237.3}\right)\right]}{(T + 237.3)^2} \qquad [4.5]$$

The maximum and minimum relative humidity together with the maximum and minimum temperature data are used for the daily actual vapor pressure (e_a) calculation given in Equation [4.6].

$$e_a = \frac{e^\circ(T_{min})\frac{RH_{max}}{100} + e^\circ(T_{max})\frac{RH_{min}}{100}}{2} \qquad [4.6]$$

The actual hourly vapor pressure (e_a) given in Equation [4.7] varies depending on the average relative humidity and average temperature.

$$e_a = \frac{RH}{100} e^\circ(T) \qquad [4.7]$$

Equation [4.8] is used to calculate the daily extraterrestrial radiation (R_a). Then from extraterrestrial radiation, clear-sky solar radiation (R_{so}) is calculated, as given in Equation [4.8].

$$R_a = \frac{24\,(60)}{\pi} G_{sc}d_r[\omega_s \sin(\varphi)\sin(\delta) + \cos(\varphi)\cos(\delta)\sin(\omega_s)] \qquad [4.8]$$

where;

R_a = daily extraterrestrial radiation [MJ m^{-2} d^{-1}],

G_{sc} = solar constant [4.92 MJ m^{-2} h^{-1}],

d_r = inverse relative distance factor for the earth-sun [unitless] (Equation [4.9]),

δ = solar declination [radians] (Equation [4.10]),

ϕ = latitude [radians], in study 0.65 and

ω_s = sunset hour angle [radians] (Equation [4.11]) (ASCE-EWRI, 2005).

J is the Julian day of the year and for date 27 June 2017, J is 178.

$$d_r = 1 + 0.033 \cos\left(\frac{2\pi}{365}J\right)$$

[4.9]

$$\delta = 0.409 \sin\left(\frac{2\pi}{365}J - 1.39\right)$$

[4.10]

$$\omega_s = \arccos[-\tan(\varphi)\tan(\delta)]$$

[4.11]

In Equation [4.12] the hourly extraterrestrial radiation (R_a) formulation is given, as follows;

$$R_a = \frac{12\,(60)}{\pi}\,G_{sc}d_r[(\omega_2 - \omega_1)\sin(\varphi)\sin(\delta) + \cos(\varphi)\cos(\delta)\,(\sin(\omega_2) - \sin(\omega_1))]$$

[4.12]

where;

R_a = extraterrestrial radiation during the hour period [MJ m^{-2} h^{-1}],

G_{sc} = solar constant [0.0820 MJ m^{-2} min^{-1}],

ω_1 = solar time angle at beginning of period [radians] (Equation [4.13]),

ω_2 = solar time angle at end of period [radians] (Equation [4.14]) (ASCE-EWRI, 2005).

$$\omega_1 = \omega - \frac{\pi t_1}{24}$$

[4.13]

$$\omega_2 = \omega + \frac{\pi t_1}{24}$$

[4.14]

ω = solar time angle [radians] (Equation [4.15]),

t_1 = length of the calculation period, 0.5 for 30-minute data.

$$\omega = \frac{\pi}{12} \left[(t + 0.06667(L_z - L_m) + S_c) - 12 \right] \qquad [4.15]$$

t = standard clock time at the midpoint of the period, in study 11.5,

L_z = longitude of the center of the local time zone, in study 330°,

L_m = longitude of the solar radiation measurement site, in study 325.5°,

S_c = seasonal correction for solar time [hour] (Equation [4.16]).

$$S_c = 0.1645 \sin(2b) - 0.1255 \cos(b) - 0.025 \sin(b) \qquad [4.16]$$

where;

$$b = \frac{2\pi (J - 81)}{364}$$

In Equation [4.17] the formulation of clear-sky solar radiation is given. The clear-sky solar radiation is related to the elevation and extraterrestrial radiation.

$$R_{so} = (0.75 + 2 * 10^{-5} z)R_a \qquad [4.17]$$

The net short-wave radiation (R_{ns}) is calculated as stated in Equation [4.18]. The solar radiation (R_s) is measured at the Eddy-Covariance flux tower. Albedo (α) which defines the reflectivity of a surface is not a fixed value. Albedo changes with time of the day, time of the season and latitude. So, it is hard to quantify albedo especially for daily reference ET calculations. Therefore, the recommended value of 0.23 (Allen, 1994) will be accepted in this study.

$$R_{ns} = (1 - \alpha)R_s \qquad [4.18]$$

In Equation [4.19] the formulization of net long-wave radiation is given. The net long-wave radiation (R_{nl}) is added to the net short-wave radiation (R_{ns}) to obtain the net radiation (R_n) given in Equation [4.20]. When calculating daily R_{nl}, maximum and minimum temperatures are used. However, while calculating hourly R_{nl}, average

temperature $(T_{ave, K})^4$ is used. The temperature unit is Kelvin. The Stefan-Boltzmann constant (σ) is 4.903×10^{-9} MJ K^{-4} m^{-2} d^{-1}.

$$R_{nl} = \sigma\left[\frac{T_{max,K}^4 + T_{min,K}^4}{2}\right](0.34 - 0.14\sqrt{e_a})(1.35\frac{R_s}{R_{so}} - 0.35) \qquad [4.19]$$

$$R_n = R_{ns} - R_{nl} \qquad [4.20]$$

In Equation [4.21] the hourly daytime soil heat flux formula is given and it only depends on the R_n.

$$G_{hr,daytime} = 0.04\ R_n \qquad [4.21]$$

4.2. METRIC Model

The METRIC model is a satellite-based image processing model consisting of multiple sub-models to calculate actual ET as the residue of surface energy balance.

The primary data required by the METRIC model are the Thermal Infrared Sensor bands, the metadata file of the image and the Operational Land Imager bands. The digital elevation model (DEM) is utilized to produce aspect and slope required for adjusting the surface temperature (T_s) and mountainous terrain corrections of the model.

METRIC model computes the latent heat flux (LE, W m^{-2}) at satellite passing time, as the residual of surface energy (Equation [4.22]). Thus, the instantaneous ET is the product of the METRIC model.

$$\lambda\mathrm{ET} = LE = R_n - \mathrm{H} - \mathrm{G} \qquad [4.22]$$

where; R_n is the net radiation flux at the surface (W m^{-2}), G is the soil heat flux (W m^{-2}), and H is the sensible heat flux (W m^{-2}). The latent heat flux is transformed into instantaneous ET by dividing LE to latent heat of vaporization (λ).

The surface energy balance used in the METRIC model is illustrated in Figure 4.2.
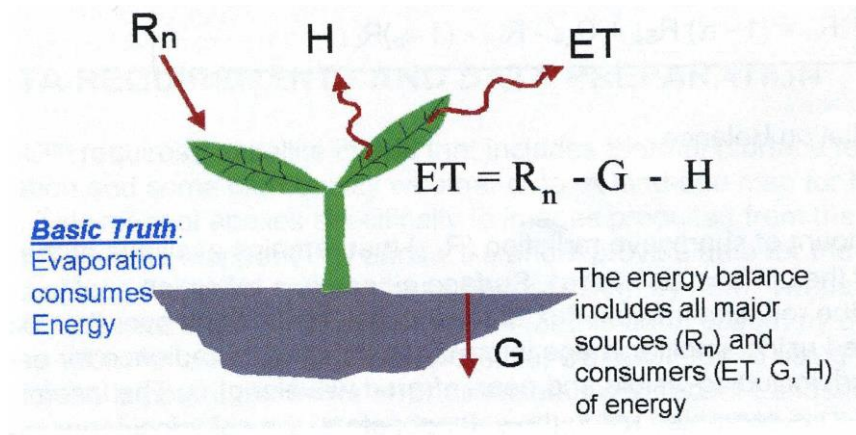
Figure 4.2. Surface Energy Balance (Allen et al., 2007)

The METRIC model is best used in flat regions. However, there are several mountainous region corrections in the model with the utilization of the digital elevation model, slope and aspect data (Allen et al., 2007).

4.2.1. R_n Calculation

The METRIC model determines the R_n from Equation [4.23] (Allen et al., 2007; Bisht et al., 2005) utilizing the solar radiation together with the incoming and outgoing long-wave radiation. The albedo is also an important parameter to calculate the R_n. The R_n calculation is given in Figure 4.3.

$$R_n = R_{s\downarrow} - \alpha R_{s\downarrow} + R_{L\downarrow} - R_{L\uparrow} - (1 - \varepsilon_0)R_{L\downarrow} \qquad [4.23]$$

where $R_{S\downarrow}$ is the incoming short-wave solar radiation calculated at the time of the satellite overpass assuming clear-sky conditions (W m^{-2}), $R_{L\downarrow}$ is the incoming long-wave radiation (W m^{-2}) calculated using the Stefan-Boltzman equation. The updated version of the effective atmospheric emissivity can be found in Allen et al., (2000). The outgoing solar radiation $\alpha R_{S\downarrow}$ (W m^{-2}) is determined utilizing albedo (dimensionless). $R_{L\uparrow}$ is the emitted long-wave solar radiation determined utilizing

broadband surface thermal emissivity ε_0 (dimensionless) and surface temperature (°K), and $(1 - \varepsilon_0)$ $R_{L\downarrow}$ is the outgoing long-wave solar radiation (W m^{-2}). ε_0 is registered as a component of LAI (Equation [4.37]). In many studies such as (Allen et al., 2011; Allen et al., 2006; Bastiaanssen et al., 1998; Jensen et al., 1990), the solar radiation parameters are explained in detail.
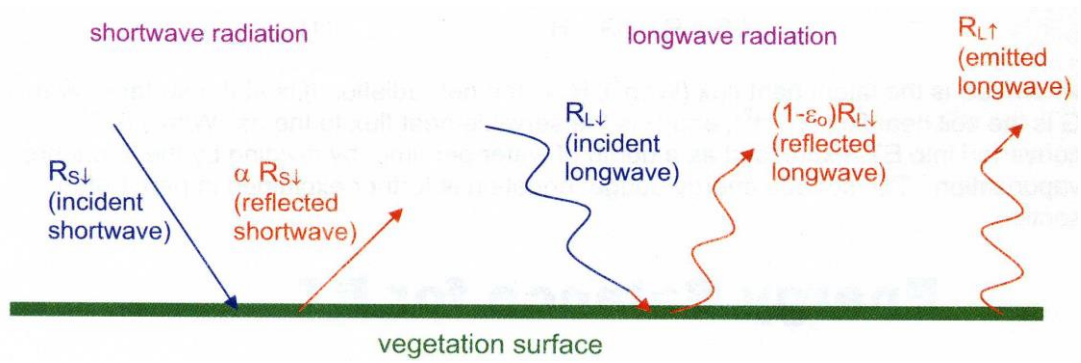
Figure 4.3. Radiation Balance (Allen et al., 2007)

The flow chart used by the METRIC model for the calculation of R_n is illustrated in Figure 4.4.
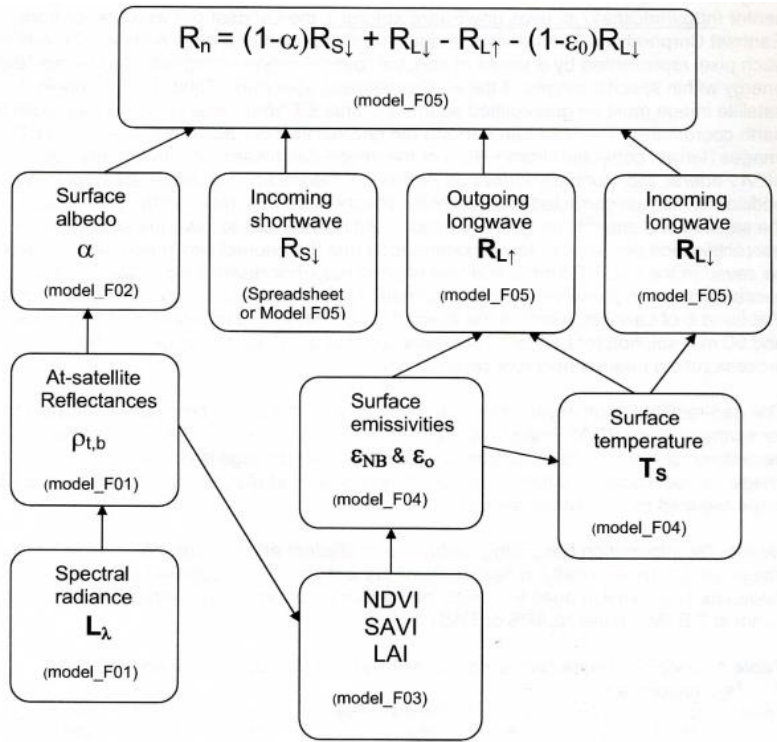
Figure 4.4. R_n flow chart of METRIC model (Allen et al., 2007)

4.2.1.1. Albedo

To calculate R_n, albedo (α) is required. At first, METRIC utilized a determined top of atmosphere reflectance to figure out albedo (Equation [4.24]). The albedo is processed using the consecutive equation (Bastiaanssen et al., 1998):

$$\alpha = \frac{\alpha_{toa} - \alpha_{atm}}{\tau_{oc}^2} \qquad [4.24]$$

where α_{toa} is planetary albedo of each pixel or albedo without atmospheric correction (Equation [4.25]), α_{atm} is atmospheric albedo and τ_{oc} is atmospheric transmittance in the solar radiation domain (Droogers and Allen, 2002; Allen et al., 2007).

$$\alpha_{toa} = \sum_{2}^{7} p_i * r_i \qquad [4.25]$$

α_{toa} is calculated using the albedo coefficients (p_i) and reflectance of each band (r_i). da Silva et al., (2016) suggested coefficients to calculate albedo for Landsat 8 imagery. In Table 4.1 the albedo coefficients utilized in this study are displayed. α_{atm} is taken as 0.03 in (da Silva et al.,2016).

Table 4.1. Albedo coefficients (Silva et al., 2016)

Band	$\rho_{s,blue}$	$\rho_{s,green}$	$\rho_{s,red}$	$\rho_{s,NIR}$	$\rho_{s,SWIR1}$	$\rho_{s,SWIR2}$
coefficient	0.3	0.277	0.233	0.143	0.036	0.012

Then the atmospheric transmissivity map is generated (Equation [4.26]).

$$\tau_{oc} = 0.35 + 0.627 * \exp\left(\frac{-0.00146 * P}{K_t * cosZ} - 0.075\left(\frac{W}{cosZ}\right)^{0.4}\right) \quad [4.26]$$

where;

P = atmospheric pressure (kPa) (Equation [4.27]),

W = atmospheric water content (mm) (Equation [4.28]),

$K_t = 1$ for clean air and Z = sun zenith angle (from satellite image metadata).

$$P = 101.3 * \left(\frac{293 - 0.0065z}{293}\right)^{5.26} \quad [4.27]$$

z = digital elevation model (m).

$$W = 0.14 * e_a * P + 2.1 \quad [4.28]$$

e_a = near surface vapor pressure at the time of the image measured at the weather station (kPa) (Equation [4.29]).

$$e_a = 0.6108 * \exp\left[\frac{17.27 * T_{dew}}{T_{dew} + 237.3}\right] \quad [4.29]$$

Dew point temperature (T_{dew}) is calculated by the average temperature (T) and relative humidity (RH) (Equation [4.30]).

$$T_{dew} = (\frac{RH}{100})^{(\frac{1}{8})} * (112 + (0.9 * T)) + (0.1 * T) - 112 \qquad \text{[4.30]}$$

4.2.1.2. Incoming Short-wave Radiation ($R_{s\downarrow}$)

The solar radiation ($R_{s\downarrow}$) is calculated using Equation [4.31].

$$R_{s\downarrow} = G_{sc} * cos\theta_{adj} * d_r * \tau_{sw} \qquad \text{[4.31]}$$

where;

G_{sc} = solar constant (1367 W/m^2),

$cos\theta_{adj}$ = solar incidence angle adjusted for slope (Equation [4.33]),

$\tau_{sw} = \tau_B + \tau_D$ broadband atmospheric transmissivity,

τ_B = transmissivity index for direct beam radiation (Equation [4.34]),

τ_D = broadband atmospheric transmissivity index (Equation [4.35]),

d_r = inverse squared relative earth-sun distance.

$$\begin{aligned} cos\theta_{unadj} = {} & \sin(\delta)\sin(\phi)\cos(s) - \sin(\delta)\cos(\phi)\sin(s)\cos(\gamma) \\ & + \cos(\delta)\cos(\phi)\cos(s)\cos(\omega) \\ & + \cos(\delta)\sin(\phi)\sin(s)\cos(\gamma)\cos(\omega) \\ & + \cos(\delta)\sin(\gamma)\sin(s)\sin(\omega) \end{aligned} \qquad \text{[4.32]}$$

where;

δ = solar declination (radians),

φ = latitude (radians),

ω = solar time angle (radians),

s = slope (radians),

γ = aspect (radians).

The slope (s) and aspect (γ) maps are generated from Digital Elevation Map.

$$cos\theta_{adj} = cos\theta_{unadj} / cos(s) \qquad [4.33]$$

$$\tau_B = 0.98 * \exp\left(\frac{-0.00146 * P}{K_t * cos\theta} - 0.075\left(\frac{W}{cos\theta}\right)^{0.4}\right) \qquad [4.34]$$

cosθ in Equation [4.34], is the cosine of solar incidence angle.

$$for\ \tau_B \geq 0.15, \tau_D = 0.35 - 0.36 * \tau_B$$
$$for\ \tau_B < 0.15, \tau_D = 0.18 + 0.82 * \tau_B \qquad [4.35]$$

Adding τ_B to τ_D, τ_{sw} is calculated.

4.2.1.3. Outgoing Long-wave Radiation ($R_{l\uparrow}$)

The outgoing long-wave radiation ($R_{l\uparrow}$) depends on the broadband surface emissivity (ε_0), Stefan-Boltzmann constant ($5.67*10^{-8}$ W m^{-2} K^{-4}) and surface temperature (T_s) (Equation [4.36]).

$$R_{L\uparrow} = \varepsilon_0 * \sigma * T_s^4 \qquad [4.36]$$

The broadband surface emissivity differs with LAI (Equation [4.37]). When LAI is more than 3, ε_0 is 0.98. Where for LAI $\leq$ 3;

$$\varepsilon_0 = 0.95 + 0.01 * LAI \qquad [4.37]$$

The vegetation parameters are important to distinguish completely vegetative pixels, water, and dry exposed soil. LAI is determined utilizing Equation [4.38] with a most extreme value restriction of 6.

$$SAVI \leq 0.817 \; için \; LAI = 11 * SAVI^3$$

$$SAVI > 0.817 \; için \; LAI = 6$$

[4.38]

To calculate SAVI, the canopy constant (L) is taken as 0.5 (Allen et al., 2007). SAVI and NDVI are determined utilizing the reflectance of red (r_4) and NIR (r_5) bands (Equations [4.39] and [4.40]).

$$SAVI = (1 + L)(r_5 - r_4)/(L + r_5 + r_4)$$

[4.39]

$$NDVI = (r_5 - r_4)/(r_5 + r_4)$$

[4.40]

The narrowband surface emissivity changes with LAI (Equation [4.41]). For LAI greater than 3, ε_{NB} is 0.98. Where for LAI≤3;

$$\varepsilon_{NB} = 0.97 + 0.0033 * LAI$$

[4.41]

The Landsat 8 satellite image consist of two thermal bands. Both thermal bands are utilized in the calculation of the land surface temperature. First the at-satellite brightness temperatures of each band are calculated (Equation [4.42]). Then the land surface temperature is calculated using at-satellite brightness temperatures (Equation [4.43]).

$$T = \frac{K_2}{\ln\left(\left(\frac{K_1}{L_\lambda}\right) + 1\right)}$$

[4.42]

T is the at-satellite brightness temperature (K), L_λ is the TOA spectral radiance (W m^{-2} sr^{-1} μm^{-1}) and K_1 and K_2 are constants for Landsat images (W m^{-2} sr^{-1} μm^{-1}). For

Landsat 8 thermal bands taken from metadata; K_2 is 1321.1, K_1 is 774.9 for band 10, K_2 is 1201.1, K_1 is 480.9 for band 11.

The TOA spectral radiance of each thermal band is calculated using band-specific constants and the digital numbers (DN) of the thermal images which is explained in details at the USGS website (url2).

The method suggested by Jiménez-Muñoz et al., (2014) is used in the calculation of the surface temperature from Landsat 8 Thermal bands (Equation [4.43]).

$$T_s = T_{10} + 1.378(T_{10} - T_{11}) + 0.183(T_{10} - T_{11})^2 - 0.268 \qquad [4.43]$$
$$+ (54.30 - 2.238w)(1 - \varepsilon) + (-129.20$$
$$+ 16.40w)\Delta\varepsilon$$

where;

T_s is the land surface temperature (K); T_{10} and T_{11} are the at-sensor brightness temperatures for bands 10 and 11 of Landsat 8 (K); ε is the mean emissivity; w is the total atmospheric water vapor content (in $g \cdot cm^{-2}$) and $\Delta\varepsilon$ is the emissivity difference.

Later the T_s is corrected to be used in sensible heat flux calculations, from the DEM of the region with the environmental lapse rate of 0.0065 °C m^{-1} (NOAA, 1976).

4.2.1.4. Incoming Long-wave Radiation ($R_{l\downarrow}$)

The incoming long-wave radiation ($R_{l\downarrow}$) is calculated utilizing the Stefan-Boltzmann constant, the near surface air Temperature (K) and the effective atmospheric emissivity ε_a (Equation [4.44]). Even though there are different opinions about T_a in the METRIC model $T_a = T_s$ is accepted.

$$R_{L\downarrow} = \varepsilon_a * \sigma * T_a^4 \qquad [4.44]$$

The effective atmospheric emissivity (ε_a) is only dependent on τ_{sw} (Equation [4.45]).

$$\varepsilon_a = 0.85 * (-\ln(\tau_{sw}))^{0.09} \qquad [4.45]$$

4.2.2. Soil Heat Flux (G) Calculation

In METRIC model, the soil heat flux (G) which is computed by Tasumi (2003) is typically defined by the pace of heat penetrating the surface. This process computes the proportion of G to R_n evaluating the proportion in noon as a component of surface temperature, albedo, and NDVI. As Bastiaanssen (1995) suggests, G is determined as a segment of the R_n (Equation [4.46]).

$$\frac{G}{R_n} = (T_s - 273.15)(0.0038 + 0.0074\alpha)(1 - 0.98 * NDVI^4) \qquad [4.46]$$

4.2.3. Hot-cold Pixel Selection

The METRIC model, uses two pixels to establish boundary conditions for the surface energy balance. Those anchors are hot-cold pixels. The cold pixel is picked from well-irrigated vegetative regions. The hot pixel is picked from bare agricultural areas where ET is assumed to be very low. The selected hot and cold pixels are verified to be bare soil and vegetation respectively using Google Maps.

According to Allen (2007), anchor pixel selection process requires skill and patience. Also, the anchor pixel selection step greatly affects the results. After selection, the surface temperatures of anchor pixels are stored to be used in the sensible heat flux process.

In the METRIC application, the hot and cold anchors are selected manually using DEM, NDVI and surface temperature (T_s) parameters. Since the elevation of the Eddy-Covariance flux tower which provides meteorological data for the study is at 1478 meters, the hot and cold pixels are selected from 1400 to 1500 meters elevation range to better simulate the environment. NDVI threshold is used as (0.10 - 0.28) for hot pixels, and (0.76 – 0.84) for cold pixels. Finally, the fittest pixels for boundary conditions are selected looking at the surface temperature and terrain type. Anchor

pixels are selected from each satellite image by following the approach explained above.

4.2.4. Sensible Heat Flux (H) Calculation

The sensible heat flux (H) in METRIC model is determined utilizing an iterative method (Equation [4.47]).

$$H = \rho_{air} C_p \frac{dT}{r_{ah}}$$ [4.47]

dT is assessed, as recommended in SEBAL (Bastiaanssen et al., 1998), with a linear relationship of the adjusted surface temperature $T_{s,datum}$ (Equation [4.48]), a noteworthy supposition for evaluating sensible heat (Allen et al., 2005; Bastiaanssen, 1995). The "a" and "b" coefficients in Equation [4.48] are resolved iteratively for hot-cold pixels and those terms are explicit for each satellite imagery as they are presented as

$$dT = a + bT_{s\ datum}$$ [4.48]

$$a = \frac{dT_{hot} - dT_{cold}}{T_{s\ datum\ hot} T_{s\ datum\ cold}}$$ [4.49]

$$b = [dT_{hot} - a]/T_{s\ datum\ hot}$$ [4.50]

The iterative process of sensible heat flux calculation is given in Figure 4.5 (Allen et al., 2007).
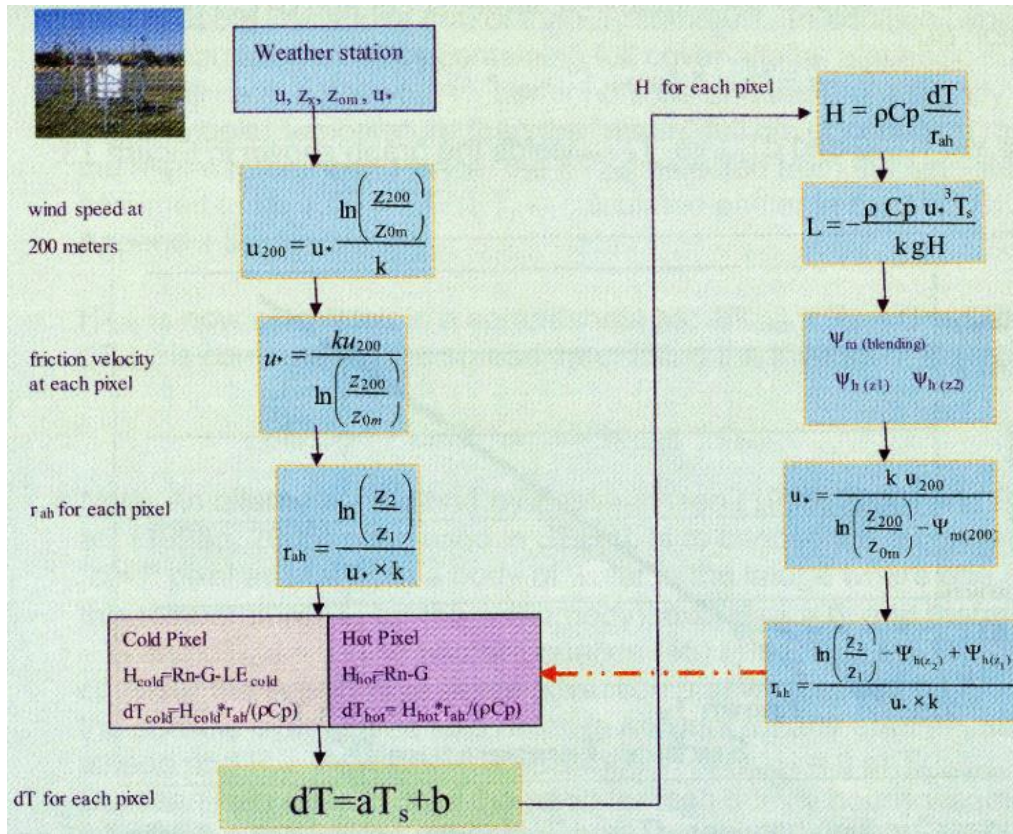
Figure 4.5. Iterative process of sensible heat flux calculation (Allen et al., 2007)

Then the momentum roughness length is corrected for mountainous terrain using the slope map given in Equation [4.51].

$$z_{om\_min} = z_{om}(1 + \frac{(\frac{180}{\pi})s - 5}{20})$$ [4.51]

As another mountainous area correction, the wind speed weight constant (ϖ) (Equation [4.52]) is multiplied with u_{200} before any further steps.

$$\varpi = 1 + 0.1(\frac{Elevation - Elevation_{station}}{1000})$$ [4.52]

where; z_x is the meteorological station wind data gathering height and u_w is the wind speed data taken from Eddy-Covariance flux tower. z_{omw} is the surface roughness length at the Eddy-Covariance flux tower. Then, the results of the Equation [4.53] and ϖ are multiplied to create the 200 meters' altitude wind speed (u_{200}) map as

$$u_{200} = \frac{u_w \ln\left(\frac{200}{z_{omw}}\right)}{\ln\left(\frac{z_x}{z_{omw}}\right)} \qquad [4.53]$$

In Equation [4.54] the friction velocity u_* is calculated, and $k = 0.41$ is the von Karman constant.

$$u_* = \frac{k u_{200}}{\ln\left(\frac{200}{z_{om}}\right)} \qquad [4.54]$$

Then the aerodynamic resistance to heat transfer (r_{ah}) map is generated (Equation [4.55]). The reference heights related to aerodynamic resistance z_1 and z_2 are generally taken as 0.1 and 2 meters respectively.

$$r_{ah} = \frac{\ln\left(\frac{z_2}{z_1}\right)}{k u_*} \qquad [4.55]$$

The air density is important for sensible heat flux calculations (Equation [4.56]). R is the specific gas constant (287 J kg^{-1} K^{-1}).

$$\rho_{air} = \frac{1000 * P}{1.01 * (T_s - dT)R} \qquad [4.56]$$

4.2.5. LE, Instantaneous ET and Reference ET Fraction (fRET) Calculations

The latent heat flux which signifies the energy consumed by ET is calculated by using Equation [4.57]:

$$LE = R_n - G - H \qquad \text{[4.57]}$$

where LE is the instantaneous latent heat flux (W/m^2) at satellite overpass at 11:30 am.

The instantaneous ET (mm/hr) is calculated with latent heat flux (LE) and latent heat of vaporization (λ) as a residual of the energy balance (Equation [4.58]):

$$ET_{inst} = 3600\frac{LE}{\lambda} \qquad \text{[4.58]}$$

The latent heat of vaporization (J/kg) is calculated using the surface temperature (Equation [4.59]):

$$\lambda = \big(2.501 - 0.00236(T_s - 273)\big) * 10^6 \qquad \text{[4.59]}$$

The reference ET fraction (ET$_r$F) is calculated by dividing the instantaneous ET to the hourly reference evapotranspiration (ET$_r$) estimated by the Penman-Monteith equation (Equation [4.60]).

$$ET_rF = \frac{ET_{inst}}{ET_r} \qquad \text{[4.60]}$$

The daily ET (mm/day) is calculated by multiplying the reference ET fraction by the daily reference evapotranspiration also calculated by the Penman-Monteith equation (Equation [4.61]).

$$ET_{24} = ET_rF * ET_{r\_24} \qquad \text{[4.61]}$$

Usually the daily ET map is obtained at this point. However, for mountain regions one more step is needed. C$_{rad}$ the radiation correction constant is calculated for each image and every pixel as

$$C_{rad} = \frac{R_{so(inst)Hor}}{R_{so(inst)Pixel}} * \frac{R_{so(24)Pixel}}{R_{so(24)Hor}} \qquad [4.62]$$

where the R_{so} is the solar radiation, "inst" means at satellite overpass and "24" means daily average. Duffie and Beckman (1991) suggested the C_{rad} equation and Allen et al. (2006) developed the equation to fit daily periods. In this study 1-hour time increment has been used for the calculation of daily averages. Finally, the C_{rad} is multiplied with ET_{24} to create the final product.

4.3. R-METRIC

Both METRIC (Allen et al., 2007) and R-METRIC (Olmedo et al.,2016) models have similar steps to generate daily actual ET maps. But they have some parameters that are calculated by different methods and equations. In this section those differences will be mentioned.

4.3.1. R-Albedo

In R-METRIC model, albedo calculation from Landsat 8 satellite images needs the constants given in Table 4.2 It is observed that the albedo calculated by R-METRIC model is lower than the values calculated by METRIC model (Table 4.1).

Table 4.2. Albedo coefficients (Olmedo et al.,2016)

Band	$\rho_{s,blue}$	$\rho_{s,green}$	$\rho_{s,red}$	$\rho_{s,NIR}$	$\rho_{s,SWIR1}$	$\rho_{s,SWIR2}$
coefficient	0.246	0.146	0.191	0.304	0.105	0.008

4.3.2. R-Surface Roughness Length

The surface roughness length (z_{om}) in R-METRIC is calculated as in the original METRIC model, depending on LAI (Equation [4.63]). The minimum value of z_{om} is set to be 0.005 meters.

$$z_{om} = 0.018 * LAI \qquad [4.63]$$

4.3.3. R-METRIC Hot-cold Pixel Selection

The anchor pixels are selected automatically when utilizing the R-METRIC model. In this selection albedo, LAI, NDVI, surface roughness length (z_{om}) and surface temperature (T_s) values are considered. The automated anchor pixel selection criteria of R-METRIC model are given in Table 4.3. Since the surface temperature depends on season it is not given as a parameter. Surface roughness length will be explained in more detail in the next chapter. The advantage of automated selection is possibility to have less human error. But as a disadvantage automated pixel selection is much more susceptible to cloudy images sometimes preferring cloud shadows as cold (wet) anchor pixels. So, a cloud mask is needed at the beginning to be able to work with automated pixel selection method. Whereas with the manual selection method the cloud mask can be applied after seeing the results since hot-cold pixels would not be selected from cloudy pixels. Five of each anchor pixels are selected in the automated process to reduce the effect of outlier pixels. The averages of anchor pixels are taken into consideration.

Table 4.3. R-METRIC anchor pixel selection criteria (Olmedo et al., 2016)

Variable	Cold pixel	Hot pixel
albedo*	0.18 - 0.25	0.13 - 0.15
NDVI*	0.76 - 0.84	0.10 - 0.28
LAI ($m^2 \cdot m^{-2}$)	3 - 6	-
Z_{om} (m)	0.03 - 0.08	≤ 0.005

CHAPTER 5

ANALYSES

The analyses performed in this study aim to generate the ET maps in mountainous region. The methods were explained in previous chapters. The METRIC model and R-METRIC model both require cloudless satellite images for better performance. Since the cloud is watched out in the manual hot-cold pixel selection of METRIC model, the cloud mask can be applied at the end of the process. However, as a drawback of the automated hot-cold pixel selection of R-METRIC, unless a cloud mask is implemented to the input satellite image the hot-cold pixel can be chosen from cloud shadow. This event causes creation of inaccurate ET maps.

The calculation of the Penman-Monteith reference ET is presented in this chapter. Next a quality study has been performed for all 43 Landsat 8 satellite images using the quality band to avoid inaccuracy. Then the METRIC and R-METRIC model analyses were implemented as explained in Chapter 4. All the calculations are presented on the image of 27 June 2017 as an example. Finally, the results are compared with the Eddy-Covariance tower flux data where surface energy balance is considered.

5.1. Reference Evapotranspiration

METRIC model needs hourly and daily reference ET values calculated on the surface (Allen et al., 2007). In this study, reference ET values are calculated utilizing the standardized Penman-Monteith equation (ASCE-EWRI, 2005). The inputs of hourly reference ET are incoming short-wave radiation, average temperature, average wind speed and dew point temperature, while daily reference ET inputs are daily average incoming short-wave radiation, daily max. and min. temperature, daily max. and min. relative humidity, daily average wind speed (Table 5.1). The meteorological data

required for the reference ET study are measured at the Eddy-Covariance flux tower. The hourly reference ET value is calculated by using the Eddy-Covariance flux tower data at the time the satellite image was captured. The satellite image was acquired on 27 June 2017 at 11:21:38. Therefore, the data of 11:30 is used in the hourly reference ET calculation. One or two stations are usually sufficient to calculate the reference ET in a Landsat image (Allen et al., 2007). The calculation process of the daily and hourly reference ET is explained for the image of 27th June 2017.

Table 5.1. Meteorological data used to calculate reference ET for the date 27.06.17

27 June 2017	Daily Meteorological Data	Meteorological Data at 11.30
2m height average wind speed (m/s)	1.89	2.17
Average Temperature (°C)	-	27.18
Average Relative Humidity (%)	-	25.95
Dew point Temperature Td (°C)	-	6.01
Solar Radiation (MJ m^{-2} d^{-1}, MJ m^{-2} h^{-1})	32.16	3.56
Max. Temperature(°C)	30.31	-
Min. Temperature(°C)	16.75	-
Max. Relative humidity (%)	50.74	-
Min. Relative humidity (%)	19.85	-
Penman reference ET$_r$ (mm d^{-1}, mm h^{-1})	9.13	0.91

5.1.1. Penman-Monteith Parameters

In Table 5.2 the C_n and C_d constant values are given for daily and hourly alfalfa reference ET calculations (ASCE-EWRI, 2005).

Table 5.2. C_n and C_d constants for alfalfa

Reference ET (ET_r)	C_n	C_d
Daily	1600	0.38
Hourly (daytime)	66	0.25
Hourly (nighttime)	66	1.7

In Equation [4.2], the elevation value (z) is 1478 meters and the atmospheric pressure value (P) is calculated as 85.0 kPa. The psychrometric constant (γ) for the atmospheric pressure of 85.0 kPa is calculated as 0.057 kPa °C^{-1} (Equation [4.3]).

The average temperature value for the daily reference ET calculation is the mean of the daily highest and lowest temperature, while the average temperature for the hourly reference is calculated as the average temperature of the time the satellite image was taken. For example, the daily average temperature for the selected image is 23.53 °C or 296.68 K, while the average temperature at 11:30 am is 27.18 °C or 300.33 K. The maximum and minimum temperatures for 27 June 2017 are 30.31 °C and 16.75 °C, respectively. For daily applications, the saturation vapor pressure is calculated as an average of saturation vapor pressures for daily maximum and minimum temperatures. After computing $e(T_{max}) = 4.32$ kPa and $e(T_{min}) = 1.91$ kPa daily saturation vapor pressure (e_s) is calculated as 3.114 kPa. The hourly saturation vapor pressure (e_s) is calculated with Equation [4.4] and it is calculated with hourly average temperature ($e(T_{ave})$ = hourly e_S = 3.604 kPa).

The daily and hourly slope of the saturation vapor pressure-temperature curves (Δ) are calculated as $\Delta_{daily} = 0.175$ kPa °C^{-1} and $\Delta_{hourly} = 0.21$ kPa °C^{-1} (Equation [4.5]). The actual daily vapor pressure is calculated as $e_a = 0.913$ kPa (Equation [4.6]). For 27 June 2017 the hourly actual vapor pressure for an average relative humidity of 25.95% is calculated as $e_a = 0.936$ kPa (Equation [4.7]). The vapor pressure deficit (e_s-e_a) used in the Penman-Monteith equation is 2.201 for daily and 2.668 for hourly calculations.

Daily extraterrestrial radiation is calculated as 41.7 MJ m^{-2} d^{-1} (Equation [4.8]). The inverse relative distance factor for the earth-sun (d_r) is calculated as 0.967 (Equation [4.9]). The solar declination (δ) is 0.407 and the sunset hour angle (ω_s) is 1.908 (Equations [4.10] and [4.11]). Hourly extraterrestrial radiation (R_a) is calculated as 2.42 MJ m^{-2} h^{-1} (Equation [4.12]). The solar time angle at beginning of period (ω_1) and the solar time angle at end of period (ω_2) are calculated as -0.330 and -0.068 respectively (Equations [4.13] and [4.14]). The solar time angle (ω) is -0.199 (Equation [4.15]). The seasonal correction for solar time (S_c) is -0.060 (Equation [4.16]).

The daily clear-sky radiation (R_{so}) is calculated as 32.51 MJ m^{-2} d^{-1} and the hourly clear-sky radiation is calculated as 1.887 MJ m^{-2} h^{-1} (Equation [4.17]). The solar radiation (R_s) is measured at the Eddy-Covariance flux tower. The daily average solar radiation (R_s) is 28.8 MJ m^{-2} d^{-1} and the hourly average solar radiation (R_s) is 3.56 MJ m^{-2} h^{-1}. The net short-wave radiation (R_{ns}) is calculated as 24.76 MJ m^{-2} d^{-1} for daily and 2.74 MJ m^{-2} h^{-1} for hourly calculations (Equation [4.18]). The daily R_{nl} is calculated as -7.74 MJ m^{-2} d^{-1} while hourly R_{nl} is -0.34 MJ m^{-2} h^{-1} (Equation [4.19]).

Finally, the daily R_n is calculated to be 17.02 MJ m^{-2} d^{-1}, while the hourly R_n is 2.40 MJ m^{-2} h^{-1} (Equation [4.20]). The soil heat flux (G) is accepted to be 0 for daily calculations. Hourly soil heat flux (G) is calculated as 0.096 MJ m^{-2} h^{-1} (Equation [4.21]).

5.2. Quality Study

When R-METRIC model is used, without any cloud mask it is easy to have hot-cold pixels selected from cloud shadows. As an example, the 4th June 2017 application is displayed in Figure 5.1.

There are 13 cloudless and four partly cloudy (around 10 % over the study basin) satellite images used in the METRIC model. However, for the additional 26 satellite images used in R-METRIC model the cloud percentage is not taken into account.

Because the purpose of those images is to understand the seasonal trend where cloudless satellite images are few and insufficient. Looking at cloudy satellite images, the cloudy pixel percentage can be seen as high as 48 %.

Hot-cold pixels are automatically selected from the cloud and shadows in 10 satellite images, so masks are applied to those pixels before applying the R-METRIC model. With this model, 43 satellite images are displayed between years 2017 and 2018. The distribution of automatically selected hot-cold pixels dated 4 June 2017 are shown in Figure 5.1, cold and hot pixels can be selected from cloud shadows. This can be seen as a disadvantage of automated pixel selection. In order to prevent this situation, a mask is applied using Landsat 8 quality band.
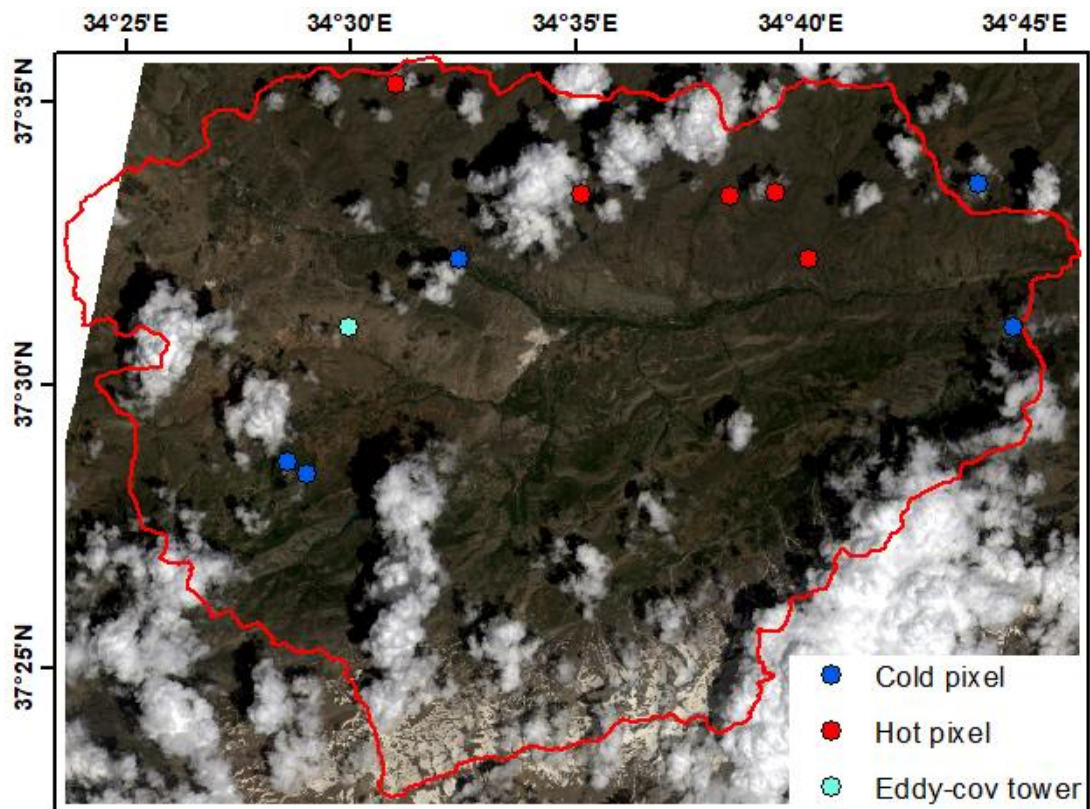
Figure 5.1. Automatically selected hot-cold pixels and the RGB satellite image dated 4 June 2017

51

The quality values of the Landsat 8 quality band are given in Table 5.3 (Guide, 2018). Cloud shadow, ice/snow and cloud pixel values of Landsat 8 quality band are masked in this study. Among the masked pixel values the most populated ones are 328, 352, 368 and 480.

Table 5.3. Landsat 8 quality band pixel values (Guide, 2018)

Attribute	Pixel Value
Fill	1
Clear	322, 386, 834, 898, 1346
Water	324, 388, 836, 900, 1348
Cloud shadow	328, 392, 840, 904, 1350
Snow/ice	336, 368, 400, 432, 848, 880, 912, 944, 1352
Cloud	352, 368, 416, 432, 480, 864, 880, 928, 944, 992
Low confidence cloud	322, 324, 328, 336, 352, 368, 834, 836, 840, 848, 864, 880
Medium confidence cloud	386, 388, 392, 400, 416, 432, 898, 900, 904, 928, 944
High confidence cloud	480, 992
Low confidence cirrus	322, 324, 328, 336, 352, 368, 386, 388, 392, 400, 416, 432, 480
High confidence cirrus	834, 836, 840, 848, 864, 880, 898, 900, 904, 912, 928, 944, 992
Terrain occlusion	1346, 1348, 1350, 1352

Figure 5.2 shows the masked satellite image of June 4, 2017 and new hot-cold pixels selected by R-METRIC. Although the METRIC model is designed for cloudless images, the METRIC model is not affected by the cloud unless hot-cold pixels are selected from pixels such as shadows, ice, and clouds. However, cloud and shadow pixels should be masked for daily ET maps that are output of METRIC model as they will also give incorrect results. The automated hot-cold pixel parameters before and after the quality mask are illustrated in Table 5.4. Where the average height of cold pixels did not change (1415 meters), the effect of masking cloud shadows can clearly be observed increasing the cold pixel's surface temperature average by 4 Kelvin. Since anchor pixels have a huge impact on sensible heat flux calculation, this temperature change is significant.
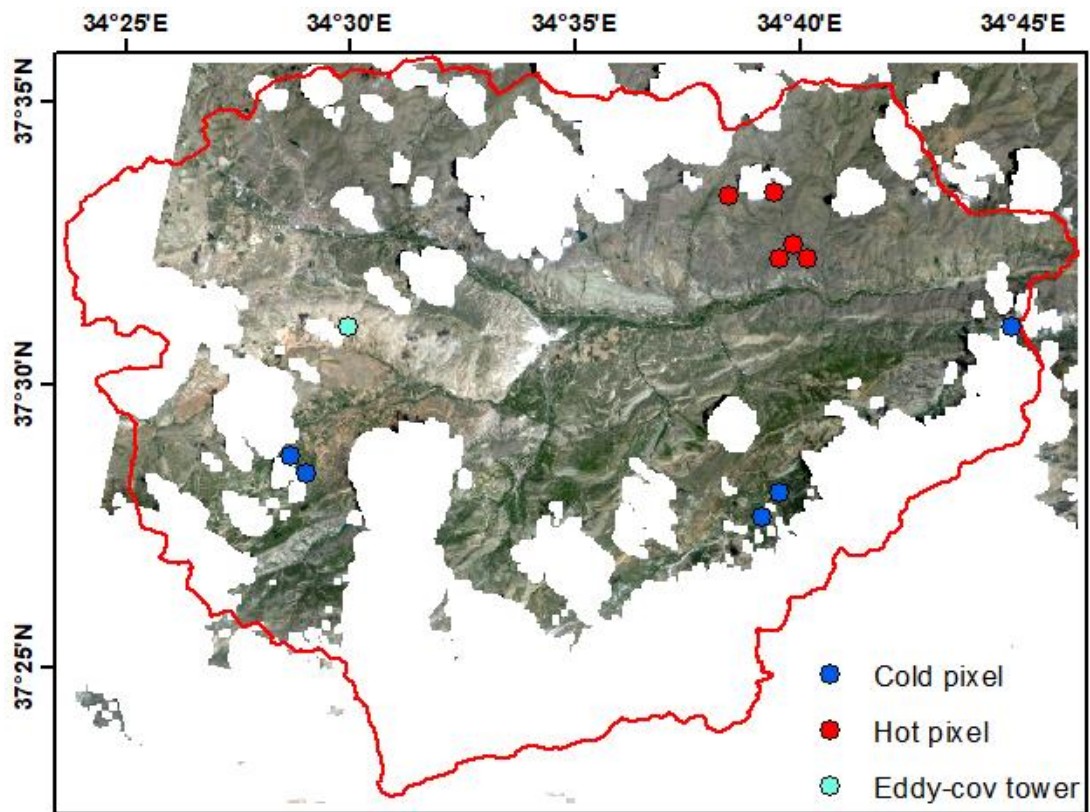
Figure 5.2. Cloud masked RGB image and new automatically selected hot-cold pixels dated 4 June 2017

Table 5.4. 4th June 2017 hot-cold pixels values before and after applying the cloud mask

	type	z_{om} (m)	T_s (K)	LAI	NDVI	albedo
Without mask	hot	0.004	325.4	0.12	0.24	0.14
	cold	0.070	293.8	3.85	0.70	0.19
With QA mask	hot	0.003	324.5	0.12	0.24	0.14
	cold	0.071	297.7	3.95	0.71	0.20

5.3. METRIC Model

The METRIC model was explained in section 4.2. The analyses done using this model for the image of 27 June 2017 are illustrated in Figures 5.3-5.22. The values at the Eddy-Covariance flux tower pixel together with the equations used are displayed with

those figures for better understanding. Since the Eddy-Covariance flux tower is the main station, comparison of the results of the methods with the results obtained at this station is essential for this study. The RGB Landsat 8 image dated 27 June 2017 together with METRIC model hot-cold pixels and Eddy-Covariance flux tower location is given in Figure 5.3. The study basin boundary is illustrated as red polygon while the hot, cold pixels and Eddy-Covariance flux tower are red, blue and teal points, respectively.
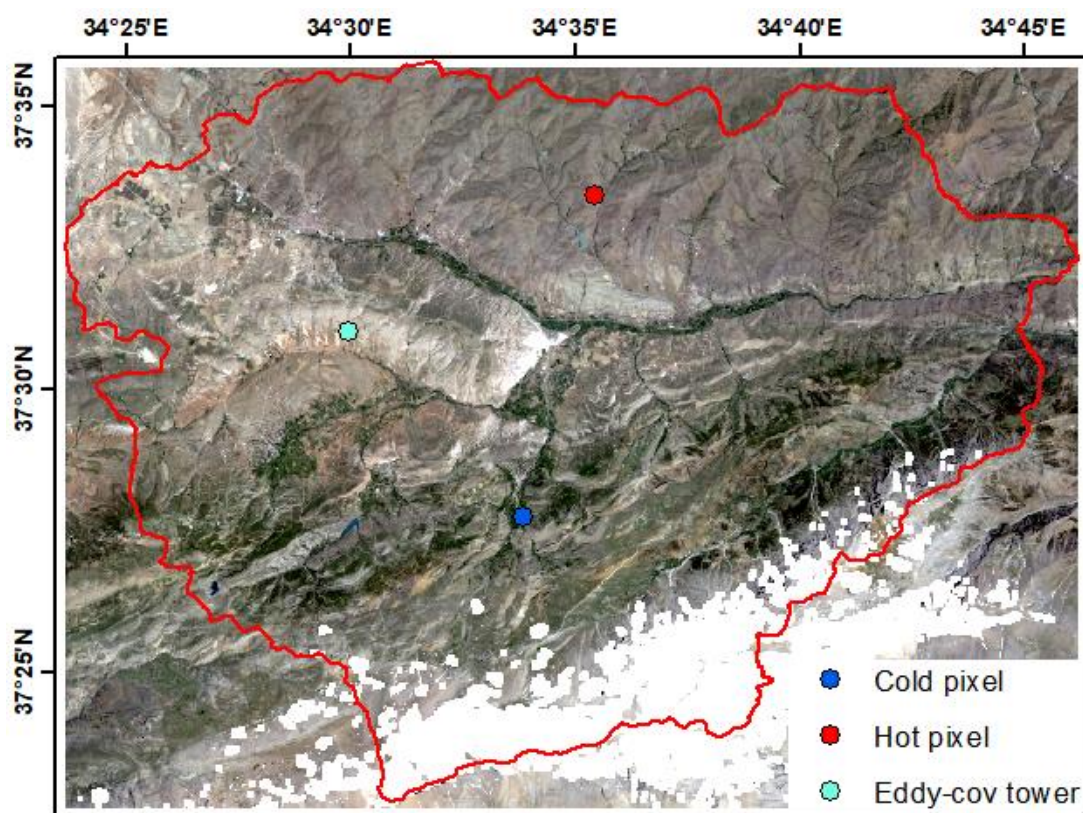
Figure 5.3. RGB Landsat 8 image with METRIC model hot-cold pixels and Eddy-Covariance flux tower

The albedo calculation is explained in detail in section 4.2.1.1. The albedo coefficients of da Silva et al. (2016), are used for the METRIC model. The albedo at Eddy station is calculated as 0.30 which is an expected value for non-irrigated arable lands, dry

bare soil and short crops in the surrounding (Figure 5.4). Also, it can be noted that a gypsum mine is located not far from the Eddy station which seems to have an effect on the region. The blue part in the middle of Figure 5.4 is caused by the gypsum mine with high reflectivity. The average albedo of the basin is found as 0.15.
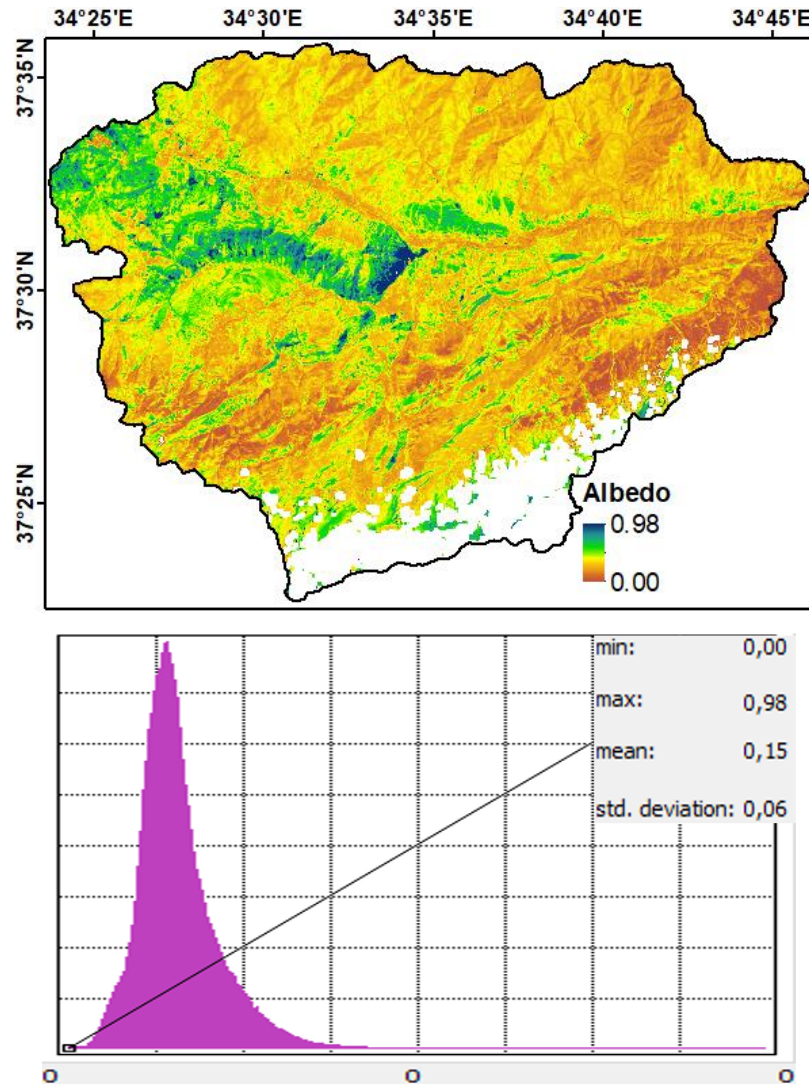

Figure 5.4. Albedo map generated from METRIC model

The incoming short-wave radiation calculation is explained in section 4.2.1.2. in detail. The Eddy station value for incoming short-wave radiation is obtained as 1027 W/m^2 (Figure 5.5). This value is mainly high due to south-east aspect which is dominant at satellite pass time that is around 11:30 am.
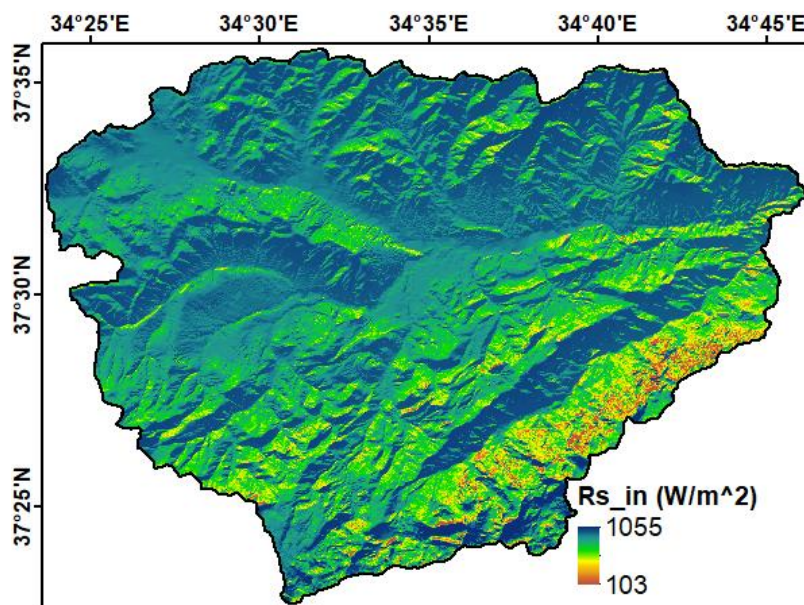
Figure 5.5. Incoming short-wave solar radiation map generated from METRIC model

As stated before the location of Eddy-Covariance tower lacks vegetation cover which is proved with low 0.25 NDVI, 0.21 SAVI and 0.10 LAI values presented in Figures 5.6-5.8.
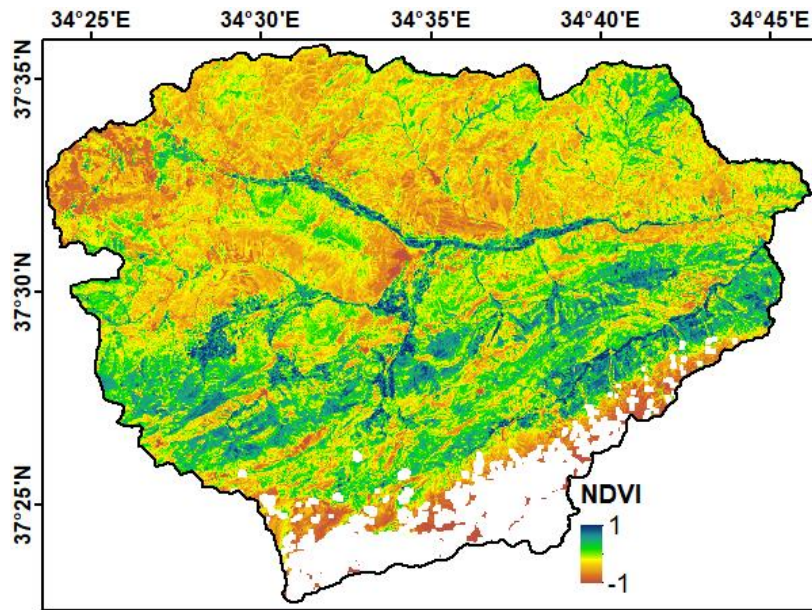
Figure 5.6. Normalized difference vegetation index (NDVI) map generated from
METRIC model
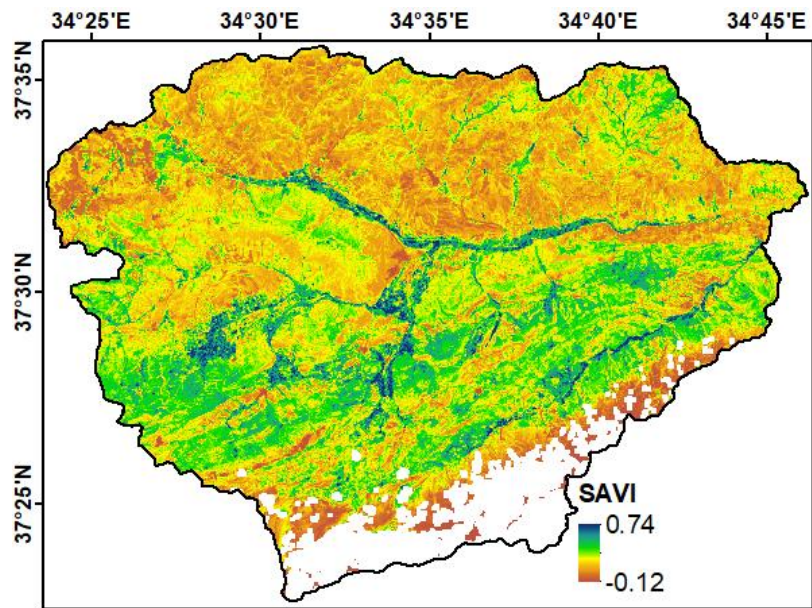
Figure 5.7. Soil-adjusted vegetation index (SAVI) map generated from METRIC
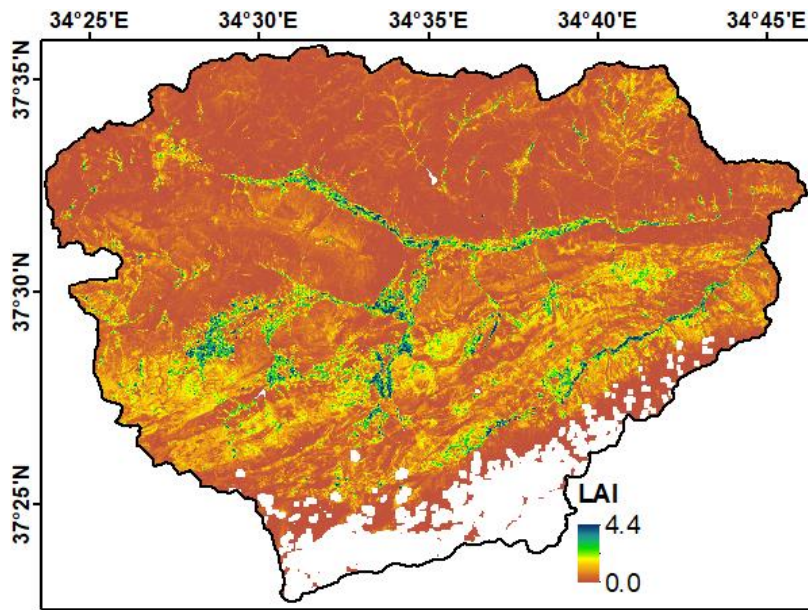model

Figure 5.8. Leaf area index (LAI) map generated from METRIC model

Surface temperature is determined by using the thermal bands of Landsat 8 satellite image (Figure 5.9). In order to be used in sensible heat flux calculations, the surface temperature map is corrected with Digital Elevation Model (Figure 5.10). The global lapse rate of 6.5 K/km is implemented and the datum is selected as the location of Eddy-Covariance flux tower. This causes Ts and Ts_dem to be equal at the selected datum, (1478 meters) as 318 Kelvin.
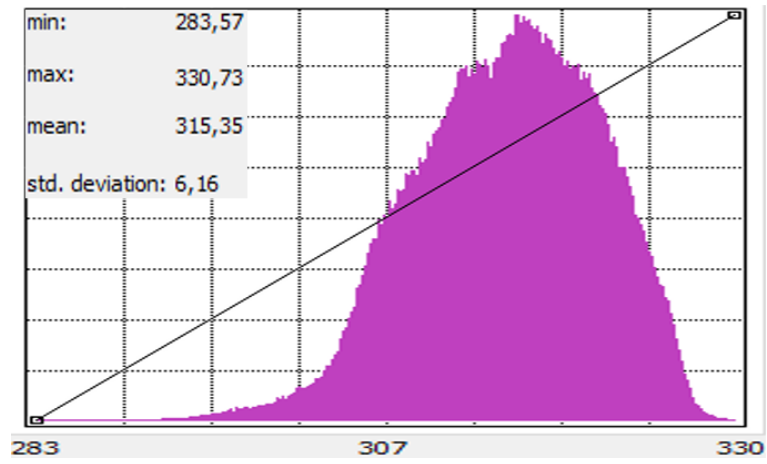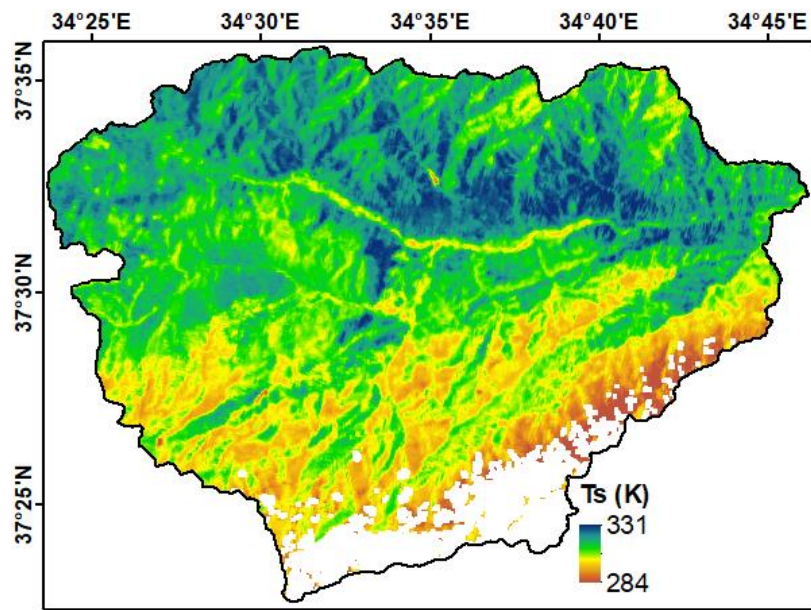
Figure 5.9. Surface Temperature map generated from METRIC model
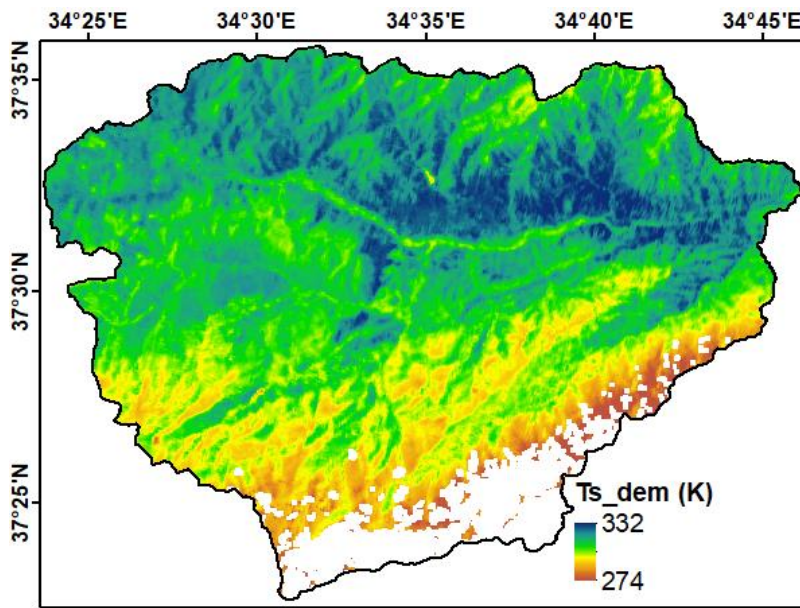
Figure 5.10. DEM corrected surface temperature map, 1478 m datum

The outgoing long-wave and incoming long-wave radiation maps are obtained (Figure 5.11-Figure 5.12). With the surface temperature being high, the outgoing long-wave radiation at Eddy station is as high as 555 W/m^2 (Figure 5.11). The incoming long-wave radiation at Eddy station is calculated as 438 W/m^2 (Figure 5.12).
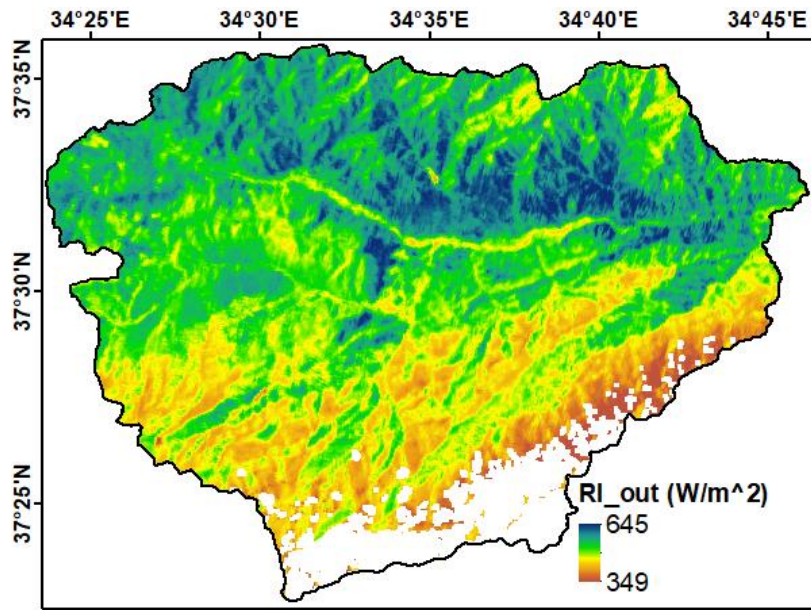
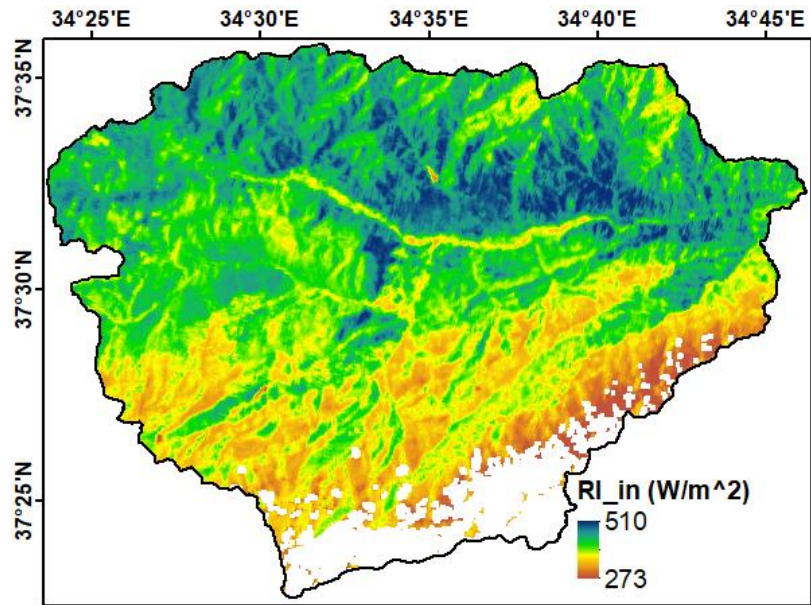Figure 5.11. Outgoing long-wave radiation map generated from METRIC model

Figure 5.12. Incoming long-wave radiation map generated from METRIC model

The R_n map is calculated using albedo, outgoing long-wave radiation, solar radiation and incoming long-wave radiation by using Equation [4.23]. The R_n at Eddy tower is calculated as 585 W/m², which diminishes due to high albedo of the region around the Eddy tower (Figure 5.13).
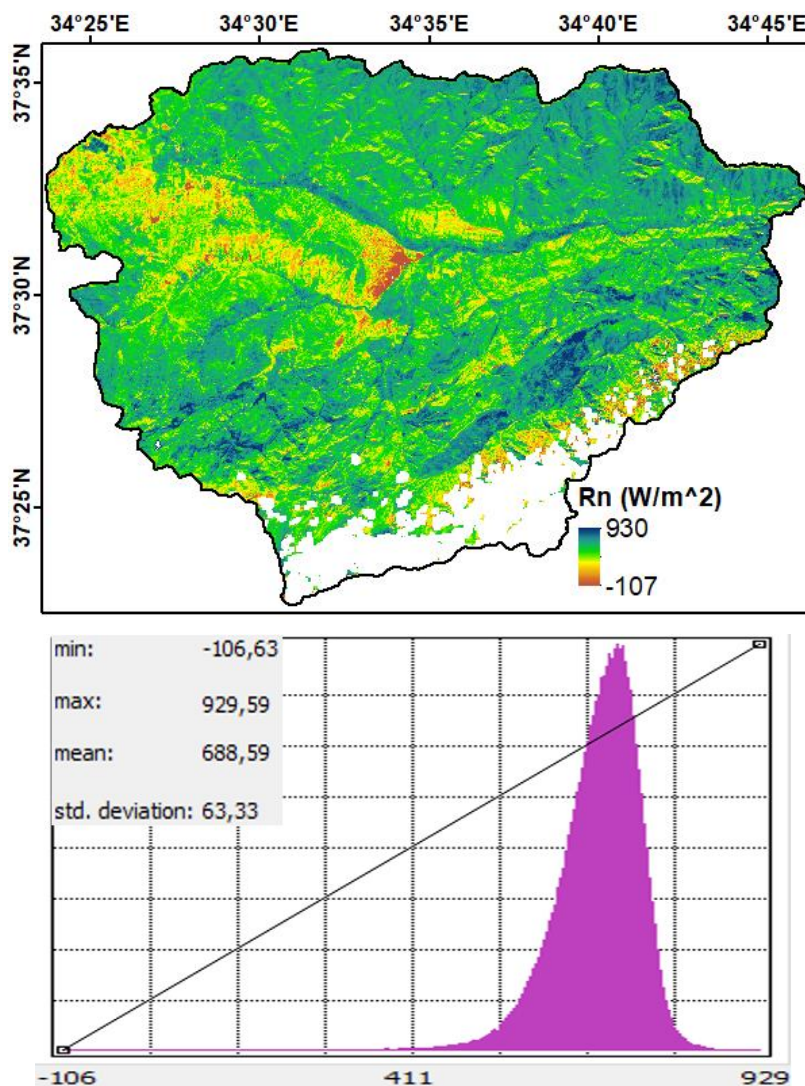

Figure 5.13. R_n map generated from METRIC model

The soil heat flux map is generated depending on R_n, T_s, albedo and NDVI [4.46]. G value is calculated as 158 W/m^2 at Eddy tower (Figure 5.14).
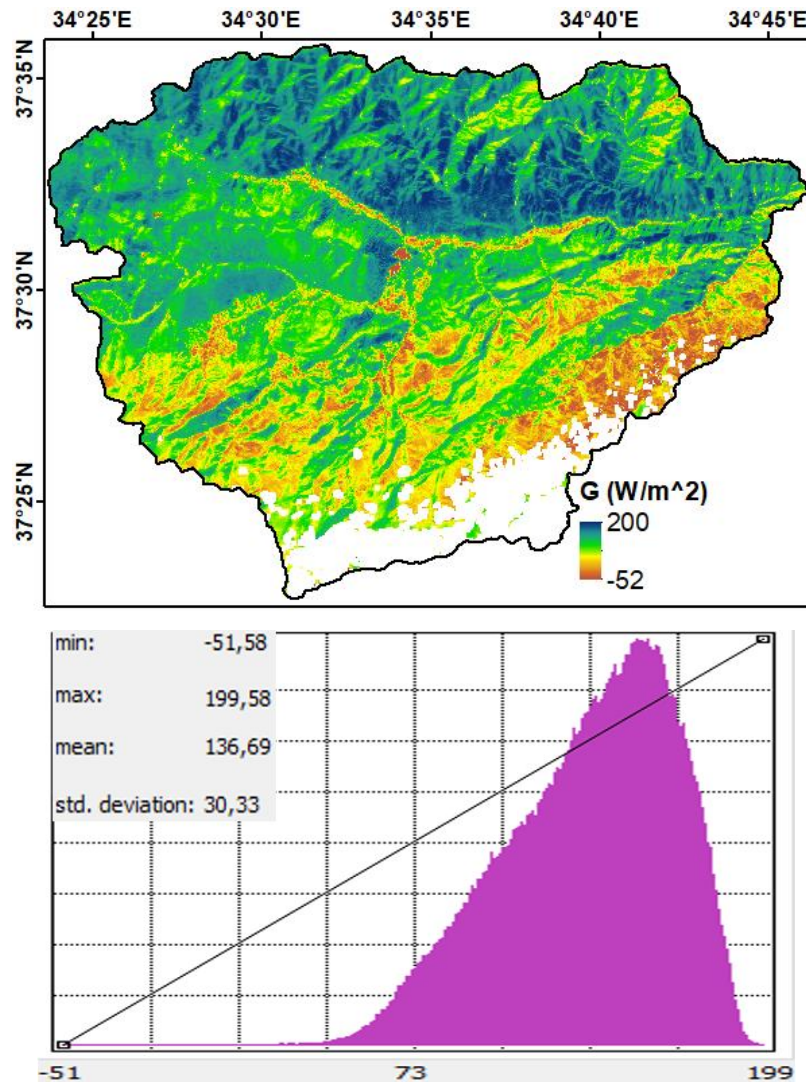

Figure 5.14. Soil heat flux (G) generated from METRIC model

The land cover in Çakıt basin is heterogeneously distributed. Main land cover is natural vegetation, fruit trees and forests. Due to the heterogeneity of land cover, it is

preferred to use CORINE Land Cover Class map dated 2018 in this study (Silva et al., 2007). For water pixels z_{om} becomes 0.001.

After the mountain correction of METRIC model, the surface roughness length at Eddy tower is calculated as 0.061 meters (Equation [4.51]) (Figure 5.15).
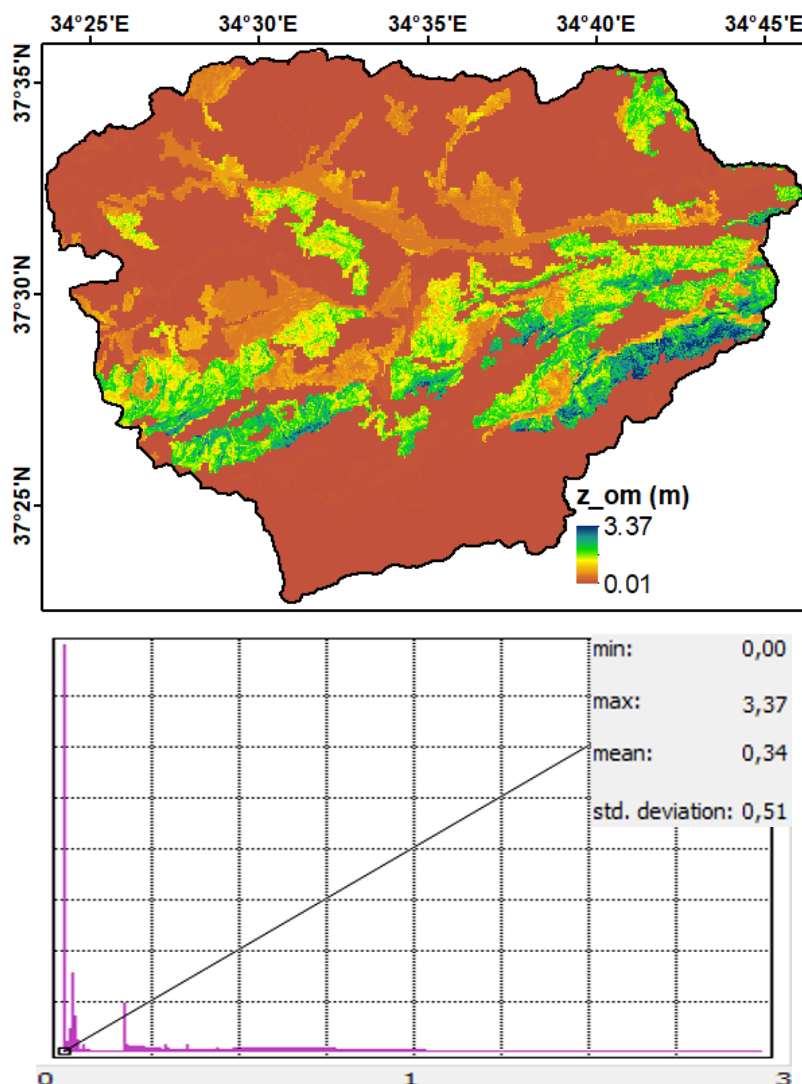

Figure 5.15. Surface roughness length map from Corine 2018 with mountain correction of METRIC model

64

The air density is important for sensible heat flux calculations. The air density at Eddy tower is calculated as 0.92 kg/m (Figure 5.16).
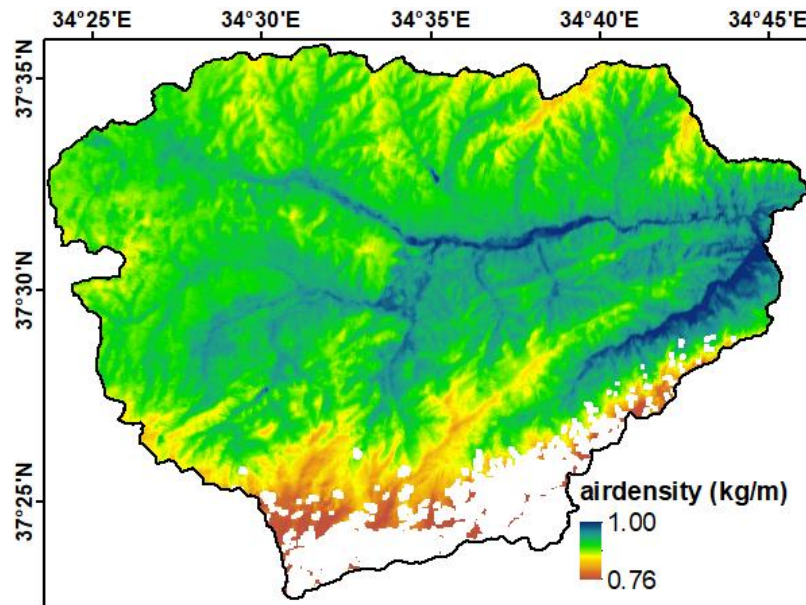

Figure 5.16. Air density map generated from METRIC model

The near-surface temperature difference at Eddy tower is calculated as 5.72 K (Figure 5.17).
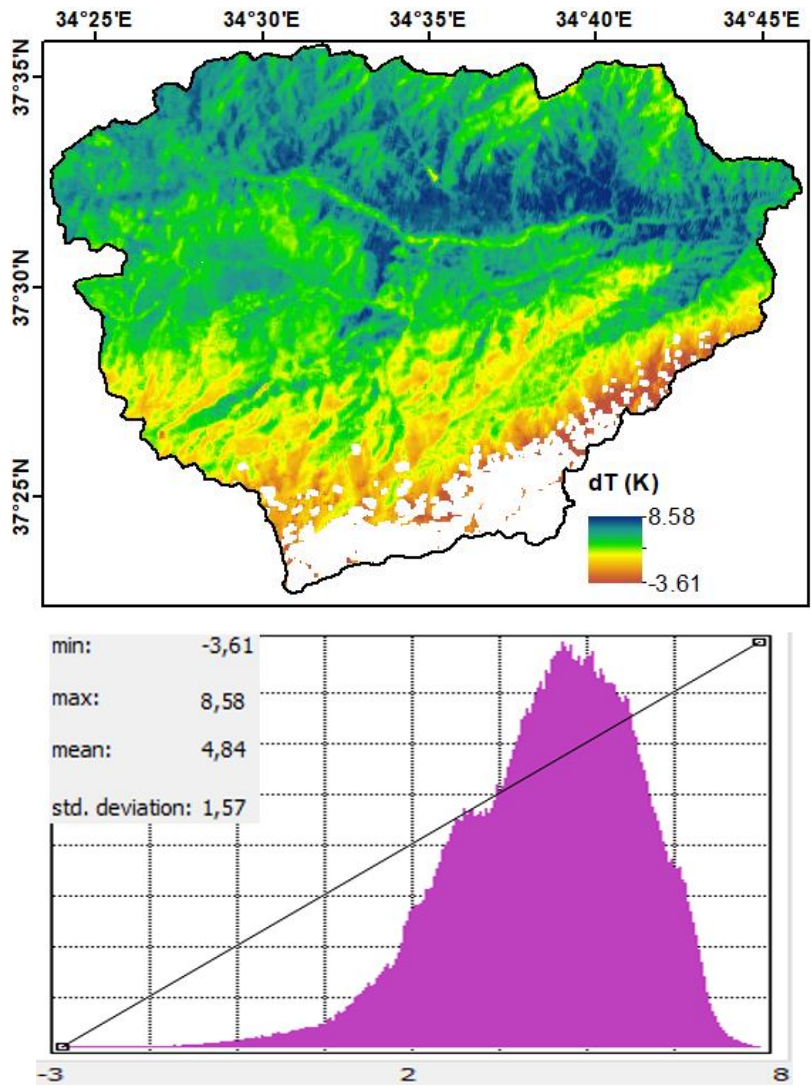
Figure 5.17. Near surface temperature difference (dT) map generated from METRIC model

The sensible heat flux for METRIC model is calculated by using the near-surface temperature difference (dT), the specific heat of air at constant pressure C_p, the aerodynamic resistance r_{ah} and the air density ρ_{air} (Equation [4.47]). High sensible heat flux means that lower energy remaining is used by latent heat flux (LE). The sensible heat flux at Eddy tower after 13th iteration is calculated as 391 W/m^2 (Figure 5.18).

The parameters of two different anchor pixel selection methods for the image of 27.06.2017 are given in Table 5.5.

Table 5.5. Manual anchor pixel selection parameters for 27.06.2017

type	z_{om} (m)	T_s (K)	LAI	NDVI	albedo
hot	0.01	327.63	0.01	0.16	0.14
cold	0.10	305.20	1.80	0.83	0.09

The hot pixel is characterized by being dry and hot, with low NDVI and high surface temperature. Since it is dry, the reference $LE_{hot} = 0.1 * ET_r * \lambda$ is considered in this study. The feature of the cold pixel is that it is wet and cold. Since the energy is spent on ET in the cold pixel, the surface temperature is lower and the NDVI is high. Reference $LE_{cold} = 1.05 * ET_r * \lambda$ is considered (Allen et al., 2007). ET_r is the hourly reference ET value found using meteorological station data. The values of the R_n, soil heat flux, aerodynamic resistance and air density maps in the hot and cold pixels are noted in an excel file.
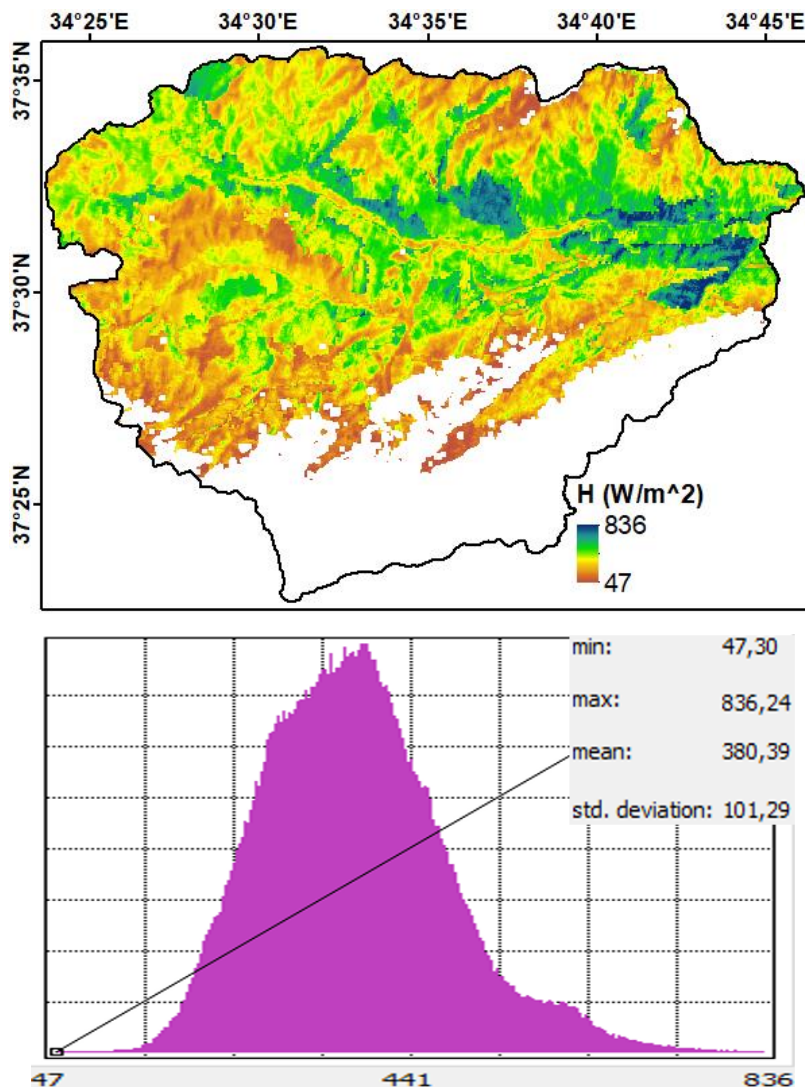
Figure 5.18. Sensible heat flux map generated after 13th iteration from METRIC
model

Instantaneous ET is determined for satellite passing time utilizing the latent heat of
vaporization and latent heat flux (Figure 5.19). At Eddy tower the latent heat flux is
calculated as 36 W/m^2 while the instantaneous ET at satellite pass is calculated as 0.05
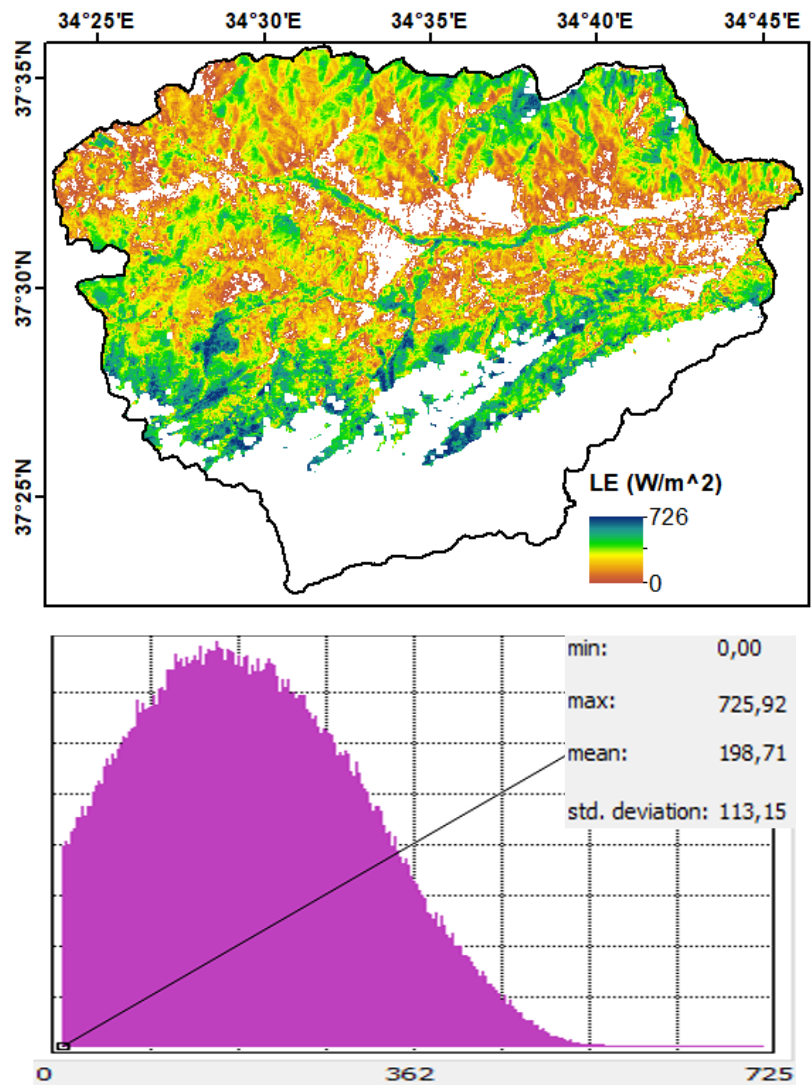mm/hr (Figure 5.20).

Figure 5.19. Latent heat flux map generated as residual of surface energy balance of METRIC model
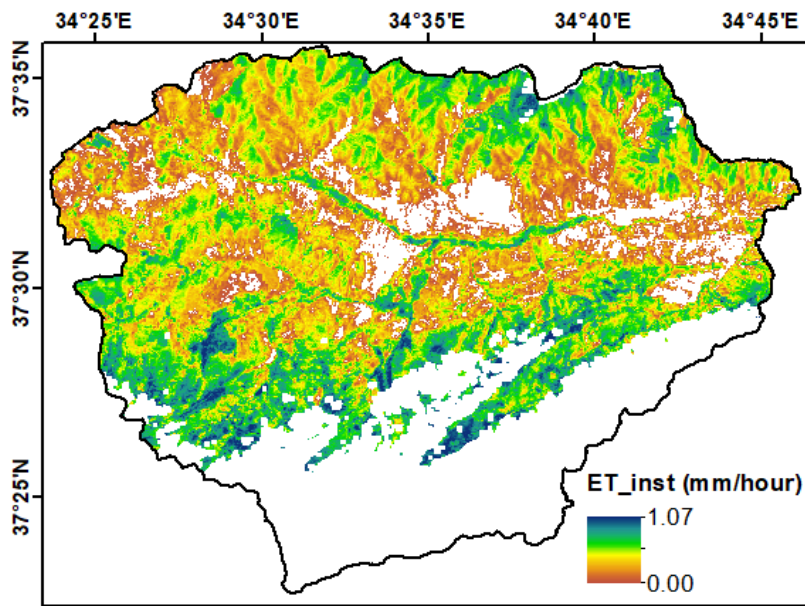
Figure 5.20. Instantaneous ET generated from METRIC model

As explained in section 4.1.5. the daily ET is calculated by using instantaneous ET with solar radiation correction coefficient (C_{rad}) and reference ET fraction (ET_rF). First the reference ET fraction is multiplied to generate daily ET map (Figure 5.21), then the solar radiation correction coefficient is introduced to observe the effect of mountain correction (Figure 5.22). The daily ET values at Eddy tower are obtained as 0.51 mm/day and 0.50 mm/day after mountain correction.
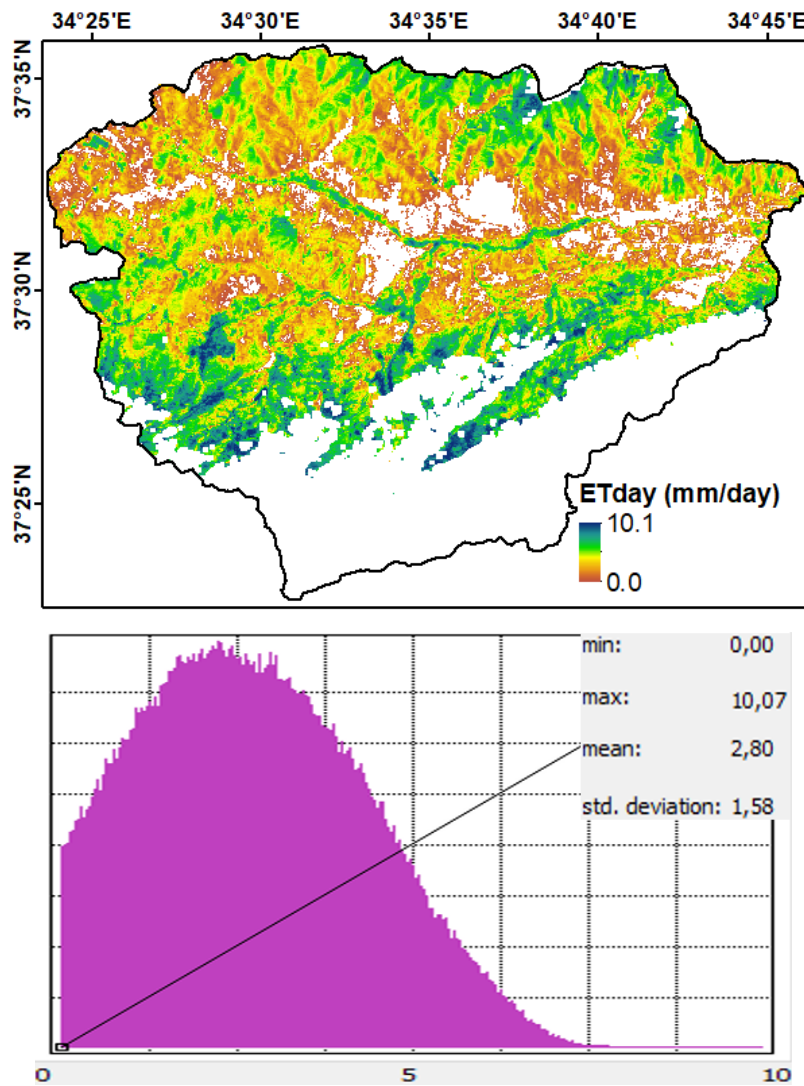
Figure 5.21. Daily ET map generated using the reference ET fraction, obtained from METRIC model
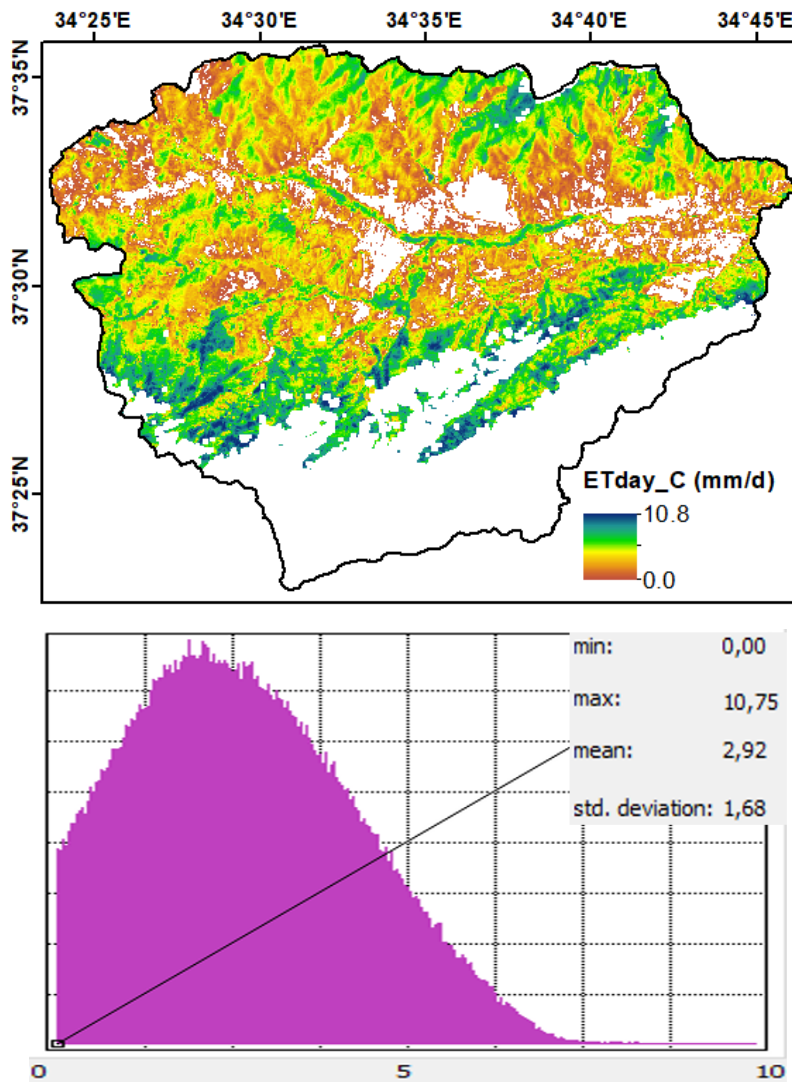
Figure 5.22. Daily ET map corrected for mountainous terrain, obtained from
METRIC model

5.4. R-METRIC

The R-METRIC model is explained in section 4.3. The analyses done using this model
for 27 June 2017 are illustrated in Figures 5.23-5.37. The RGB Landsat 8 image dated
27 June 2017 together with R-METRIC model hot-cold pixels and Eddy-Covariance
flux tower location is given in Figure 5.23. The study basin boundary is illustrated as
red polygon while the hot, cold pixels and Eddy-Covariance flux tower are red, blue

and teal points respectively. five hot and five cold pixels are automatically selected for the R-METRIC study.
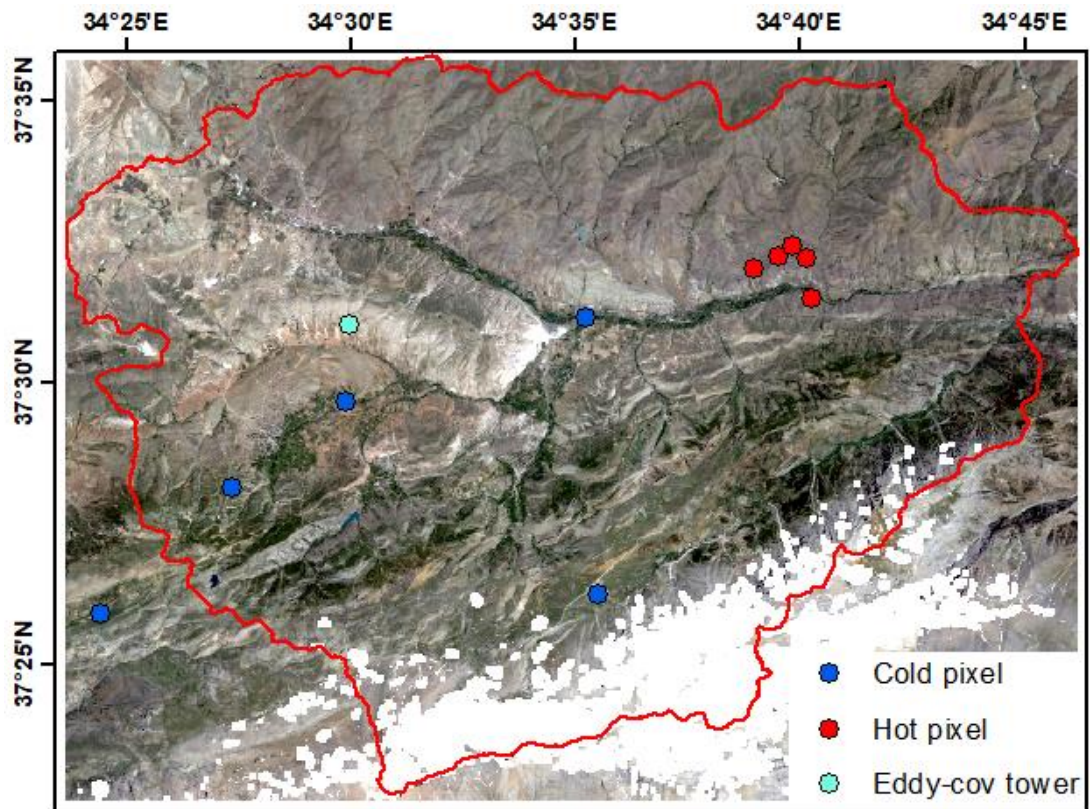
Figure 5.23. RGB Landsat 8 image with R-METRIC model hot-cold pixels and Eddy-Covariance flux tower (27 June 2017)

The R-METRIC albedo calculation is explained in section 4.2.1. At the Eddy station the albedo is calculated as 0.26 which is higher than the basin average, 0.16, due to being a dry region and probably consisting of gypsum area as explained previously (Figure 5.24).
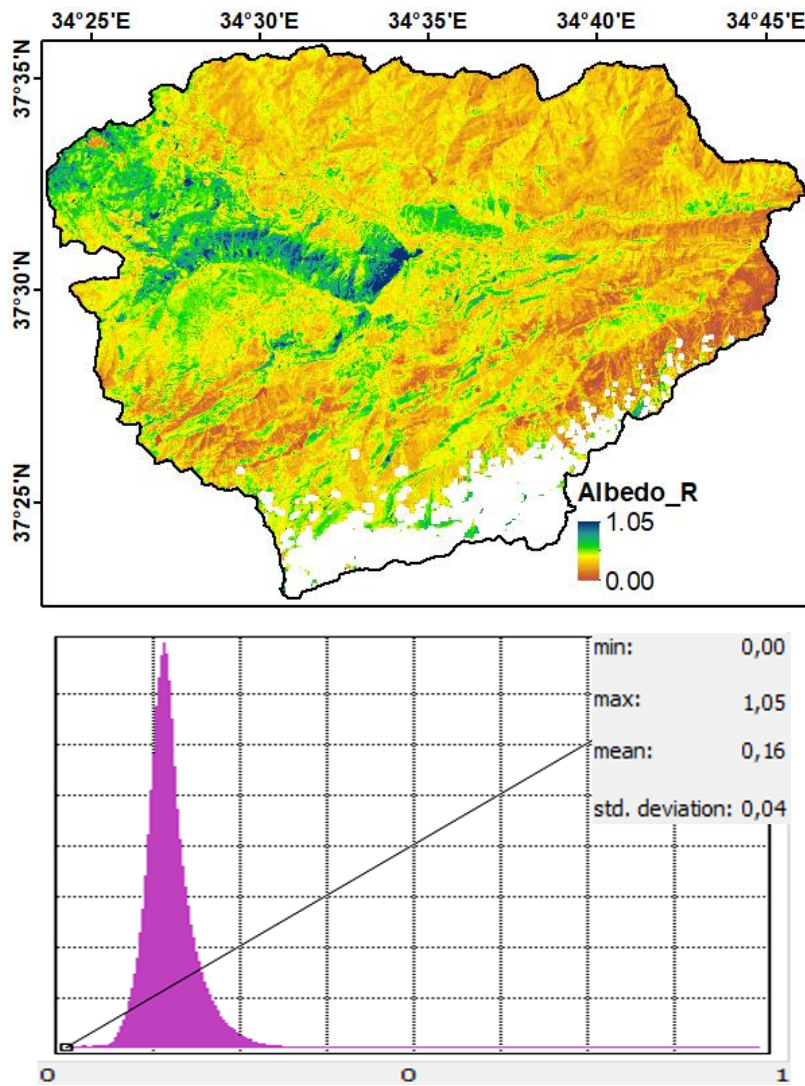
Figure 5.24. Albedo map generated from R-METRIC model

The Eddy station value for incoming short-wave radiation is calculated as 909 W/m^2 (Figure 5.25).
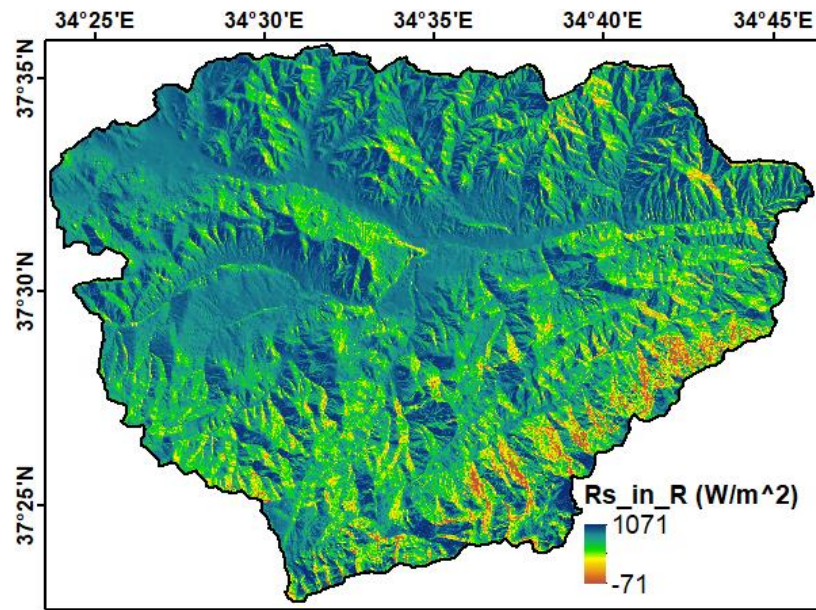
Figure 5.25. Incoming short-wave solar radiation map generated from R-METRIC model

The leaf area index value at Eddy tower is obtained as 0.20 which is still quite lower than a vegetative pixel (Figure 5.26). The vegetative areas can be observed in blue and green.
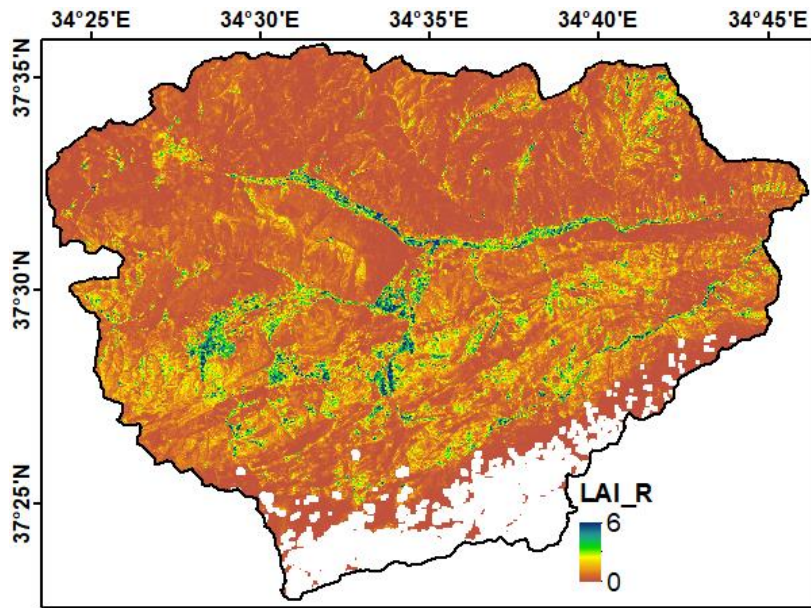
Figure 5.26. Leaf area index (LAI) map generated from R-METRIC model

The surface temperature at Eddy tower is 318 K which is the same value for both models (Figure 5.27).
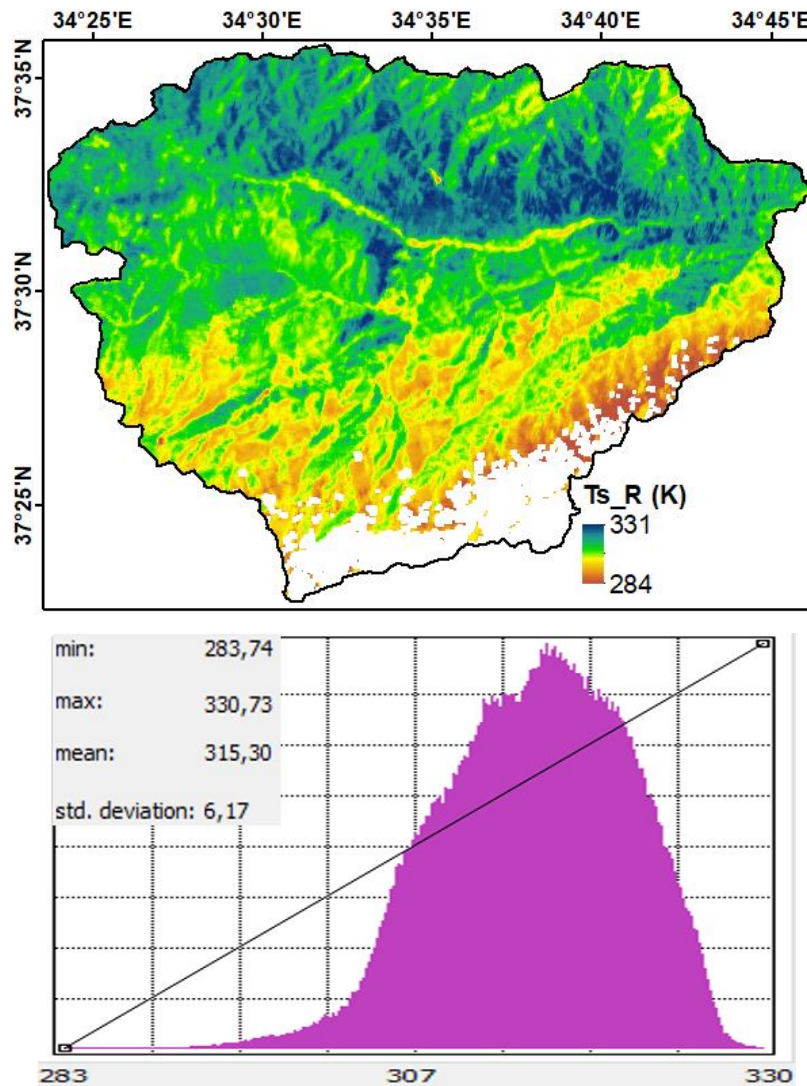
Figure 5.27. Surface Temperature map generated from R-METRIC model

The R-METRIC outgoing long-wave radiation at Eddy station is 534 W/m^2 (Figure 5.28). The incoming long-wave radiation at Eddy station is calculated as 435 W/m^2 (Figure 5.29). Those values are higher than the ones calculated by the METRIC model.
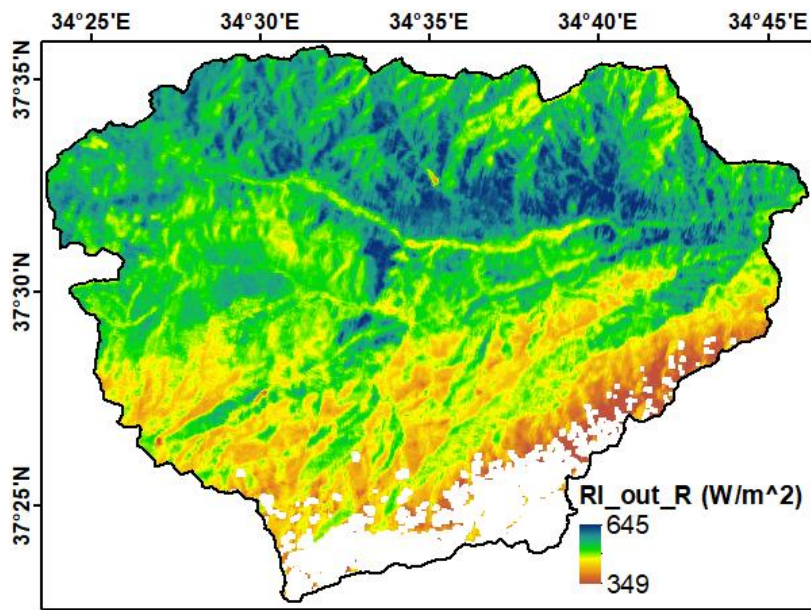
Figure 5.28. Outgoing long-wave solar radiation map generated from R-METRIC model
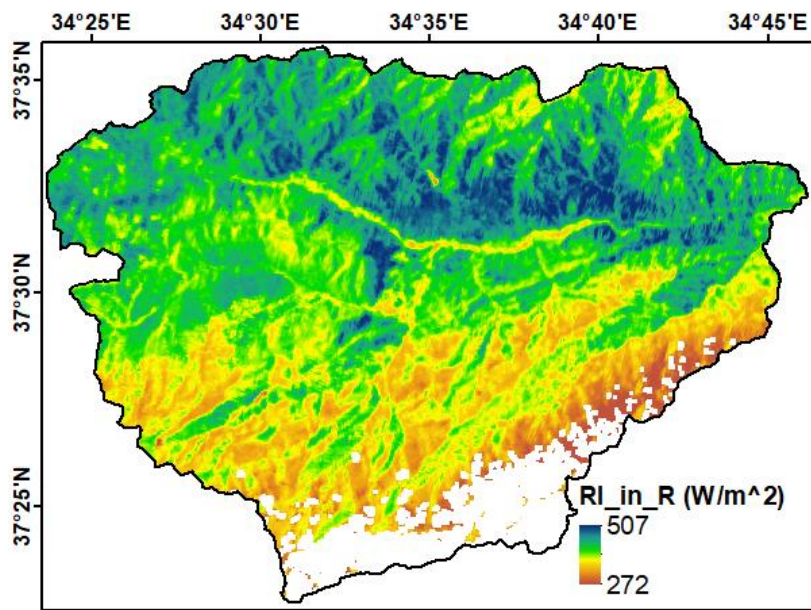
Figure 5.29. Incoming long-wave solar radiation map generated from R-METRIC model

The R_n at Eddy tower is obtained as 534 W/m^2 which is low due to high albedo of the region around the Eddy tower (Figure 5.30).
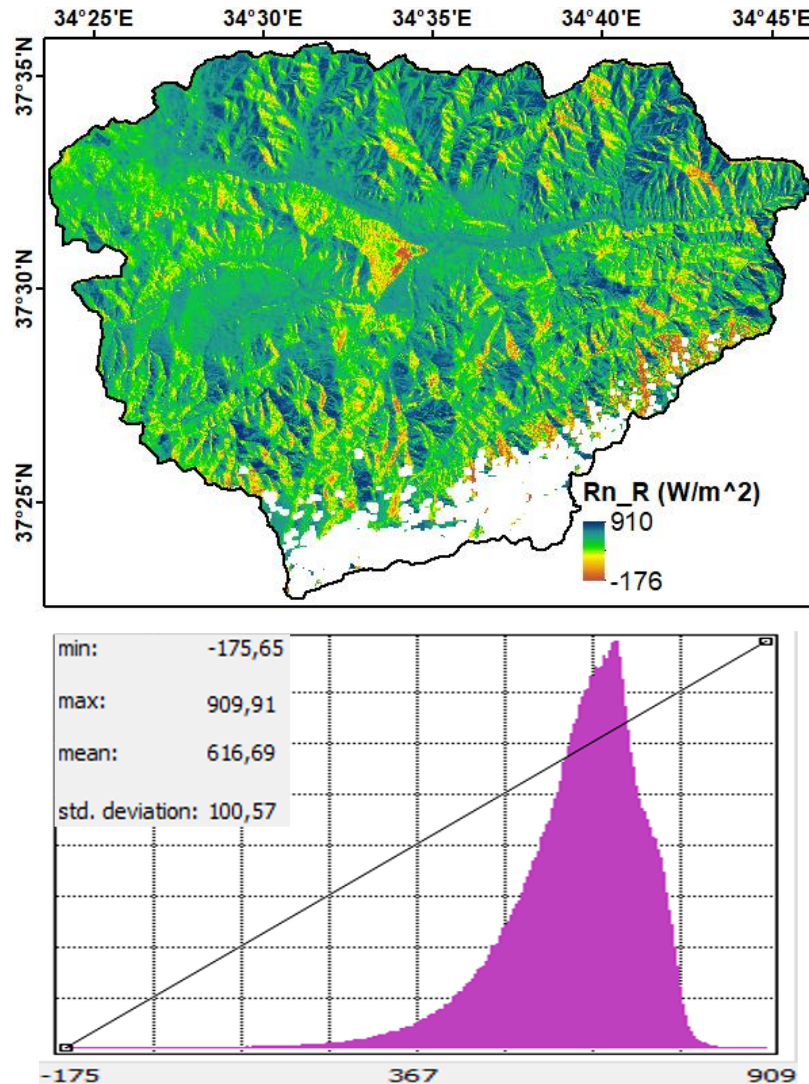
Figure 5.30. R_n map generated from R-METRIC model

The R-METRIC model soil heat flux value is calculated as 126 W/m^2 at Eddy tower which is more than the value calculated by METRIC model due to high surface temperature (Figure 5.31).
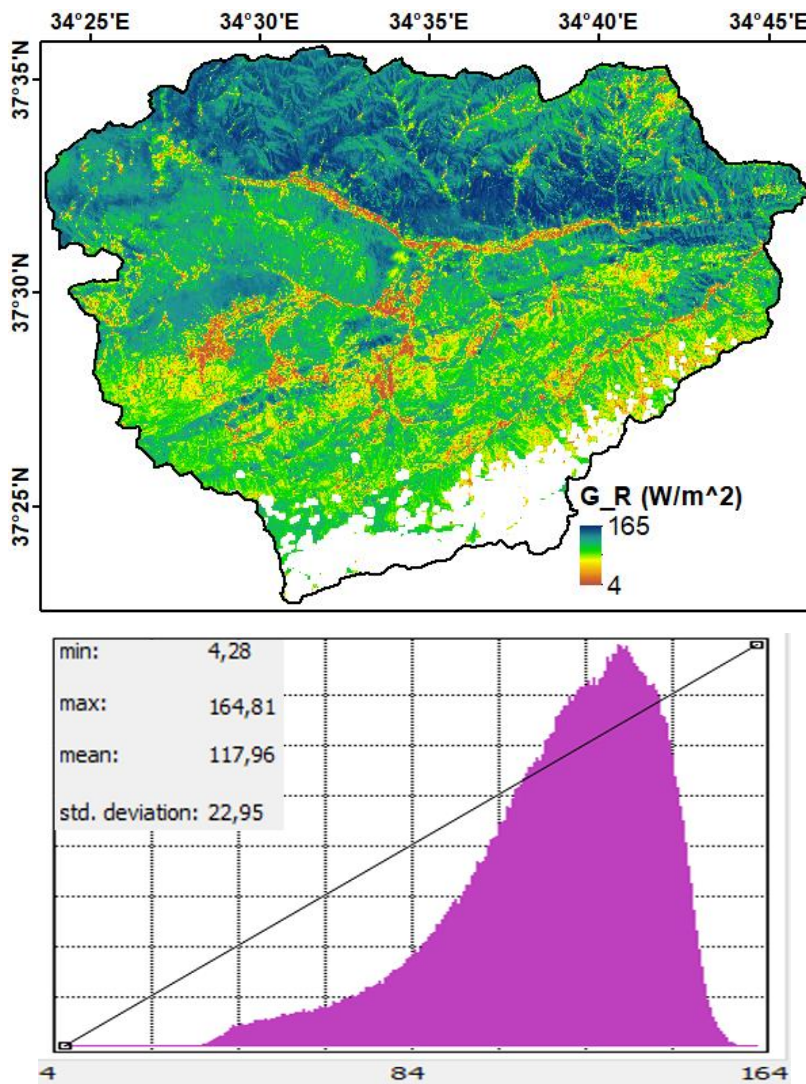
Figure 5.31. Soil heat flux (G) map generated from R-METRIC model

The surface roughness length (z_{om}) in R-METRIC is calculated depending on LAI (Equation [4.63]) which is explained in section 4.3.2. The z_{om} values calculated with CORINE Land Cover Class are much higher than the R-METRIC model z_{om} values (Figure 5.32).
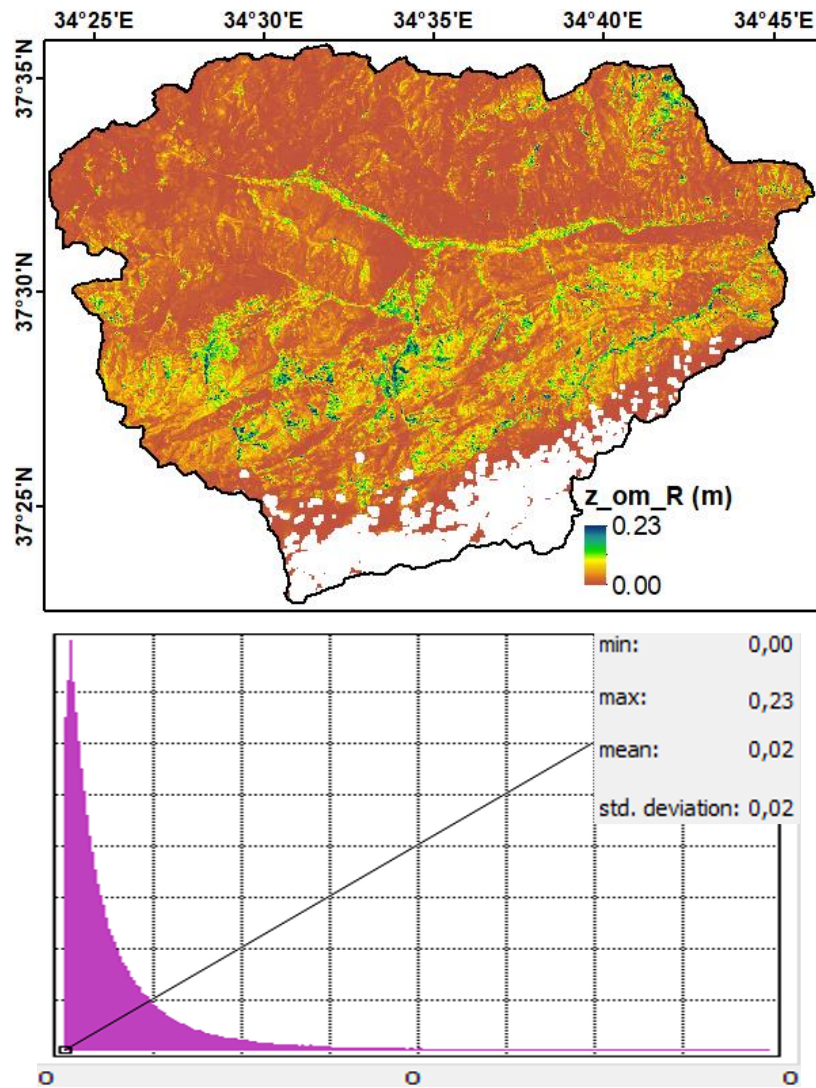
Figure 5.32. Surface roughness length map generated from R-METRIC model

The near-surface temperature difference at Eddy tower is calculated as 2.38 K (Figure 5.33). The range between maximum and minimum dT is significantly higher for the R-METRIC model.
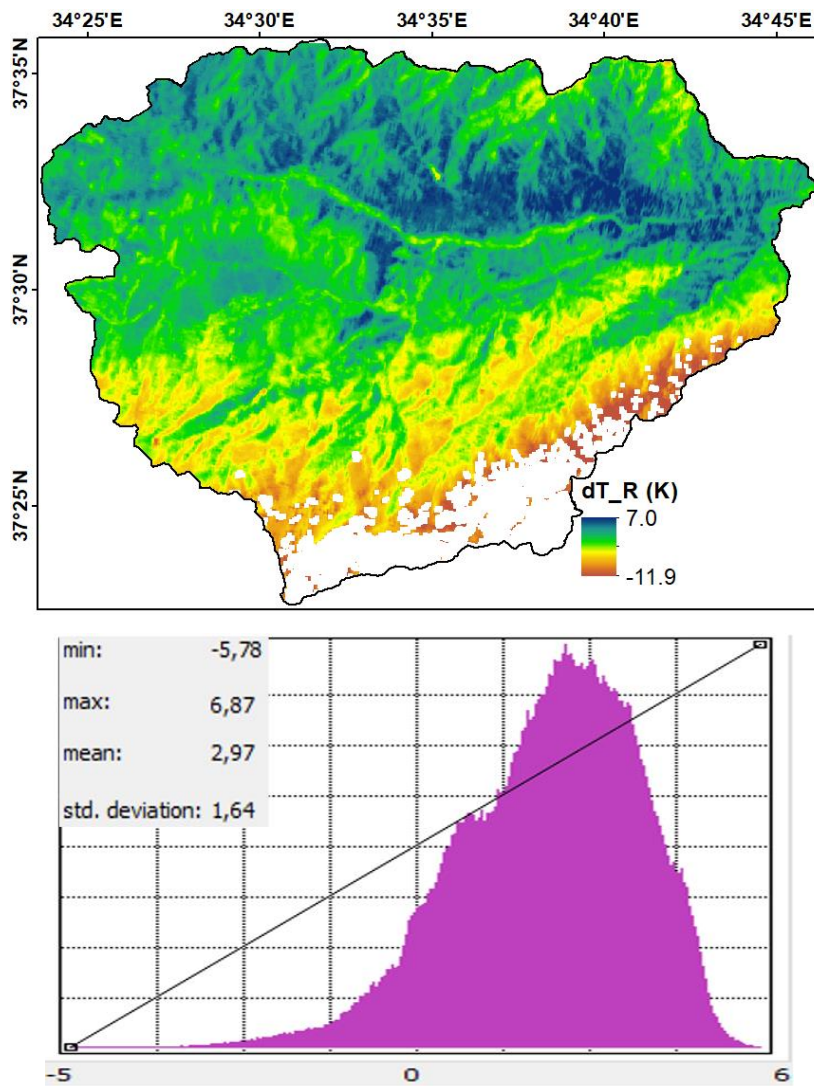
Figure 5.33. Near surface temperature difference (dT) map generated from R-METRIC model

The automated anchor pixel selection considers values of albedo, LAI, NDVI, surface roughness length (z_{om}) and surface temperature (T_s) (Table 5.6).

Table 5.6. Automated anchor pixel selection parameters (27.06.2017)

type	z_{om} (m)	T_s (K)	LAI	NDVI	albedo
hot	0.001	330.47	0.05	0.18	0.13
hot	0.005	330.38	0.16	0.27	0.14
hot	0.002	330.31	0.08	0.20	0.14
hot	0.001	329.84	0.04	0.17	0.14
hot	0.002	329.67	0.08	0.21	0.14
cold	0.076	306.54	4.84	0.74	0.20
cold	0.079	306.60	5.56	0.78	0.20
cold	0.077	309.27	4.90	0.75	0.19
cold	0.078	309.87	4.77	0.75	0.20
cold	0.072	310.01	4.22	0.73	0.19

Comparing Table 5.5 and Table 5.6 the most difference in the parameters of METRIC and R-METRIC methods is obtained for z_{om}.

The sensible heat flux of R-METRIC model at Eddy tower pixel is calculated as 99 W/m^2 (Figure 5.34). The sensible heat flux values of the R-METRIC model are significantly lower than the values of METRIC model due to the use of ET$_r$ in the sensible heat flux calibration.
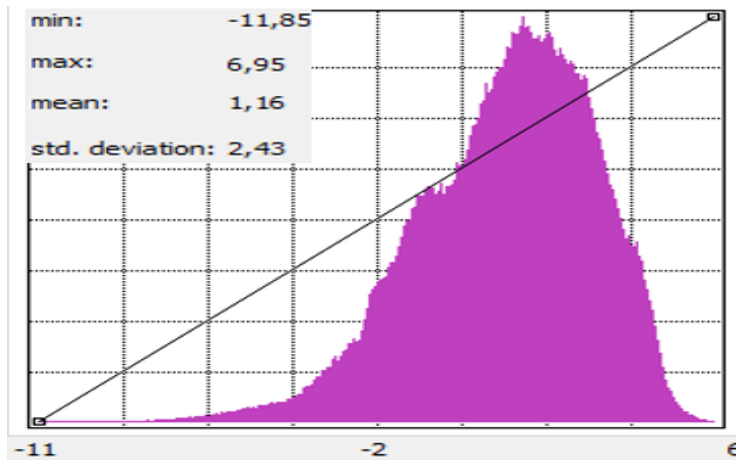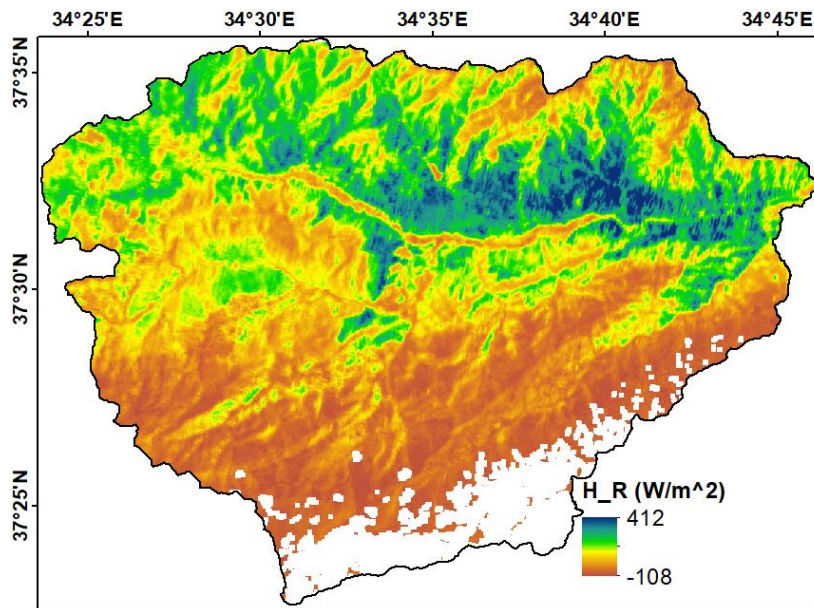
Figure 5.34. Sensible heat flux map generated from R-METRIC model

At Eddy tower location the latent heat flux is calculated as 316 W/m² at satellite passing time (Figure 5.35).
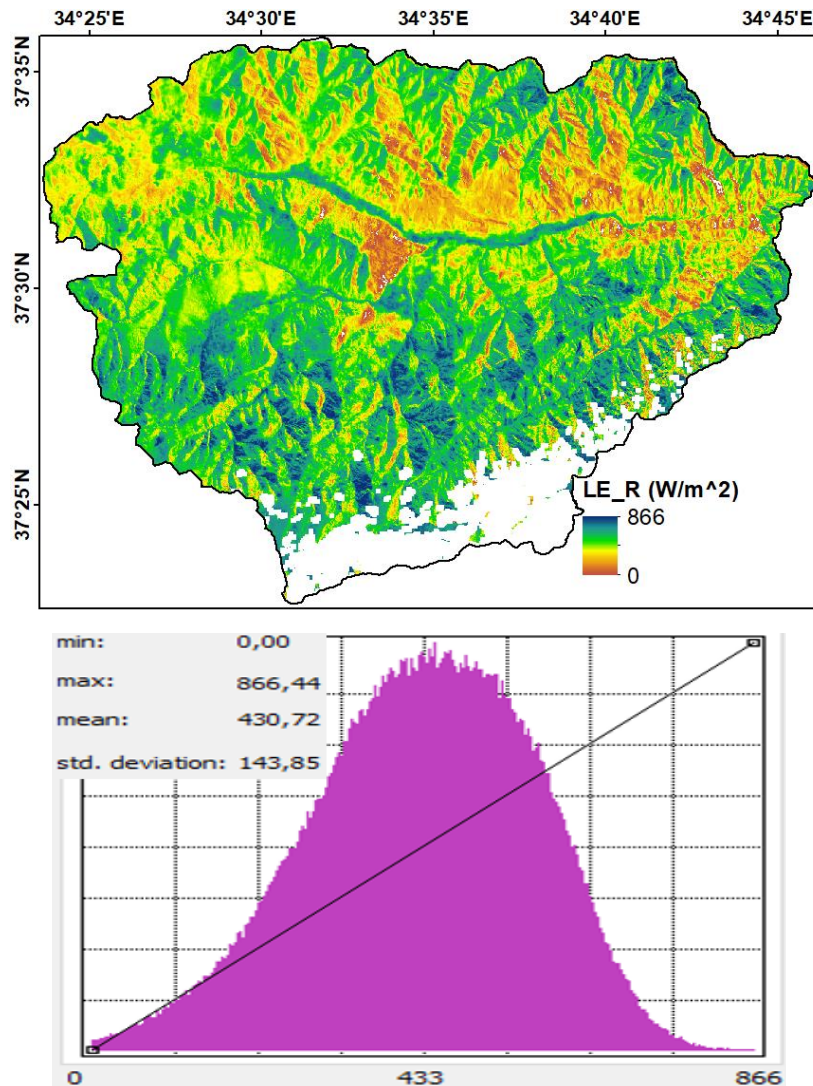
Figure 5.35. Latent heat flux map generated as residual of surface energy balance of R-METRIC model

In R-METRIC model the daily ET is also calculated using instantaneous ET with solar radiation correction coefficient (C_{rad}) and reference ET fraction (ET_rF). First the reference ET fraction is multiplied to generate R-METRIC model daily ET map (Figure 5.36). Then the same solar radiation correction coefficient is introduced to observe the effect of mountain correction (Figure 5.37). Since the C_{rad} depends on the Julian day, topographic parameters and meteorological station data which are the same

for both models, the same C_{rad} maps for 27 June 2017 are implemented for both models. The histogram of the final product is given in Figure 5.36 to understand the trend of the daily ET map. The daily ET values at Eddy tower are 5.18 mm/day and 5.19 mm/day after mountain correction. The daily basin average actual ET is increased after the mountain correction.
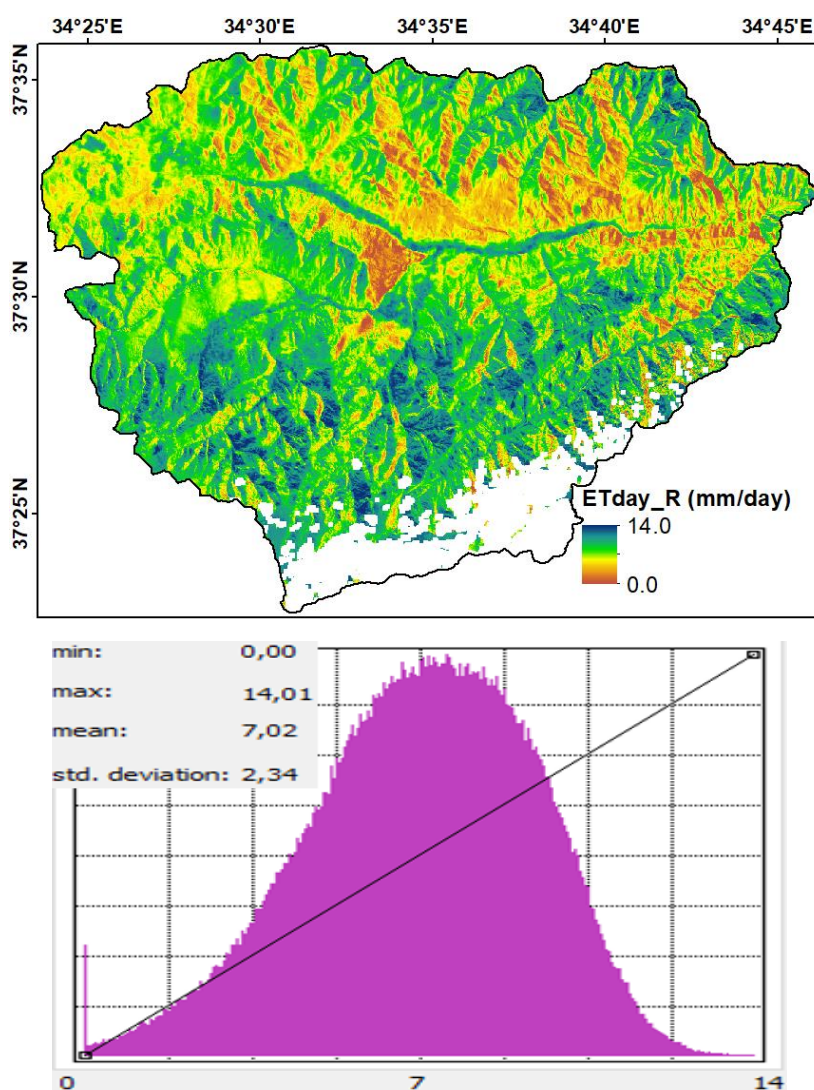
Figure 5.36. Daily ET map generated using the reference ET fraction, R-METRIC model
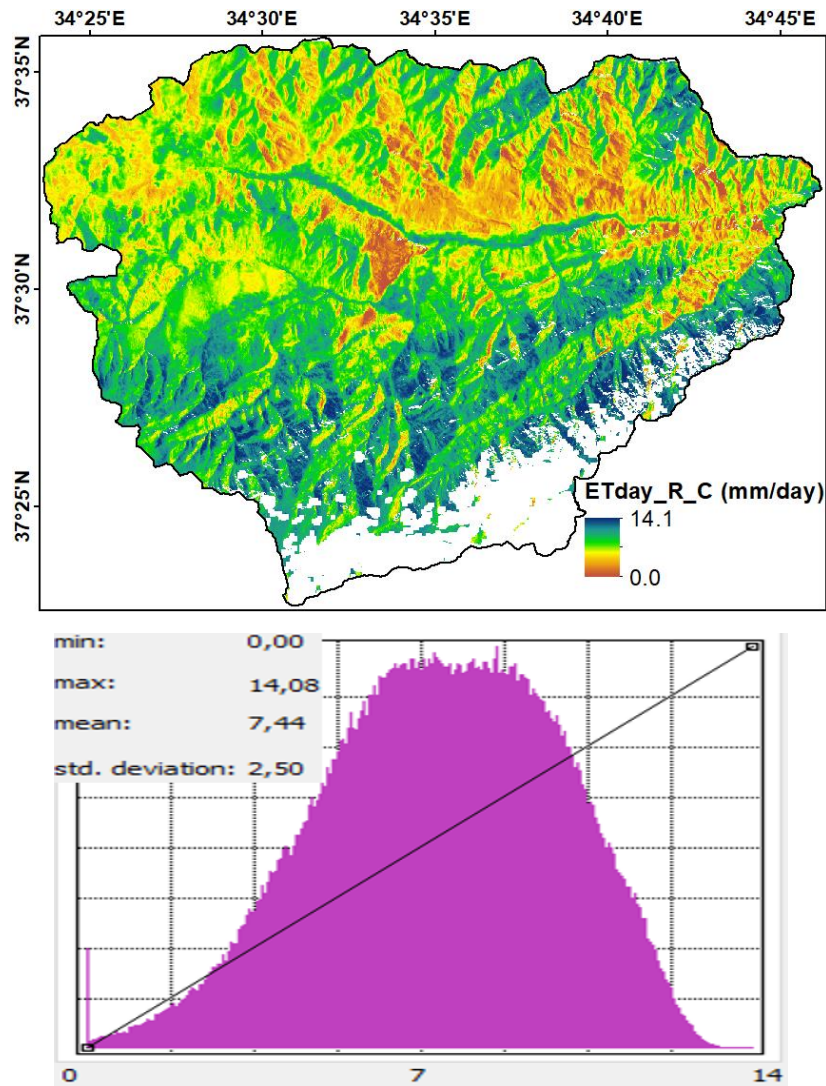
Figure 5.37. Daily ET map corrected for mountainous terrain, R-METRIC model

5.5. Eddy Covariance Surface Energy Balance Study

The Eddy-Covariance tower flux data is examined and some complication disturbing the integrity of the data have been found. As an example, the date June 4, 2017 is examined in detail. It is known from the quality study that a very dense cloud event happened on 4 June 2017 (Figure 5.38). The surface energy balance implies that the red and blue lines should be close to each other. During a dense cloud event this fails.

The R_n converges to zero as expected but the latent heat flux sensor stopped working for some time.
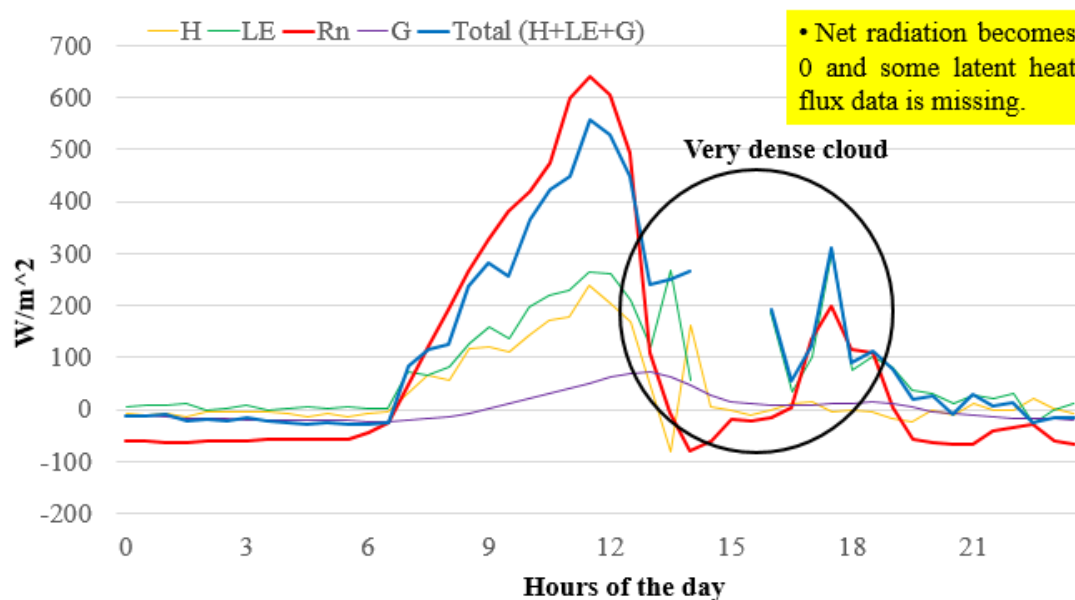
Figure 5.38. Eddy-Covariance tower flux data dated June 4, 2017

As a second event approximately one year later, the surface energy balance is quite good until a rainfall event occurs (Figure 5.39). Then the latent heat flux values become inaccurate. So, it is needed to eliminate such faulty data before studying the enclosure of the surface energy balance.
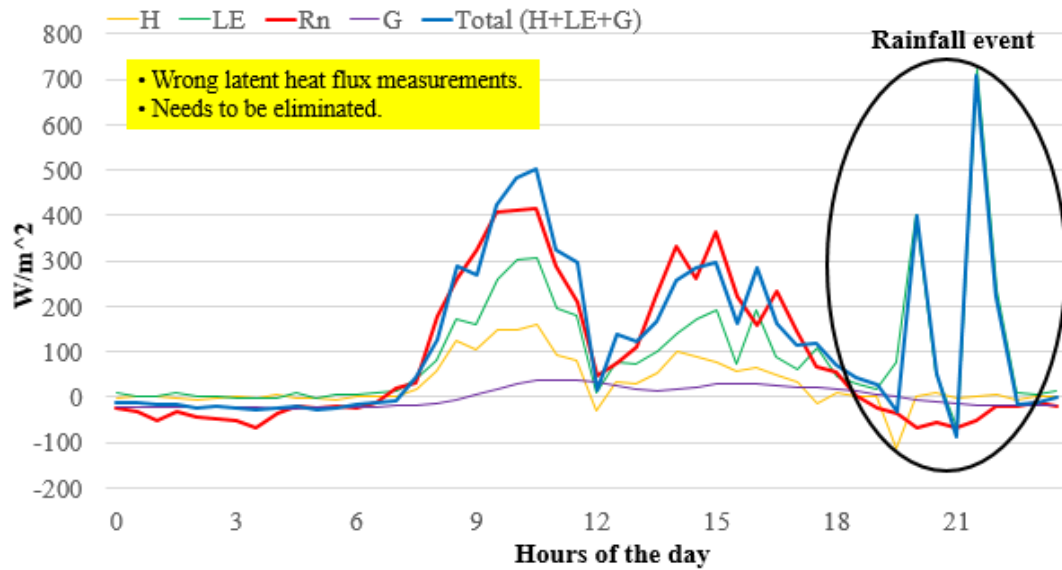
Figure 5.39. Eddy-Covariance tower flux data dated May 10, 2018

All the flux data gathered from the Eddy-Covariance flux tower is used to constitute a diurnal cycle. In Figure 5.40 the data is used without any correction while in Figure 5.41 the data have been corrected for extreme events. The correction uses the Gaussian distribution to get rid of extreme values. Approximately 75 to 80% of the data are used after the correction. However, no significant change except the smoothening of the lines is observed. Looking at the diurnal cycle the gap between the red and blue line, in other words the error increases towards noon. From the analysis performed on energy budget the maximum error is obtained for the noontime as 23%. One reason for this is that the Eddy-Covariance flux tower is not seasonally calibrated. However, this error margin is still within acceptable limits even when no calibration is performed (Twine, et al., 2000). As a result, it is decided that the error of the surface energy balance is amplified due to the heterogeneous topography of the measurement site where Eddy-Covariance flux tower is situated.
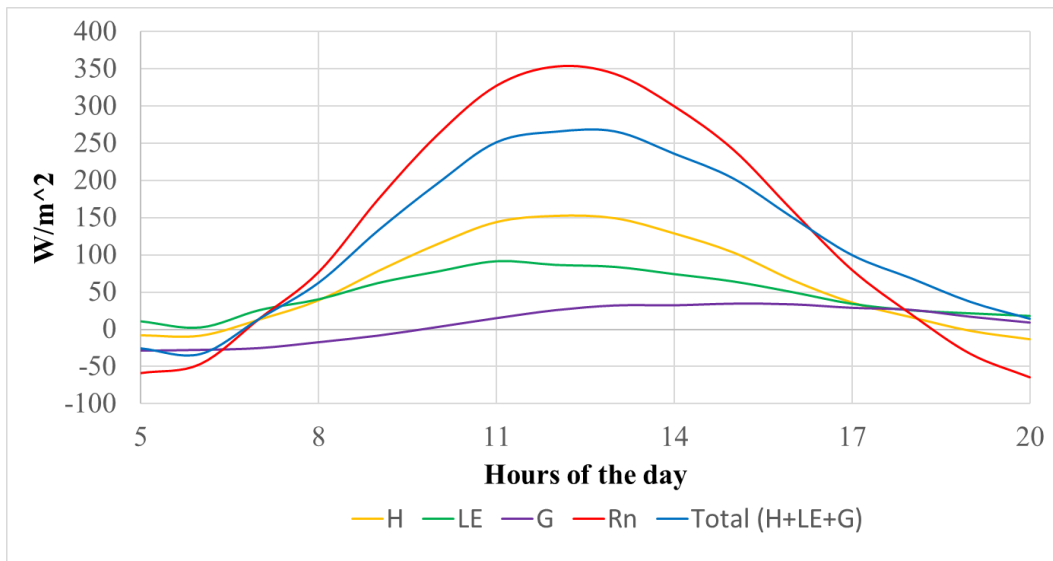
Figure 5.40. Diurnal cycle of Eddy-Covariance flux data before correction between
27.03.17 – 11.03.19
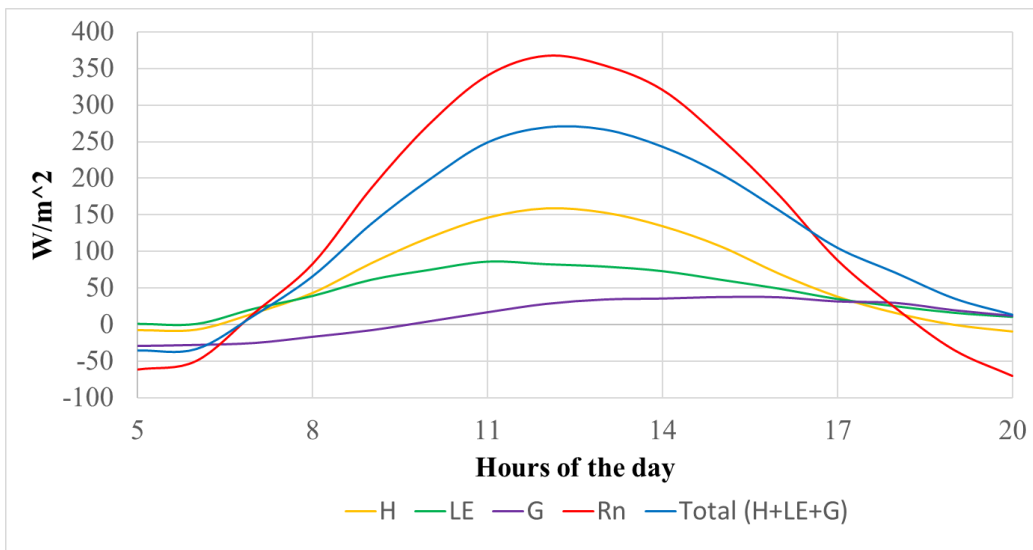
Figure 5.41. Diurnal cycle of Eddy-Covariance flux data after correction between
27.03.17 – 11.03.19

CHAPTER 6

RESULTS AND DISCUSSIONS

6.1. Eddy-Covariance Flux Tower Results

The Eddy-Covariance tower installed at 1478 meters in the study basin measured the sensible heat flux (H), latent heat flux (LE), soil heat flux (G) and net radiation (R_n) since April 2017. The Eddy-Covariance flux tower calculates latent heat flux via sensors by gathering information from the environment using a fetch distance. In flat regions, the estimated fetch distance for 2 meters sensor height is around 200 meters. However, in this study the region is mountainous resulting at a non-flat environment around the Eddy-Covariance flux tower which limits using a large area with 200 meters fetch distance.

Looking at the closure of Eddy-Covariance tower in this study the maximum error is found as 23% near noontime. The peak R_n value is 350 W/m^2 and the error value at this time is about 80 W/m^2. Hereby we see that the error rate is 23%. This is the maximum error and the average error would be smaller. Therefore, although the land cover around the Eddy-Covariance flux tower is susceptible to error, the study values remain within the range stated in the literature (Widmoser and Wohlfahrt, 2018). Since the Eddy-Covariance system measures fluxes from the turbines in the air (micro scale), the error goes up with increasing time scales.

The Eddy-Covariance flux tower gathers three different latent heat flux values that can be utilized in daily ET calculations. The first two latent heat fluxes are gathered directly with the use of EC150 and KH20 sensors. The third latent heat flux value is calculated via the surface energy balance parameters leaving latent heat flux as a residue of surface energy balance similar to the METRIC model. Looking at Figure 6.1 and Figure 6.2, the KH20 sensor results are in generally higher in value than the EC150 sensor. The KH20 sensor has failed in April 2018. Daily ET values obtained

from LE measured by EC150 and KH20 sensors are not complete for all the 43 Landsat 8 satellite images utilized in METRIC model calculations. However, considering the daily ET generated from Eddy-Covariance flux tower surface energy balance there is a daily ET value for each Landsat 8 satellite image. The surface energy balance daily ET values are perceptibly higher than obtained from EC150 and KH20 sensors daily ET values. Not being perfectly correlated, a seasonal trend can be visualized for the Eddy-Covariance flux tower daily ET values.
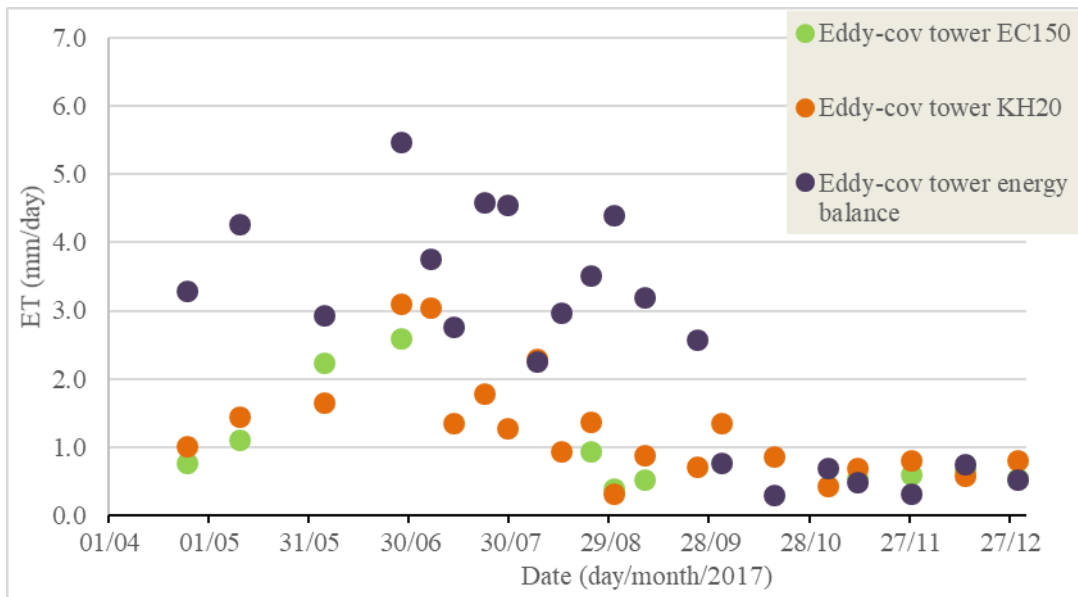
Figure 6.1. The comparison of Eddy-Covariance flux tower daily ET values (2017)
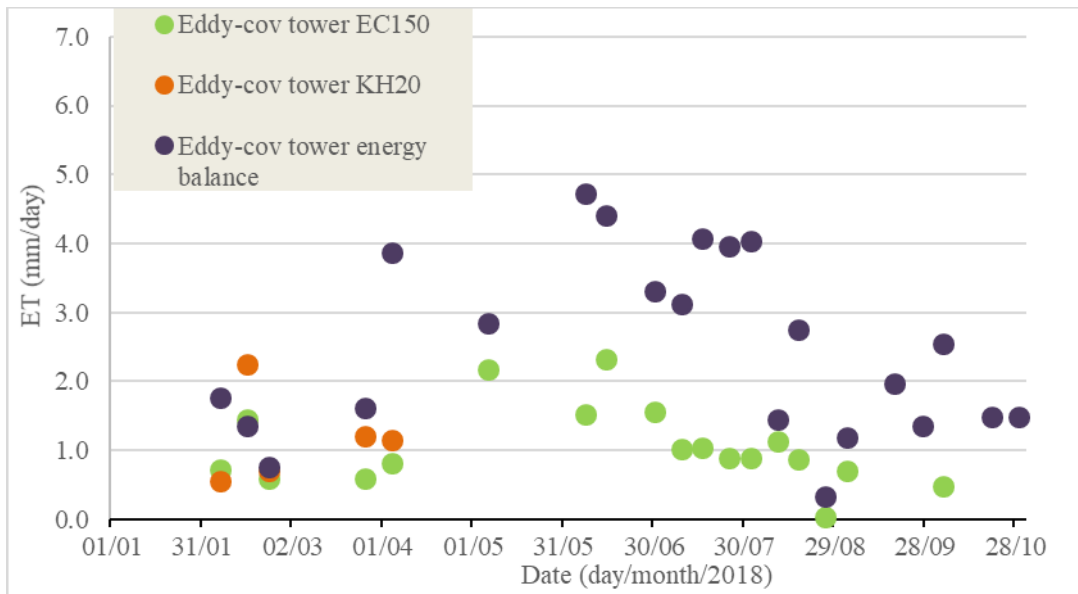
Figure 6.2. The comparison of Eddy-Covariance flux tower daily ET values (2018)

93

6.2. METRIC and R-METRIC Methods Results

The estimated daily actual ET results of the METRIC and R-METRIC models were compared with the measured Eddy-Covariance surface energy balance ET using three performance measure criteria (i.e., Root Mean Square Error (RMSE), coefficient of determination (R^2), and the correlation coefficient (C_r) (Khadr, 2016)). While model results are measured values (ET_{meas}), the Eddy-Covariance data are observed values (ET_{obs}).

The coefficient of determination, R^2 is calculated using Equation [6.1]. It indicates the relative fit between the data.

$$R^2 = 1 - \frac{\sum(ET_{obs} - ET_{meas})^2}{\sum(ET_{obs})^2} \qquad [6.1]$$

The correlation coefficient (C_r) is a measure of how well the trends model results follow the trends in the Eddy-Covariance values. The correlation coefficient is calculated using Equation

[6.2], where n is the number of observations:

$$C_r = \frac{(\sum ET_{obs} * ET_{meas}) - \frac{(\sum ET_{obs})(\sum ET_{meas})}{n}}{\sqrt{[(\sum ET_{obs}^2 - \frac{\sum(ET_{obs})^2}{n})(\sum ET_{meas}^2 - \frac{\sum(ET_{meas})^2}{n})]}} \qquad [6.2]$$

The RMSE is the square root of the variance of the residuals. It indicates the absolute fit of the model to the data. It indicates how close the model results are to the observed values from the Eddy-Covariance flux tower. RMSE is calculated as in Equation [6.3].

$$RMSE = \sqrt{\frac{\sum(ET_{obs} - ET_{meas})^2}{n}} \qquad [6.3]$$

Due to an existing fetch distance in the latent heat flux sensor, investigating only one pixel may arise some error. Trying to eliminate the errors that can occur by taking 1 pixel into account at Eddy-Covariance flux tower location, the METRIC and R-METRIC results are analyzed using a 100 meters fetch distance. The average of all pixels lying in the fetch is calculated with equal weights. Investigating Figure 6.3 and Figure 6.4, it can be seen that the fetch study has increased the daily ET values for both METRIC and R-METRIC models which is a result of the environment being so different than the Eddy-Covariance flux tower pixel. The seasonal trend is present for the METRIC and R-METRIC model results as well. However, the seasonal trend is especially improved with the fetch study in year 2018. For dates 7 August 2017, 7 September 2017 and 4 April 2018 the Eddy-Covariance flux tower pixel was masked due to illogical parameters of METRIC model observed at this pixel. Therefore, no values for "METRIC Eddy point" series for specified dates are presented in Figure 6.3 and Figure 6.4.

METRIC model and R-METRIC model results are compared with the Penman-Monteith reference ET values and the results are shown in Figure 6.5 and Figure 6.6. The latent heat flux estimating sensors are sensible and those sensors can fail in bad weather conditions as explained in Section 5.5. Due to the reliability and having a full set of data for the 43 days used in this study, the Eddy-Covariance surface energy balance results are used rather than KH20 and EC150 sensor data. The Eddy-Covariance tower energy balance results are close to the Penman-Monteith reference ET values which are frequently used as daily ET reference. The Penman-Monteith reference ET is almost always greater than the estimated and calculated actual ET values. The reason for high ET results is that the Penman-Monteith reference ET assumes unlimited water and with this assumption water is not a limiting factor for the calculations. The most catching feature of these figures is the similarity between the Eddy-Covariance tower energy balance and R-METRIC model daily ET values. Both results have a well-established seasonal curve with Eddy-Covariance tower results

being generally higher than the R-METRIC model results. The difference in value between those results can be seen as quite consistent.

Figure 6.3. The comparison between METRIC and R-METRIC model results at Eddy-Covariance tower location and the 100 meters fetch area averages (2017)

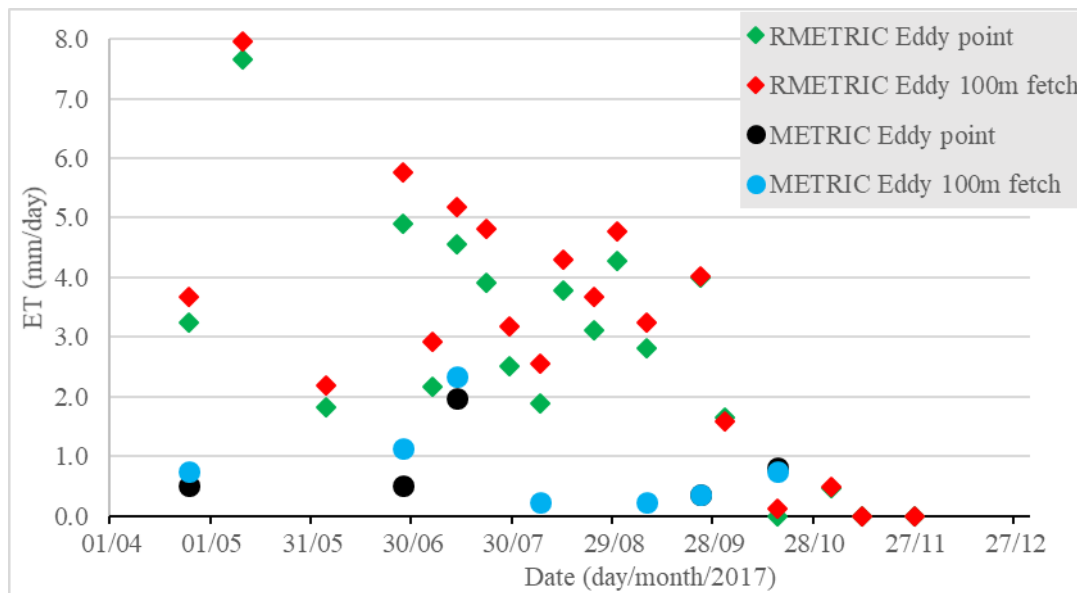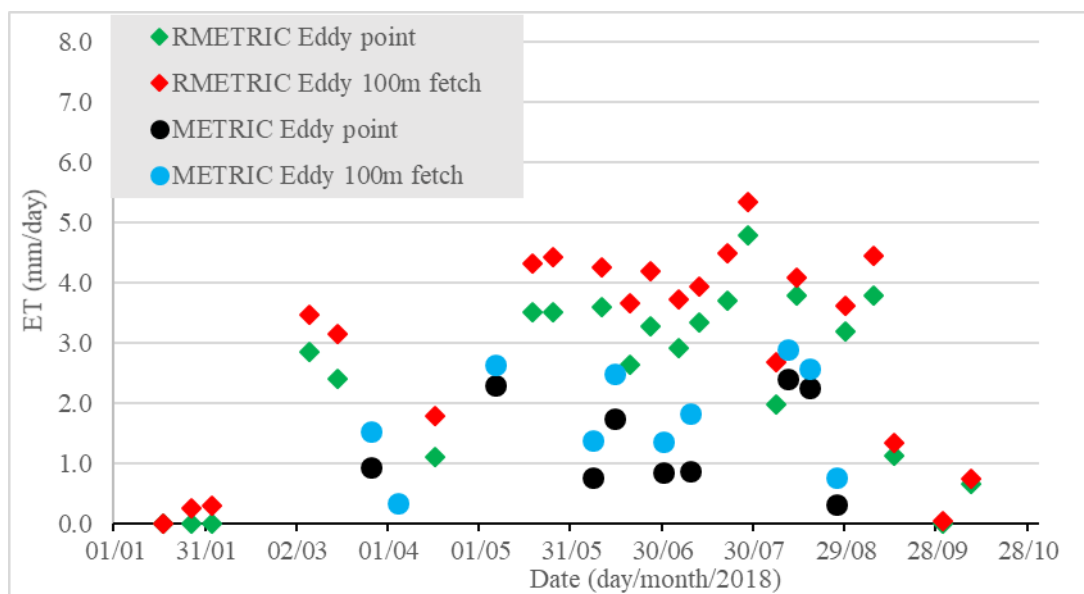Figure 6.4. The comparison between METRIC and R-METRIC models results at Eddy-Covariance tower location and the 100 meters fetch area averages (2018)
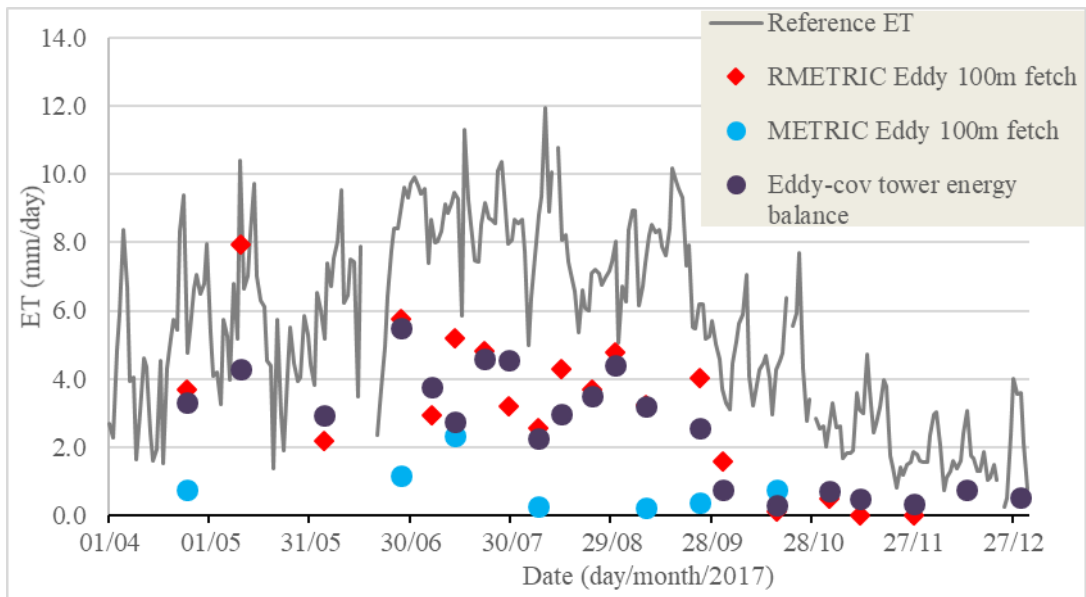
Figure 6.5. The Penman-Monteith reference ET, Eddy-Covariance flux tower, METRIC and R-METRIC results daily ET comparison (2017)
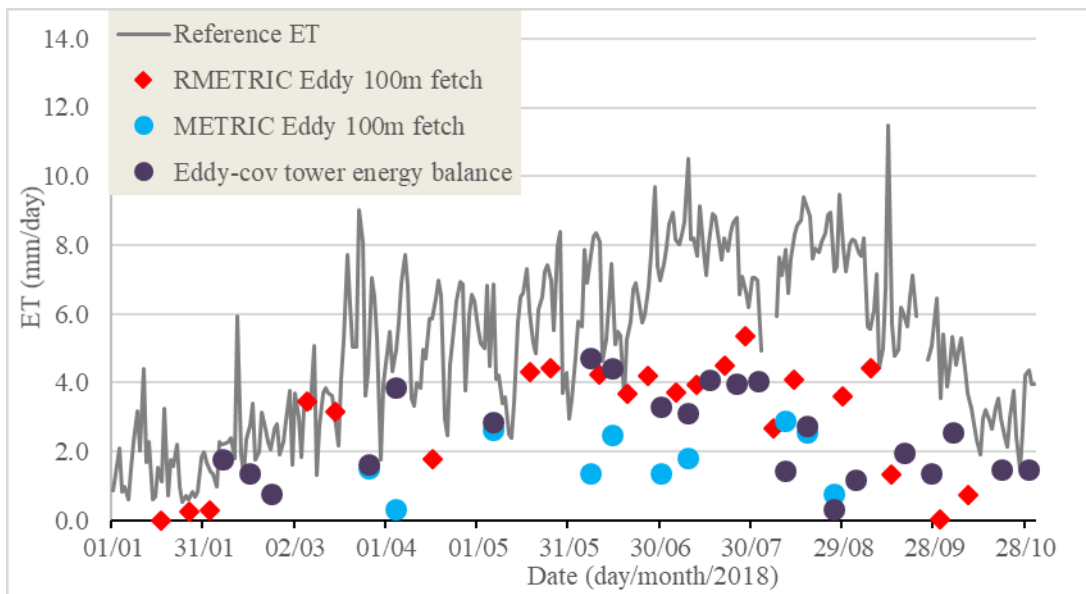
Figure 6.6. The Penman-Monteith reference ET, Eddy-Covariance flux tower, METRIC and R-METRIC results daily ET comparison (2018)

A fetch of 100 meters is utilized for METRIC and R-METRIC results to better simulate the observed data obtained from the Eddy-Covariance tower since the sensible heat flux data is measured with a fetch distance. In Table 6.1, the observed Eddy-Covariance data are compared with METRIC at Eddy-Covariance tower pixel (METRIC) and 100 meters fetched (METRIC-fetch) results for the 17 days estimated. Also, R-METRIC at Eddy-Covariance tower pixel (RMET) and 100 meters fetched (R-MET-fetch) results are compared with the observed Eddy-Covariance data for the same 17 days, in addition to all 43 days processes with the R-METRIC model (RMET43 and RMET43-fetch). Finally, the R-METRIC model results for the months from April to September are compared with the observed Eddy-Covariance data (RMET6month and RMET6month-fetch).

Table 6.1. RMSE, R^2 and C_r parameters between the estimated daily ET results of the METRIC and R-METRIC models and observed Eddy-Covariance tower daily ET

	R^2	C_r	RMSE (mm/day)
METRIC	0.3812	-0.07	2.477
METRIC-fetch	0.5340	0.05	2.149
RMET	0.8389	0.55	1.264
RMET-fetch	0.7853	0.60	1.459
RMET43	0.7909	0.67	1.335
RMET43-fetch	0.7650	0.71	1.415
RMET6month	0.8188	0.25	1.468
RMET6month-fetch	0.7911	0.32	1.577

Looking at Table 6.1, the fetch application has a positive effect on the results. Comparing results of RMET43 and RMET6month, the R^2 is better without winter months, although the C_r and RMSE are lower with the inclusion of winter months. Also, it should be noted that the R-METRIC estimates from November to February around the Eddy-Covariance flux tower are 0. Finally, the R-METRIC model results

are better than the METRIC model results for all three performance measurement criteria considering the correlation with the Eddy-Covariance tower flux data.

The scatter plot between RMET43 and Eddy-Covariance tower energy balance is given in Figure 6.7. In addition, the scatter plot between RMET43-fetch and Eddy-Covariance tower energy balance is given in Figure 6.8. The fetch study significantly improved the R-METRIC results for the range where Eddy-Covariance energy balance measurements are between 3 and 5 mm/day as it is shown in Figure 6.7 and Figure 6.8 in circle.

In Figure 6.9 and Figure 6.10 the basin averages of the METRIC and R-METRIC models are compared with the Penman-Monteith reference ET. Comparing basin averages to Eddy-Covariance tower location results, the basin averages are way smoother in terms of seasonal trends which can be expected due to a larger pool of data. Compared to the METRIC model, the R-METRIC model results are better at catching the seasonal trend together with the Eddy-Covariance flux tower comparison. In R-METRIC model more images could be used and this gives a better temporal analysis of ET variation.

The center part of the study basin was clipped to better visualize the daily ET results for different terrain types. In Figure 6.11(a), the blue area in the top is a water body. The white area in the center is a gypsum mine and finally the dark green parts are vegetation. In Figure 6.11(b), the clipped METRIC model daily ET map is given. The water body and vegetation are high ET regions as expected while the gypsum mine is masked out in the METRIC model application. In Figure 6.11(c), the clipped R-METRIC model daily ET map is shown. The water body and vegetation are blue which are high ET regions the same as the METRIC model. However, in the R-METRIC application the gypsum mine is red which means near zero ET.
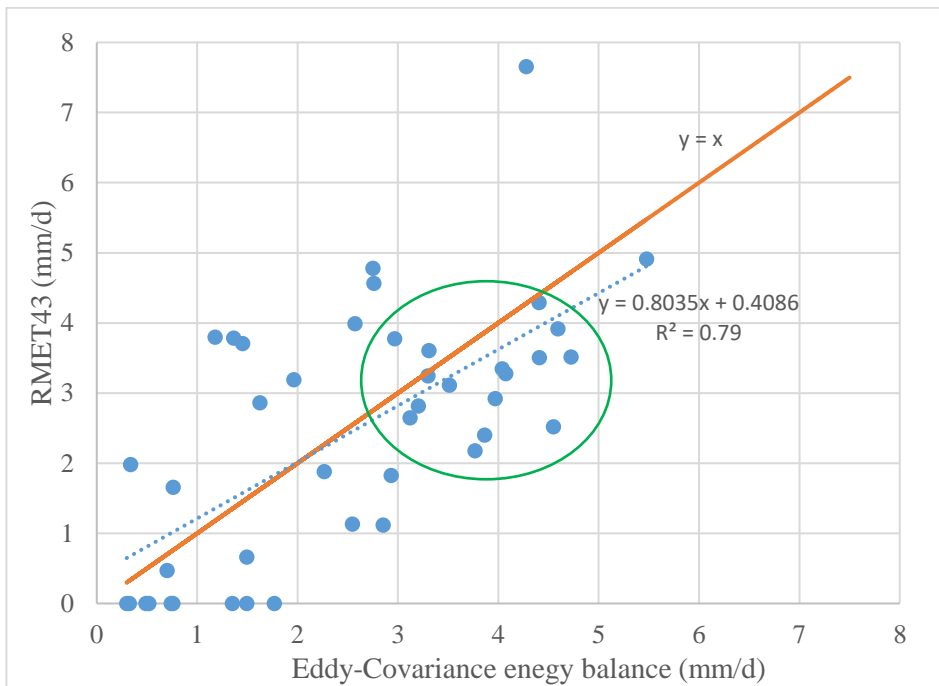
Figure 6.7. Scatter plot between RMET43 and Eddy-Covariance energy balance
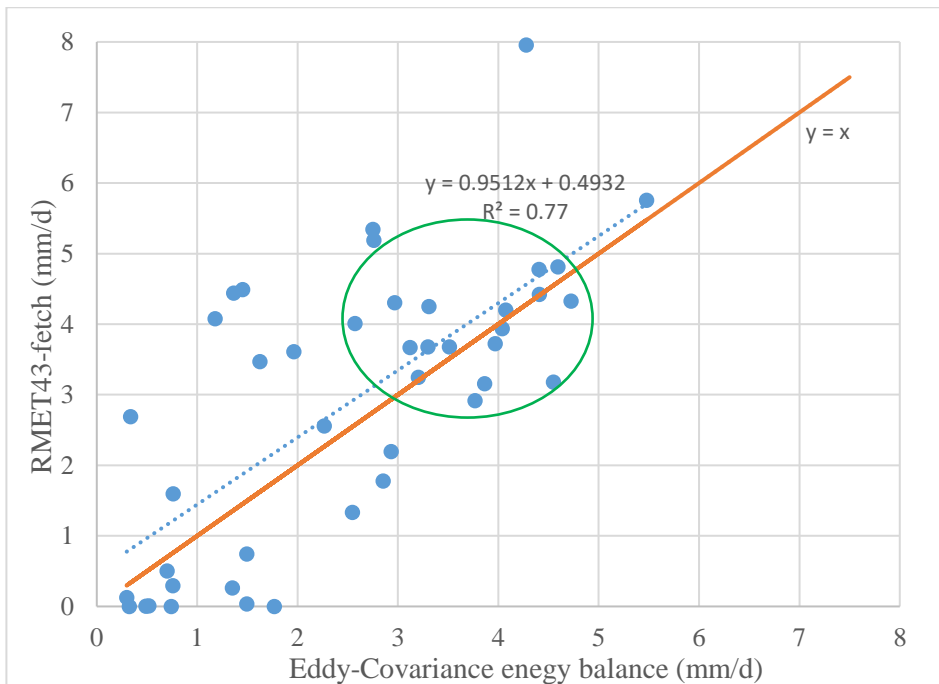
Figure 6.8. Scatter plot between RMET43-fetch and Eddy-Covariance energy
balance
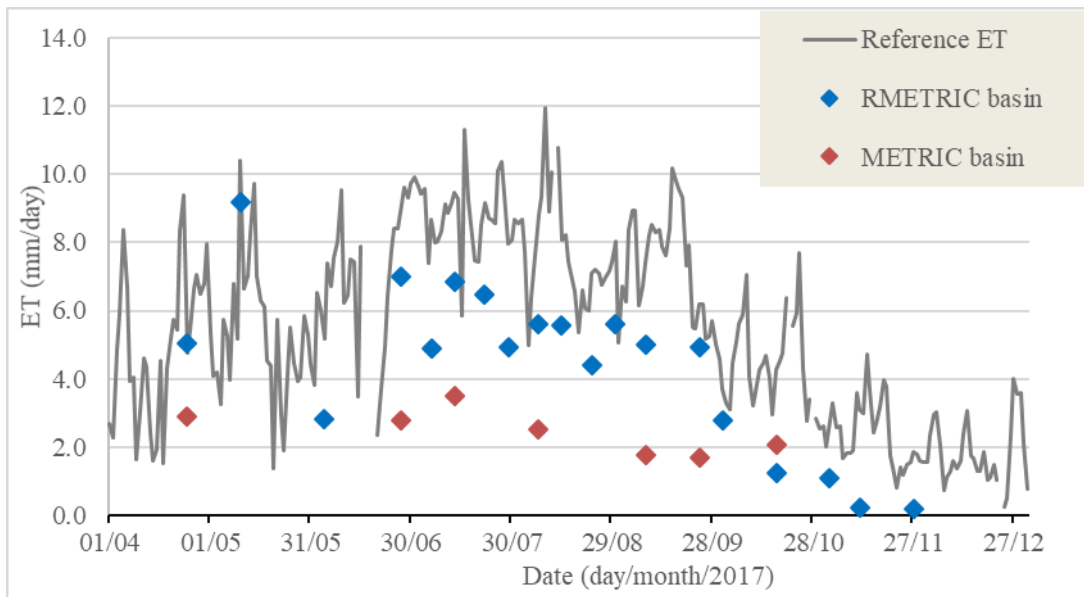
Figure 6.9. The Penman-Monteith reference ET, METRIC and R-METRIC basin averages daily ET comparison (2017)
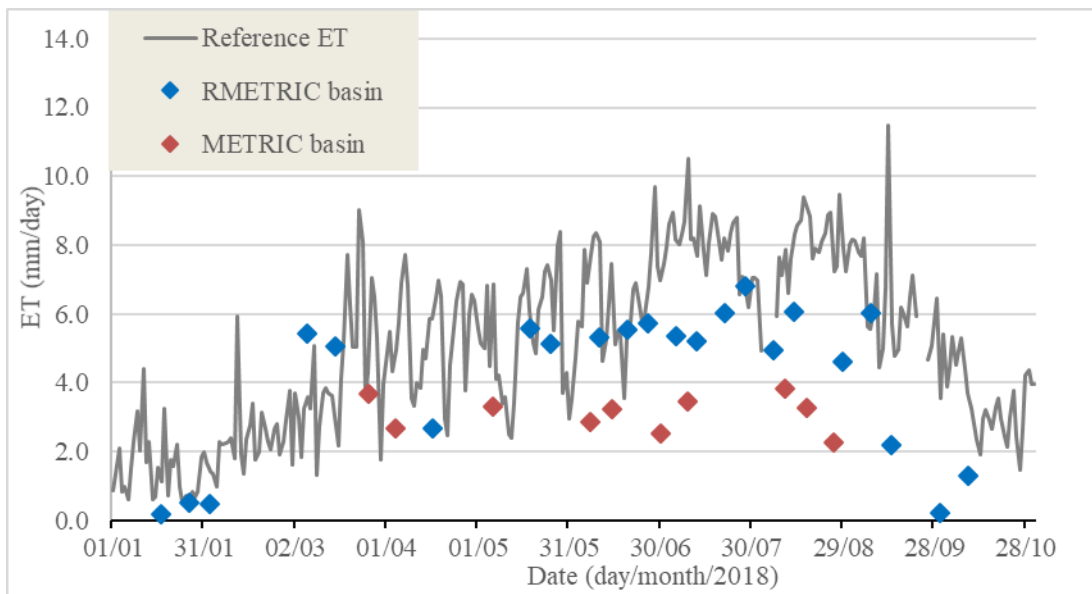
Figure 6.10. The Penman-Monteith reference ET, METRIC and R-METRIC basin averages daily ET comparison (2018)
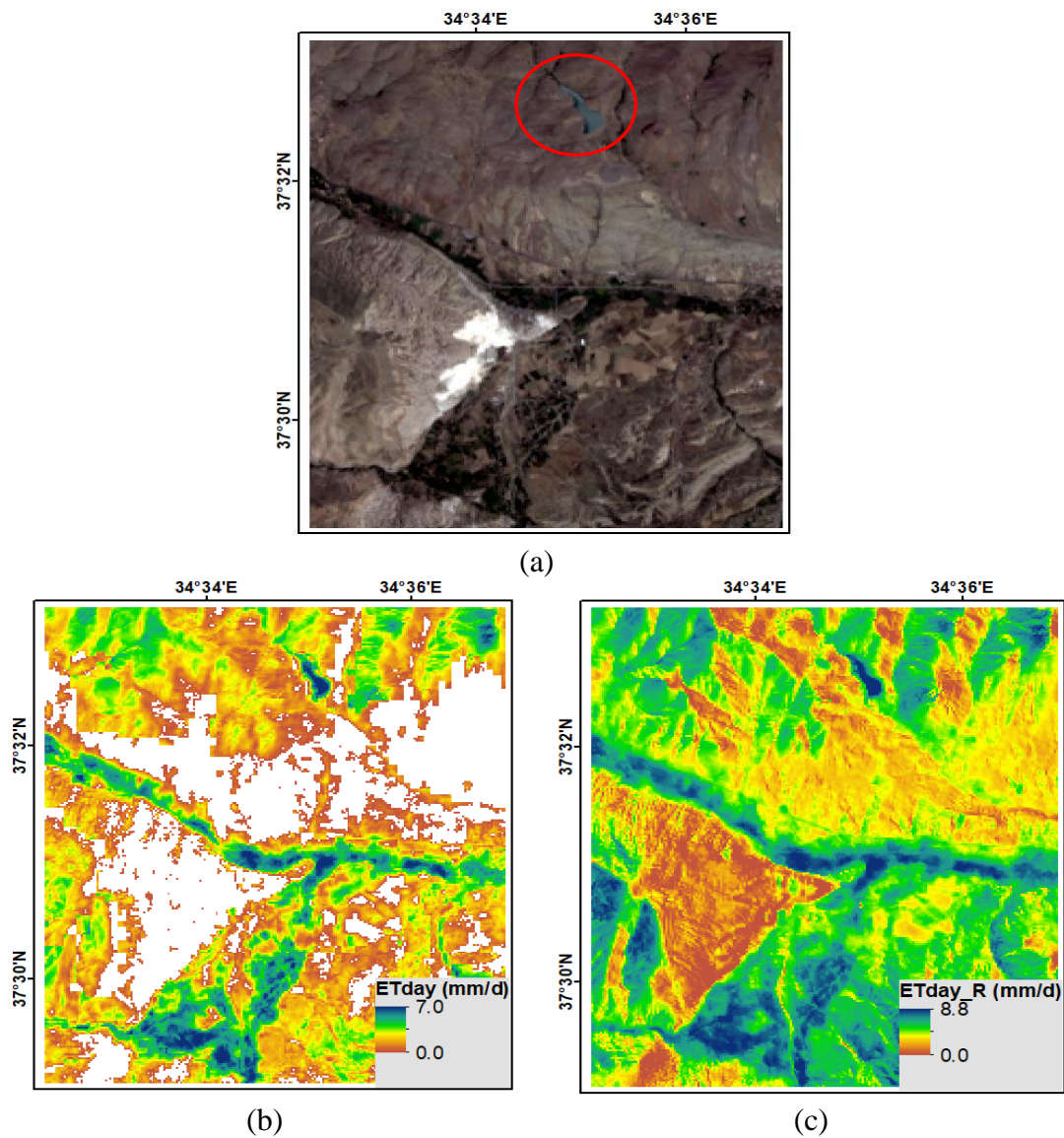
Figure 6.11. Clipped RGB image (a), METRIC daily ET map (b) and R-METRIC
daily ET map (c) (27.06.17)

The reasoning behind the mask in the METRIC model was to get rid of rocky terrain
which we are not interested as a source of ET. Investigating the red part in the middle
of Figure 6.11(c), it is very similar to the masked part in Figure 6.11(b) for the same
region. This shows that the mask utilized in the METRIC model is consistent. Both

models estimate successfully the irrigated cherry tree path along the river channel and the open water surface. However, the R-METRIC model results are generally higher than then METRIC model results.

The Eddy-Covariance tower having 2 sensors for direct latent heat flux measurements was not enough to have a continuous latent heat flux data. According to Wang and Dickinson (2012), 70% of the direct latent heat flux measurements from an Eddy-Covariance system remain after considering bad weather conditions and failures. As a result, residue latent heat flux of the energy balance was the only continuous latent heat flux data measured at the Eddy-Covariance tower.

According to He et al. (2017), for cloudy and rainy weathers the uncertainty coming from the interpolations in calculation enhances. This statement is important due to the usage of 26 cloudy images in the R-METRIC model which can affect the results. However, such images were necessary to increase the temporal resolution of the study results.

According to Oliveira (2018) and Tasumi (2019), for natural vegetation and bare soil the METRIC model overestimates ET more than for agricultural areas. Çakıt basin consisting heavily of natural vegetation and bare soil which is affected from this deduction.

According to Madugundu et al. (2017), the METRIC model estimations are better at full canopy compared to the partial canopy which has a significant impact on a mountainous basin scale such as the Çakıt basin. For the study basin, full canopy is situated along the river channel. However, a large portion of the Çakıt basin consists of natural vegetation and bare soil/rock affecting the METRIC model estimations.

The R-METRIC model is more automated than the METRIC model making the R-METRIC model faster and more reliable considering human error. In addition, the results of the R-METRIC model catch the seasonal trend better than the METRIC model.

CHAPTER 7

CONCLUSIONS AND RECOMMENDATIONS

In this study, remote sensing based models (METRIC and R-METRIC) aiming to estimate spatially distributed evapotranspiration were used in a mountainous area. The results were compared with the Eddy-Covariance flux tower measurements. The following conclusions and recommendations were obtained:

- Knowing that METRIC model estimations are better at full canopy on flat areas compared to partial canopy in mountainous areas, both METRIC and R-METRIC models' results are found satisfactory in the study area, which is located in a mountainous area.

- In order to observe the seasonal trend in ET, the model results are compared to Penman-Monteith Reference ET values. As expected, the Penman-Monteith reference ET is obtained greater than the model based ET values, which are the actual ET values. Both models' results follow the seasonal trend illustrated for years 2017 and 2018.

- R-METRIC model offers a fast and reliable platform for estimating actual ET using the land surface energy balance. Since more satellite images can be used in R-METRIC model, it is possible to get more results to observe the seasonal trend of ET. In this study the R-METRIC model has performed better compared to the Eddy-Covariance flux tower data according to the RMSE and R^2 metrics used in the study.

- The importance of the hot-cold pixel selection in METRIC model is assessed. The lower performance of the METRIC model can be due to the required human expertise at hot-cold pixel selection. The R-METRIC model having automatized hot-cold pixel selection which considers more parameters compared to the METRIC model seems to be more reliable for estimating ET at mountainous regions.

- The fetch approach which considers the average of actual ET estimates around the Eddy-Covariance tower location improved the correlation in the models, taking 100 m fetch distance from the Eddy-Covariance tower helps in smoothing the models' results.

- In the assessment of the modelled ET values, Eddy-Covariance tower flux measurements are found valuable. The lack of energy balance closure observed at the vast majority of eddy covariance flux sites is also observed in the study area. Although the land cover around the eddy covariance flux tower is susceptible to error, the study values remain within the range stated in the literature. It is recommended to have independent measurements of one of the energy balance components that may present a promising approach for complementing ongoing theoretical and experimental efforts aimed at elucidating the causes for the energy imbalance.

- It is recommended to install the Eddy-Covariance tower at full canopy and flat areas and maintain routine calibration of the sensors.

REFERENCES

Aboukhaled, A., Alfaro, A., & Smith, M. (1982). Lysimeters, FAO Irrig. Drain. Pap, 39, 68.

Aksu, H., & Arikan, A. (2017). Satellite-based estimation of actual evapotranspiration in the Buyuk Menderes Basin, Turkey. Hydrology Research, 48(2), 559-570.

Allen, R. G. (1994). An update for the calculation of reference evapotranspiration. ICID Bull., 43(2), 35-92.

Allen, R.G., L.S. Pereira, D. Raes, and M. Smith. 1998. "Crop Evapotranspiration: Guidelines for Computing Crop Water Requirements." United Nations Food and Agriculture Organization, Irrigation and Drainage Paper 56, Rome, Italy, 300.

Allen, R. G., Walter, I. A., Elliott, R., Mecham, B., Jensen, M. E., Itenfisu, D., Howell, T. A., Snyder, R., Brown, P., Echings, S., Hattendorf, M., Cuenca, R. H., Wright, J. L., Martin, D. & Spofford, T. (2000). "Issues, requirements and challenges in selecting and specifying a standardized ET equation." Proc., 4th National Irrig. Symp., ASAE, Phoenix, 201–208.

Allen, R. G., Tasumi, M., Morse, A., & Trezza, R. (2005). Satellite-based evapotranspiration by energy balance for western states water management. In Impacts of Global Climate Change, 1-18.

Allen, R.G., Trezza, R., Tasumi, M., (2006). Analytical integrated functions for daily solar radiation on slopes. Agric. For. Meteorol. 139, 55–73.

Allen, R. G., Tasumi, M., & Trezza, R. (2007). Satellite-based energy balance for mapping evapotranspiration with internalized calibration (METRIC)— Model. Journal of irrigation and drainage engineering, 133(4), 380-394.

Allen, R.G., Pereira, L.S., Howell, T.A., Jensen, M.E., (2011). Evapotranspiration information reporting: I. factors governing measurement accuracy. Agric. Water Manag. 98, 899–920.

ASCE-EWRI (2005). Task Committee on Standardization of Reference Evapotranspiration, Principal; Report by the American Soc. Civil Engineers (ASCE), Report 0-7844-0805-X. In The ASCE Standardized Reference Evapotranspiration Equation. Allen, R.G., Walter, I.A., Elliott, R.L., Howell, T.A., Itenfisu, D., Jensen, M.E., Snyder, R.L. Eds.

Bastiaanssen, W. G. M. (1995). Regionalization of surface flux densities and moisture indicators in composite terrain. A remote sensing approach under clear skies in Mediterranean climates, 271.

Bastiaanssen, W. G., Menenti, M., Feddes, R. A., & Holtslag, A. A. M. (1998). A remote sensing surface energy balance algorithm for land (SEBAL). 1. Formulation. Journal of hydrology, 212, 198-212.

Bisht, G., Venturini, V., Islam, S., & Jiang, L. E. (2005). Estimation of the net radiation using MODIS (Moderate Resolution Imaging Spectroradiometer) data for clear sky days. Remote Sensing of Environment, 97(1), 52-67.

Black, T. A., Tanner, C. B., & Gardner, W. R. (1970). Evapotranspiration from a Snap Bean Crop 1. Agronomy Journal, 62(1), 66-69.

Büyükcangaz, H., Steele, D. D., Tuscherer, S. R., Hopkins, D. G., & Jia, X. (2017). Evapotranspiration mapping with METRIC to evaluate effectiveness of irrigation in flood mitigation for the Devils Lake Basin. Transactions of the ASABE, 60(5), 1575-1591.

Carr, J. E. (1990). National water summary 1987: Hydrologic events and water supply and use (Vol. 2350). US Government Printing Office.

da Silva, B. B., Braga, A. C., Braga, C. C., de Oliveira, L. M. M., Montenegro, S. M. G. L., and Junior, B. B. (2016). "Procedures for calculation of the albedo with OLI-

Landsat 8 images: Application to the Brazilian semi-arid." Revista Brasileira de Engenharia Agrícola e Ambiental, 20(1), 3–8.

Droogers, P., & Allen, R. G. (2002). Estimating reference evapotranspiration under inaccurate data conditions. Irrigation and drainage systems, 16(1), 33-45.

Duffie, J. A., & Beckman, W. A. (1991). Solar engineering of thermal processes. New York: Wiley, 770-772.

Dugas, W. A., Fritschen, L. J., Gay, L. W., Held, A. A., Matthias, A. D., Reicosky, D. C., Steduto, P. & Steiner, J. L. (1991). Bowen ratio, eddy correlation, and portable chamber measurements of sensible and latent heat flux over irrigated spring wheat. Agricultural and forest meteorology, 56(1-2), 1-20.

Frangi, J. P. (1996). Evapotranspiration and stress indicator through Bowen ratio method. In Evapotranspiration and Irrigation Scheduling (Proc. Int. Conf., San Antonio, TX, 3-6 November), St. Joseph, 1996. ASAE.

Fuchs, M., & Tanner, C. B. (1970). Error analysis of Bowen ratios measured by differential psychrometry. Agricultural Meteorology, 7, 329-334.

Guide, P. (2018). Landsat 8 surface reflectance code (LaSRC) product. Availabe online: https://landsat. usgs. gov/sites/default/files/documents/lasrc_product_guide. pdf (accessed on 26 December 2018).

Harlow, R. C., Burke, E. J., Scott, R. L., Shuttleworth, W. J., Brown, C. M., & Petti, J. R. (2004). Research Note: Derivation of temperature lapse rates in semi-arid south-eastern Arizona. Hydrology and Earth System Sciences, 8(6), 1179-1185.

He, R., Jin, Y., Kandelous, M., Zaccaria, D., Sanden, B., Snyder, R., Jiang, J., & Hopmans, J. (2017). Evapotranspiration estimate over an almond orchard using landsat satellite observations. Remote Sensing, 9(5), 436.

Jensen, M. E., Burman, R. D., and Allen, R. G., eds. (1990). "Evapotranspiration and irrigation water requirements." ASCE Manuals and Reports on Engineering Practice No. 70, ASCE, Reston, Va

Jiménez-Muñoz, J. C., Sobrino, J. A., Skoković, D., Mattar, C., & Cristóbal, J. (2014). Land surface temperature retrieval methods from Landsat-8 thermal infrared sensor data. IEEE Geoscience and remote sensing letters, 11(10), 1840-1843.

Khadr, M. (2016). Forecasting of meteorological drought using Hidden Markov Model (case study: The upper Blue Nile river basin, Ethiopia). Ain Shams Engineering Journal, 7(1), 47-56.

Köksal, E. S. (2008). Evaluation of spectral vegetation indices as an indicator of crop coefficient and evapotranspiration under full and deficit irrigation conditions. International Journal of Remote Sensing, 29(23), 7029-7043.

Lian, J., & Huang, M. (2015). Evapotranspiration estimation for an oasis area in the Heihe River Basin using Landsat-8 images and the METRIC model. Water resources management, 29(14), 5157-5170.

Madugundu, R., Al-Gaadi, K. A., Tola, E., Hassaballa, A. A., & Patil, V. C. (2017). Performance of the METRIC model in estimating evapotranspiration fluxes over an irrigated field in Saudi Arabia using Landsat-8 images. Hydrology and Earth System Sciences, 21(12), 6135-6151.

Mastrorilli, M., Katerji, N., Rana, G., & Nouna, B. B. (1998). Daily actual evapotranspiration measured with TDR technique in Mediterranean conditions. Agricultural and Forest Meteorology, 90(1-2), 81-89.

NOAA (1976). Atmosphere, U. S. Standard. Washington DC: US Government Printing Office.

Oliveira, B., Caria Moraes, E., Carrasco-Benavides, M., Bertani, G., & Augusto Verola Mataveli, G. (2018). Improved Albedo Estimates Implemented in the METRIC

Model for Modeling Energy Balance Fluxes and Evapotranspiration over Agricultural and Natural Areas in the Brazilian Cerrado. Remote Sensing, 10(8), 1181.

Olmedo, G. F., Ortega Farias, S., Fonseca Luengo, D., and Fuentes Peñailillo, F. (2016). water: Tools and functions to estimate actual evapotranspiration using land surface energy balance models in R. R J. 8:352–369.

Rana, G., & Katerji, N. (2000). Measurement and estimation of actual evapotranspiration in the field under Mediterranean climate: a review. European Journal of agronomy, 13(2-3), 125-153.

Revfeim, K. J. A., & Jordan, R. B. (1976). Precision of evaporation measurements using the Bowen ratio. Boundary-Layer Meteorology, 10(2), 97-111.

Rolland, C. (2003). Spatial and seasonal variations of air temperature lapse rates in Alpine regions. Journal of climate, 16(7), 1032-1046.

Shuttleworth, W. J. (2008). Evapotranspiration measurement methods. Southwest Hydrology, 7(1), 22-23.

Silva, J., Ribeiro, C., & Guedes, R. (2007). Roughness length classification of Corine Land Cover classes. In Proceedings of the European Wind Energy Conference, Milan, Italy, Volume 710, 110.

Sinclair, T. R., Allen, L. H., & Lemon, E. R. (1975). An analysis of errors in the calculation of energy flux densities above vegetation by a Bowen-ratio profile method. Boundary-Layer Meteorology, 8(2), 129-139.

Szeicz, G., & Long, I. F. (1969). Surface resistance of crop canopies. Water Resources Research, 5(3), 622-633.

Szeicz, G., Van Bavel, C. H. M., & Takami, S. (1973). Stomatal factor in the water use and dry matter production by sorghum. Agricultural Meteorology, 12, 361-389.

Tanner, C. B. (1967). Measurement of evapotranspiration. Irrigation of agricultural lands, (irrigationofagr), 534-574.

Tasumi, M. (2003). Progress in Operational Estimation of Regional Evapotranspiration Using Satellite Imagery. University of Idaho, Moscow, ID.

Tasumi, M. (2019). Estimating evapotranspiration using METRIC model and Landsat data for better understandings of regional hydrology in the western Urmia Lake Basin. Agricultural Water Management, 226.

Thyer, N. (1985). Looking at western Nepal's climate. Bulletin of the American Meteorological Society, 66(6), 645-650.

Trezza, R., Allen, R., & Tasumi, M. (2013). Estimation of actual evapotranspiration along the Middle Rio Grande of New Mexico using MODIS and landsat imagery with the METRIC model. Remote Sensing, 5(10), 5397-5423.

Twine, T. E., Kustas, W. P., Norman, J. M., Cook, D. R., Houser, P., Meyers, T. P., Prueger, J. H., Starks, P. J. & Wesely, M. L. (2000). Correcting eddy-Covariance flux underestimates over a grassland. Agricultural and Forest Meteorology, 103(3), 279-300.

url1: https://earthexplorer.usgs.gov (3 December 2019).

url2: http://usgs.gov/land-resources/nli/landsat/using-usgs-landsat-level-1-data-product (3 December 2019).

Wang, K., & Dickinson, R. E. (2012). A review of global terrestrial evapotranspiration: Observation, modeling, climatology, and climatic variability. Reviews of Geophysics, 50(2).

Widmoser, P., & Wohlfahrt, G. (2018). Attributing the energy imbalance by concurrent lysimeter and eddy covariance evapotranspiration measurements. Agricultural and forest meteorology, 263, 287-291.

Wilson, K. B., Hanson, P. J., Mulholland, P. J., Baldocchi, D. D., & Wullschleger, S. D. (2001). A comparison of methods for determining forest evapotranspiration and its

components: sap-flow, soil water budget, eddy Covariance and catchment water balance. Agricultural and forest Meteorology, 106(2), 153-168.

Wilson, K., Goldstein, A., Falge, E., Aubinet, M., Baldocchi, D., Berbigier, P., Bernhofer, C., Ceulemans, R., Dolman, H., Field, C. & Grelle, A. (2002). Energy balance closure at FLUXNET sites. Agricultural and Forest Meteorology, 113(1-4), 223-243.

Zhao, W. G., Berliner, P. R., Zangvil, A., Camp, C. R., Sadler, E. J., & Yoder, R. E. (1996). Heat storage terms in evapotranspiration estimation. In Evapotranspiration and Irrigation Scheduling. Proceedings of the International Conference, November, 3-6.